SOLVING THE PROBLEM OF WATER IMPACT IN WAVES BY IMPROVING A CONSTRAINED INTERPOLATION PROFILE BASED METHOD

by

© Peng Wen, B.Eng, M.Eng.

A thesis submitted to the

School of Graduate Studies

in partial fulfilment of the

requirements for the degree of

Doctor of Philosophy

Department of Ocean and Naval Architectural Engineering

Memorial University of Newfoundland

October 2018

St. John's Newfoundland

Abstract

This thesis presents numerical solutions to water impacts on two-dimensional and three-dimensional objects entering calm water as well as regular waves. The highly nonlinear water entry problems which are governed by the Navier-Stokes equations were solved by a Constrained Interpolation Profile (CIP)-based finite difference method on fixed Cartesian grids. The advection calculations were solved by the CIP method. A pressure-based algorithm was applied for the non-advection calculations. The highly violent water surface was determined by using color functions and the tangent of hyperbola for interface capturing scheme with weighed line interface calculation method (THINC/WLIC). A three-dimensional numerical wave tank (NWT) with a damping zone was developed. A parallel computing algorithm based on the message passing interface (MPI) was implemented to speed up the computations.

Validation studies of the present method were carried out for several two-dimensional and three-dimensional bodies entering calm water symmetrically and asymmetrically with prescribed velocities and free-fall motions. The predicted impulsive impact, motions and free surface were compared with the experimental results. Satisfactory agreement was demonstrated.

Furthermore, this work systematically studied the influence of regular waves on the slamming impacts. Prior to it, a NWT was formed and validated by generating regular waves and by solving the impact underneath a fixed deck. The predicted impact force was in good agreement with the experimental data. The water entry of a wedge in regular waves was then investigated. The slamming forces and the pressure distributions were predicted and compared with calm water solutions. A thorough

study was also conducted to examine how the slamming impact can be affected by various factors, such as wave properties (the wave length and the wave height), the wave heading, the entry velocity and the location of entry. It was found that waves resulted in obvious horizontal slamming force and asymmetrical pressure distribution on the wedge bottom. The entry location and the entry velocity had a significant effect on the slamming forces. Increased local pressure on the wedge bottom may occur due to the presence of waves.

Acknowledgements

Firstly, I would like to express my sincere gratitude to my supervisor, Dr. Wei Qiu, for his continuous support throughout my PhD studies and research. I am very grateful for his patience and kindness. Not only has his guidance consistently helped me throughout conducting my research, but also his encouragement has helped me through the difficult times I have encountered.

Besides my supervisor, I would like to thank the rest of my thesis committee, Dr. Heather Peng and Dr. David Molyneux, for their insightful comments. They have helped me to better understand the field of marine hydrodynamics. Without their precious support, it would not have been possible to conduct this research. I would also like to show my gratitude to my colleagues and friends at Memorial University, for the helpful discussions and suggestions in all the stages of my research.

I am very grateful to the support by NSERC through its CREATE program. Without this support, I would have not been able to complete this research.

Last but not the least, I would like to thank my family. I would like to thank my wife, Yi Zhang, for her love, patience and support throughout my PhD studies. I also owe my deepest gratitude to my parents, B.S. Wen and X.R. Dong, for their support and understanding all the time. Thanks for the birth of my son, Lucas. You let me understand more deeply the meaning of life. I would also like to express my gratitude to my parents-in-law, C.X. Mu and L.L. Zhang, for their great efforts in taking care of Lucas.

Contents

List of Tables

List of Figures

Chapter 1

Introduction

1.1 Background

Marine vessels and offshore structures operating in harsh environments are subjected to water impacts which are commonly called slamming. Large-amplitude ship motions can result in impulsive water impact and green water on deck, which will subsequently cause severe damage to ship structures. Launching life boats into water is another example of the water entry problem. The horizontal members on the offshore structures in the splash zone may encounter engulfing by large and possibly breaking waves. The deck joining two hulls of a multi-hull vessel can encounter wet-deck slamming when a wave hits the underside of it. For these structures, the wave impacts may be a serious source of fatigue. To improve the safety and operation of ships and offshore structures, it is necessary to gain knowledge of flow behaviour and the induced motion of ships during the water entry process. The prediction of both local and global forces and pressures, exerted by the impact on the structures, is especially important. An

in-depth review of the current state of knowledge on slamming can be found in [1].

The slamming problem is highly nonlinear since it involves breaking water surfaces and air bubbles. The majority of the investigation into slamming problems were simplified by considering simple shapes, such as a wedge with large deadrise angles, entering into calm water. A large number of experimental studies have been conducted by various researchers. For example, Zhao et al. [111] conducted vertical drop tests for a wedge section and a ship bow flare section. Kim et al. [38] conducted similar drop tests for symmetric and asymmetric wedges. Wei and Hu [86] studied the complex hydrodynamics of a horizontal cylinder entering water. Except for water entry in calm water, model tests were conducted in wave tanks. For example, Ochi [50] carried out a series of self-propelled tests on two model ships in various wave lengths, wave heights and at various ship drafts in regular waves. Hermundstad and Moan [24] conducted model tests of a car carrier in regular waves of various heights. They studied slamming on two panels in the upper part of the bow flare. Kim et al. [37] measured the stern slamming impact by towing a containership model in regular and irregular waves. Head and following sea conditions of different ship speeds were considered. These experiments not only revealed some characteristics of the slamming process, but also provided benchmark data for the validation of numerical models. However, they are usually expensive to conduct.

With the increasing power of computers, numerical simulations have also been conducted to study the water entry problems. Korobkin and Pukhnachov [42] gave a review of earlier numerical research on water entry problems. Examples of the recent numerical studies of water entry problems include the work based on the boundary element method (BEM) by Zhao and Faltinsen [110], the predictions of 2-D slamming

problems of symmetric bodies based on the VOF method by Kleefsman et al. [41] and the 2-D simulation of water entry for various bodies based on the Constrained Interpolation Profile (CIP) method by Wen and Qiu [92].

It was not until recently that the effects of water waves on slamming impact was investigated numerically. Hu and Liu [32] presented the pressure distribution on a 2-D flat-bottom body impacting with waves based on the finite volume method (FVM). Sun et al. [67] analysed the hydrodynamic problem of a two dimensional wedge entering waves based on the incompressible velocity potential theory. The gravity effect, the wave height, the wave length, the location of entry and the entry angle were studied.

In this thesis, the water entry problems for 2-D and 3-D objects entering both calm water and regular waves are investigated numerically with a CIP-based method. Emphasis is put on accurate prediction of the slamming impact force/pressure and the disturbed water surface. Another significance of this work is to examine how water waves affect them. A review of analytical, experimental and numerical studies on slamming problems is given in the next section.

1.2 Literature Review

1.2.1 Analytical-oriented Studies

Owing to the practical importance in ocean engineering, the water-entry problem has been extensively studied by many researchers. The theoretical analysis of the similarity flow induced by the wedge entry was pioneered by von Karman [78], who

developed an asymptotic theory for flat impact problems. Later, Wagner [79] modified von Karman's solution by considering the effect of water splash on the body. Shiffman and Spencer [63] developed general solutions for the vertical impact of a cone on a water surface. Verhagen [76] investigated the impact of a flat plate on a water surface both theoretically and experimentally. Cointe and Armand [12] extended Wagner's theory and addressed the problem of the vertical water entry of a rigid horizontal cylinder. Korobkin and Pukhnachov [42] reviewed early numerical research on water entry problems. Howison et al. [29] reviewed and extended Wagner's solution to include 3-D impact and air-cushion effects. Mei et al. [48] applied Wagner's theory and derived the analytic solution of the water impact problem for a general 2-D body. Oliver [52] extended Wagner's solution to derive the second-order corrections using a systematic matched-asymptotic analysis. Most of these methods were limited to simple 2-D geometries and shallow body submergence.

1.2.2 Experimental Studies

Experimental methods have been used to study the water entry problems. Chuang [10] carried out several early water entry tests on a flat-bottom model and wedges with various small deadrise angles (from 1° to 15°) from various drop heights. Chuang and Milne [11] later conducted similar tests on cone-shaped models with various deadrise angles and compared the test results with theory and those for two-dimensional wedge models. Greenhow and Lin [22] conducted water entry tests of wedges with large deadrise angles (over 30°) and cylinders into calm water. Troesch and Kang [71] studied experimentally the water entry of a sphere and a cusped body. They used

the test results to validate numerical predictions. Lin and Shieh [44] utilized a high-speed charge coupled device (CCD) camera and a digital particle tracking velocimeter (DPTV) to study the pressure and flow field during the water entry of a flat-bottom body and a cylinder. Zhao et al. [111] carried out drop tests of a wedge section with 30° deadrise angle and a ship bow section. Engle and Lewis [15] conducted drop tests on wedges with two deadrise angles (10° and 20°). Hermundstad and Moan [24] conducted model tests on a Ro-Ro vessel to study the bow flare slamming in regular oblique waves. They used the test results to validate numerical predictions. Yettou et al. [106] investigated the pressure distribution on a free-falling wedge upon entering calm water. Parameters such as the drop height, the deadrise angle and the mass of the wedge were studied. Davis and Whelan [13] carried out a series of drop tests with a two-dimensional catamaran bow cross section to evaluate a computational model for catamaran wet deck slamming. Zhu et al. [112] examined the water entry and exit of a horizontal circular cylinder and validated their numerical solutions. Tveitnes et al. [72] investigated the constant velocity water entry and exit of wedge sections. Huera-Huarte et al. [34] conducted drop tests on flat panels at different entry velocities and for angles in the range from 0.3° to 25°. Peng et al. [58] investigated the slamming load on a small scale trimaran model in the drop tests with various drop heights. Alaoui and Nême [2] presented experimental results for slamming impacts on cones, square pyramids and wedge-cones entering calm water at constant velocities. Hong et al. [28] conducted drop tests on a modified Wigley hull model with various drop heights.

Van Nuffel et al. [75] studied the local and global loads acting on a rigid cylinder subjected to water wave slamming. Panciroli et al. [54] investigated the water impact

of deformable wedges using numerical and experimental methods. Hong et al. [27] measured the temporal and spatial distribution of bow flare slamming load on a 10000 TEU containership model in various wave conditions. Kim et al. [38] experimentally studied the local water impact loads on two-dimensional symmetric and asymmetric wedges. Tian et al. [70] carried out experiments to study the water impacts on a bow flare section. Van Nuffel et al. [74] presented a detailed study on the local pressures acting on the surface of a cylinder during vertical water entry into calm water. Wei and Hu [86] investigated the water entry of a horizontal cylinder into calm water with various length to diameter ratios, cylinder water density ratios and drop heights. Kim et al. [37] studied the characteristics of stern slamming loads on a 10000 TEU containership model in regular and irregular waves. Panciroli et al. [57] experimentally studied the water entry of curved rigid wedges with varied radius of curvature and drop heights. Shams et al. [61] experimentally characterized the water entry of an asymmetric wedge with varied heel angles into calm water using particle image velocimetry (PIV). Wang et al. [81] investigated the water entry of a free-falling wedge. They focused on the evolution of the pressure on the impact sides and the top side, the global hydrodynamic loads, the air-water interface and the wedge motion. Wei and Hu [87] presented experimental results of the water entry of inclined cylinders with various inclined angles, density ratios and length to diameter ratios. Barjasteh et al. [5] investigated the asymmetric water entry of wedges with various deadrise angles, inclination angles and impact speeds. Wang and Guedes Soares [84, 83] studied the bow and stern slamming of a chemical tanker in irregular head waves.

Hydroelasticity is important in slamming [16]. There have been a few experi-

mental works on slamming of elastic structures. Carcaterra and Ciappi [6] reported theoretical and experimental analysis of the response of an elastic wedge-shaped body impacting the water surface. Faltinsen and Chezhian [17] presented numerical and experimental studies on slamming of a three-dimensional body with idealized shape. Peseux et al. [59] studied the slamming of rigid and deformable cones with different deadrise angles and thickness. Panciroli et al. [55] presented numerical and experimental studies on the hydroelastic phenomena during the water entry of elastic wedges. The tests varied the wedge thickness, the deadrise angle and the impact velocity. Stenius et al. [64] presented a method to experimentally characterize the significance of hydroelasticity for slamming loaded marine panels. Panciroli and Porfiri [56] studied hydroelastic effects of flexible panels during water entry through PIV measurements. Shams et al. [62] investigated the entire hydroelastic slamming of a wedge, from the entry to the exit phase.

1.2.3 Numerical Studies

Various numerical methods have also been developed to address water entry problems. The potential flow theory has been applied to solve the water entry problem of a wedge, for example, by Vinje and Brevig [77], Greenhow [20], Zhao and Faltinsen [110] and Zhao et al. [111]. Greenhow [21] further calculated the water entry and exit of a horizontal cylinder. Wu et al. [94] analysed the water entry problem of a wedge through free fall motion. Hermundstad and Moan [24] used a nonlinear strip theory method with a generalized 2-D Wagner formulation solved by the boundary element method to predict the slamming loads on a car carrier. The results were validated by

experimental results. Chuang et al. [9] developed a boundary element method based on the desingularized Cauchy's formula and removed the corner singularity at the intersection point of the body and the water surface. Sun and Faltinsen [65] developed a 2-D BEM method to simulate the water impact of horizontal circular cylinders and cylindrical shells. Wu [93] investigated the water entry of twin wedges based on the potential flow theory and studied the interaction effect. Xu et al. [97] simulated the oblique water entry of an asymmetrical wedge based on a BEM method with an analytical solution for the jet. Sun and Wu [66] analysed the 3-D oblique entry of a cone into water based on the BEM method using fully nonlinear boundary conditions on the moving free surface and the body surface. Xu and Wu [96] used BEM with vortex shedding to simulate the oblique water entry of a wedge. The pressure jump was addressed by imposing the Kutta condition at the wedge apex. Bao et al. [4] studied the 2-D oblique entry of a wedge with three degrees of freedom. Wang and Faltinsen [80] improved the results of Zhao and Faltinsen [110] and presented reliable results for deadrise angles down to 1°.

Although great efforts have been made to solve water entry problems based on the potential flow theory, it is still difficult for these methods to treat the highly distorted or breaking free surface. The gravity term is usually ignored in these methods and thus the study is limited to short-term simulation. These difficulties can be overcome by solving the the Navier-Stokes equations using a computational fluid dynamics (CFD) technique coupled with an interface capturing scheme. They have been increasingly employed to overcome the difficulties in treating the highly nonlinear free surface. CFD methods can generally fall in two broad categories: Lagrangian methods and Eulerian methods.

The smoothed particle hydrodynamics (SPH) method, a Lagrangian method originally developed by Gingold and Monaghan [18], has been applied to water entry problems. Oger et al. [51] studied the water entry of a wedge using the SPH method. Kim et al. [39] applied the SPH method to simulate the 2-D water entry of asymmetric bodies. Gong et al. [19] studied the hydrodynamic problem of a 2-D wedge entering water based on the SPH method with a non-reflection boundary treatment. Panciroli et al. [55] presented numerical and experimental studies on the water entry of elastic wedges. The numerical model was based on a coupled finite element method (FEM) and SPH formulation, with the commercial code LS-DYNA. Ren et al. [60] used a modified moving particle semi-implicit (MPS) method to simulate the water entry of a 2-D wedge and a 2-D ship section. Chae and Yoon [8] estimated the water splash and slamming pressures caused by water entry based on an SPH method. Ma and Liu [45, 46] conducted a comparative study on the wedge water entry with a 2-D two-phase SPH method. Zha et al. [108] used an improved MPS method to simulate the hydroelastic water entry of a 2-D wedge.

The level set (LS) method, originally developed by Osher and Sethian [53], is a free surface capturing method. The deformation and movement of the free surface is captured by a continuous smooth function. The LS method has been used to simulate the water entry of solid bodies by Gu et al. [23]. Yang et al. [103, 102] studied the water entry problems of 2-D triangular wedges and ship sections using a LS method and an immersed boundary method (IBM).

The finite volume method (FVM) was also employed. The FVM is based on the integral of the governing Navier-Stokes equations. The integrated equations are discretized over control volumes. An interface capturing scheme is usually coupled

to track the free surface. For example, Kleefsman et al. [41] applied the volume-of-fluid (VOF) method to simulate 2-D symmetric slamming problems of a wedge, a cone and a circular cylinder. Wang and Wang [85] solved the water entry problem of 2-D twin cylinders using a free surface capturing method and Cartesian cut cell mesh based on FVM. Swidan et al. [68] computed the local slamming loads of a 2-D wedge shaped hull using the FVM method. Wang and Guedes Soares [82] investigated the water impact of 3-D buoys by using an explicit finite element method with an Arbitrary-Lagrangian Eulerian (ALE) solver. Zhang et al. [109] studied the effect of compressibility on pressure distribution based on a finite element method solver. Ma et al. [47] used the open source FVM code, OpenFOAM, to simulate the water entry of 2-D wedges. Iranmanesh and Passandideh-Fard [35] investigated the slamming of a 3-D horizontal circular cylinder using the VOF method. Kamath et al. [36] studied the water entry of a 2-D free falling wedge using a CFD method. Monroy et al. [49] compared the merits of the potential theory based method and the CFD method based on a VOF interface.

Some unconventional CFD approaches have been used to solve the water entry problems. Li te al. [43] applied the lattice Boltzmann method (LBM) to simulate the water entry problem. Studies on the water entry of a wedge and a ship section were carried out by Hong et al. [26]. In their work, results from a number of participants based on various numerical methods were compared. It was found that CFD methods are promising for cases where the wedge has a tilted angle of zero and for ship sections with smaller drop heights. There is a need to investigate further the asymmetric water entry of the wedge and the symmetric water entry of the ship section with larger drop heights.

The constrained interpolation profile (CIP) method, originally developed by Takewaki et al. [69], Yabe [100] and Yabe et al. [99], has also been used in water entry studies. The CIP method solves the advection of a function based on a high-order upwind scheme. It can achieve sub-cell resolution while retaining the sharpness of the profile. Hu and Kashiwagi [30] further developed the CIP combined and unified procedure (CCUP) to simulate violent free surface flows. The robustness and the stability of the CCUP method has been demonstrated in treating multi-phase flows. Zhu et al. [112] applied the CCUP method to simulate the water entry and the exit of a 2-D circular cylinder. The results were compared with experimental data. In the work of Yang and Qiu [105], the CIP method was extended to solve the water entry problems of 3-D bodies based on their studies of 2-D problems (Yang and Qiu, [104]). Wen and Qiu [89, 90, 91, 92] further developed the CIP method by implementing the parallel computation algorithm and applied it to 2-D and 3-D slamming problems. Wei et al. [88] studied the hydrodynamic problem for water entry of 2-D wedges with a CIP-based method. The Tangent of Hyperbola for Interface Capturing (THINC) method was used for interface capturing. Hu et al. [33] applied the CIP method and the THINC/slope weighting (SW) scheme to simulate the water entry of twin wedges. Kim et al. [40] studied the 2-D water entry of a symmetric wedge and a ship section with low drop height using two potential flow based methods, a CIP-based method and an over-set method. The numerical results were compared with each other and with model test data. It was found that the CFD methods can be applied to solve the water entry of ship-like sections which is difficult to solve with a potential flow based method. The CIP method has proven to be robust in solving 2-D and 3-D slamming problems.

It is clear from this literature review that a large amount of experimental, analytical and numerical work has been conducted in tackling water entry problems. Most of the work, however, has been limited to 2-D and simplified geometries. Another restriction in some of the previous numerical studies was that the simulation was only for the initial entry stage. Moreover, nearly all the work focused on water entry into calm water. Thus, there is a need to develop an accurate and effective tool which solves the 3-D water entry problem given any arbitrary geometrical shape in a long-term simulation. It is also necessary to examine the effects of propagating waves on the water entry process. The main focuses of the present work are summarized in the next section.

1.3 Present Work

The present research focused on the numerical simulation of highly nonlinear water entry problems in waves based on a CIP-based FDM method. The main objectives of this thesis are summarized as follows:

- Water impact in waves. The majority of the previous studies on the water entry problems was focused on the entry into calm water. Relatively few attempts were made to analyse the water entry of an solid object into waves. The effects of the relative velocity between the object and the waves have not been thoroughly examined. In this work, a 3-D numerical wave tank is generated based on the CIP-based method. The water entry of a wedge into regular waves is studied. The effects of several wave properties, such as wave length, wave height and location of entry on the water impact are investigated.

- Improved prediction of slamming impact on arbitrary geometry. Due to the complex physical phenomena and the challenges to the numerical techniques, most studies of water entry problems have focused on 2-D simulations with simplified geometries, such as wedges. Further, the highly violent free surface has not been well modelled. This work aims at developing a numerical simulation program for solving the water entry of a 3-D body with arbitrary geometry. More importantly, the accurate prediction of the pressure distribution on the body, the impact force and the shape of the free surface (the jets, air bubbles, etc.) is the primary goal in this thesis.

- Free fall mode simulation. Realistically, when it comes to water entry problems, the trajectory of a solid body is not always known. It is necessary for a simulation code to be able to determine the motion of the body as well. This is challenging because the prediction of the body's motion affects the solution of the flow field surrounding the body and thus the slamming force acting on it. Inaccurate impact force in turn affects the motion of the body as the coupled motion has to be solved by considering the impact forces as external forces acting on the body.

- Parallel computation. In comparison with simulations based on the potential flow theory, the present method is more time consuming. To address this issue, the modern high performance computers with multiple processors and more powerful computing clusters are utilized. The simulation program developed in this work is based on a parallel computation technique, MPI. The parallel computing program speeds up the simulations and enables finer grids.

1.4 Description of Software Development

A computer program based on the improved CIP-based method and MPI was developed to simulate the water entry of a 2-D or 3-D solid body with arbitrary geometry into calm water or waves. The program predicts slamming forces, pressure distributions on a rigid body and free surface by solving 6-DOF of motions.

The program was written in FORTRAN 90 with the MPI library, MPICH (version 3.0.4). Several MacPro workstations with Linux system and a computing cluster at Memorial University have been used for the simulation cases as discussed in this thesis. The typical computing time for a 2-D simulation of entry into calm water is about one hour and twenty four hours for a 3-D one using 12 processors. It takes much longer time for a simulation of slamming in waves.

1.5 Outline of the Thesis

Chapter 1 introduces the water entry problem and presents a review of previous studies on this subject. The objectives and the outline of this thesis are also presented.

Chapter 2 gives details on the mathematical formulations of the CIP-based method. The CIP method is introduced and the interface capturing scheme, the THINC/WLIC scheme, is formulated. A parallel computing algorithm is presented. The computational methods for predicting hydrodynamic forces and moments and the body motions are provided. The development of a numerical wave tank is then presented.

In Chapter 3, the numerical methods are validated by simulating several 2-D water entry problems including wedges with/without tilted angles and ship sections with

different drop heights. Convergence studies on domain sizes, grid sizes and time steps are presented. Three interface capturing schemes are compared. Both compressible and incompressible solvers are studied. The numerical solutions are compared with published experimental results. The free fall mode simulation is also presented.

In Chapter 4, the present method is extended to 3-D water entry problems. Several 3-D water entry problems are simulated and the numerical solutions are compared with experimental data. The 3-D computations include the water entry of a wedge section with prescribed velocities, the free fall of a Wigley hull and the free fall of an inclined circular cylinder. The predicted impact forces and motions are compared with experimental results.

Chapter 5 focuses on analysing the water entry of a wedge into regular waves. Convergence studies are carried out on grid size and time step. The numerical wave tank is validated by simulating the wave impact on deck. The water entry into waves is then studied. The effects of wave lengths, wave heights, encounter angles, entry velocities and entry locations on the water entry impact are examined. The pressure distribution on the wedge bottom and the slamming forces are predicted and analysed. Discussions on the solutions are presented.

In Chapter 6, this thesis ends with conclusions. Some future perspectives are presented.

Chapter 2

Numerical Formulations

2.1 Coordinate System

The Earth-fixed Cartesian coordinate system is adopted. As demonstrated in Fig. 2.1, the z-axis is pointing upward and the water surface is located at $z = 0$. In this chapter, only three-dimensional formulations are presented. When it comes to 2-D computations, the x-z coordinate system is used.

2.2 Governing Equations

Due to the short duration, turbulence is usually not fully generated in slamming problems. As a result, the laminar flow is assumed in the slamming problems. The differential equations governing the compressible and viscous flow can be written as:

$$\frac{\partial \rho}{\partial t} + u_i \frac{\partial \rho}{\partial x_i} = -\rho \frac{\partial u_i}{\partial x_i} \tag{2.1}$$

$$\frac{\partial u_i}{\partial t} + u_j \frac{\partial u_i}{\partial x_j} = -\frac{1}{\rho} \frac{\partial \sigma_{ij}}{\partial x_j} + f_i \tag{2.2}$$

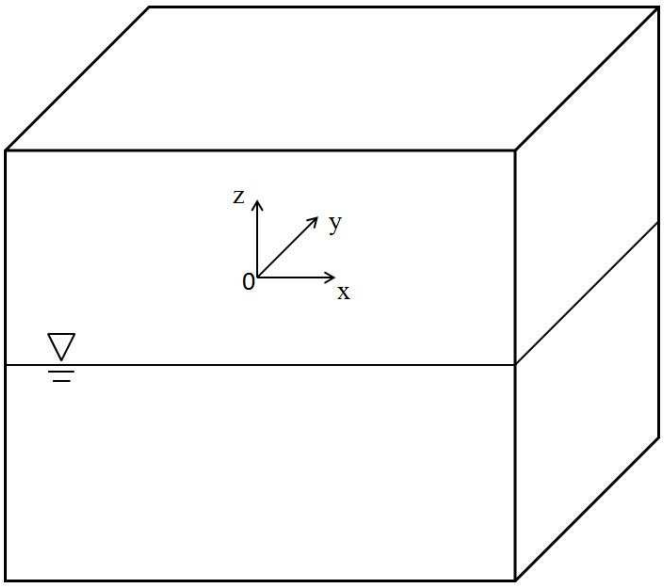

Figure 2.1: Earth-fixed coordinate system

where t is time, x_i $(i = 1, 2, 3)$ are the spacial coordinates in the Cartesian coordinate system, ρ is the density of the fluid, u_i are the velocity components, σ_{ij} is the stress tensor, and f_i are the body forces.

The Newtonian fluid is assumed. The total stress, σ_{ij}, can be written as:

$$\sigma_{ij} = -p\delta_{ij} + 2\mu S_{ij} - 2\mu\delta_{ij}S_{kk}/3$$
$$S_{ij} = \frac{1}{2}(\frac{\partial u_i}{\partial x_j} + \frac{\partial u_j}{\partial x_i})$$

where μ is the dynamic viscosity and δ_{ij} is the Kronecker delta function.

Since the temperature variation is not considered in this study, the equation of state can be written as $p = f(\rho)$. Applying it to Eq. (2.1), the pressure equation can be obtained:

$$\frac{\partial p}{\partial t} + u_i\frac{\partial p}{\partial x_i} = -\rho C_s^2\frac{\partial u_i}{\partial x_i} \tag{2.3}$$

where $C_s = \sqrt{\partial p/\partial\rho}$ is the sound speed and p is the pressure.

2.3 CIP-based Flow Solver

A domain embedding staggered Cartesian grid system with variable cell sizes is used. The water phase and the air phase are described by the same governing equations which are described in the previous section. The fractional step approach is applied to the governing equations, Eqs. (2.1) and (2.2), so that they are split and solved stepwise in three phases:

1. Advection phase:

$$\frac{\partial \rho}{\partial t} + u_i \frac{\partial \rho}{\partial x_i} = 0 \tag{2.4}$$

$$\frac{\partial u_i}{\partial t} + u_j \frac{\partial u_i}{\partial x_j} = 0 \tag{2.5}$$

$$\frac{\partial p}{\partial t} + u_i \frac{\partial p}{\partial x_i} = 0 \tag{2.6}$$

2. Non-advection phase I

$$\frac{\partial u_i}{\partial t} = \frac{2\mu}{\rho} \frac{\partial}{\partial x_j} (S_{ij} - \frac{1}{3} \delta_{ij} S_{kk}) + f_i \tag{2.7}$$

3. Non-advection phase II

$$\frac{\partial \rho}{\partial t} = -\rho \frac{\partial u_i}{\partial x_i} \tag{2.8}$$

$$\frac{\partial u_i}{\partial t} = -\frac{1}{\rho} \frac{\partial p}{\partial x_i} \tag{2.9}$$

$$\frac{\partial p}{\partial t} = -\rho C_s^2 \frac{\partial u_i}{\partial x_i} \tag{2.10}$$

The advection phase solves the linear advection of various variables including the density, ρ, the velocity components, u_i and the pressure, p. The CIP method is employed to compute the advection phase. The principle and formulation of the CIP

method are described in Appendix A.1. The CIP method is a high order upwind scheme which can achieve sub-cell resolution. The numerical stability and accuracy of the CIP method were examined by Utsumi et al. [73], in which it was shown that the numerical stability is dependent on both the grid size and the time step. Sufficiently small grid size and Courant-Friedrichs-Lewy number, $c = u\Delta t/\Delta x$, are typically required. In the work of Utsumi et al. [73], it was also shown that the CIP method has less numerical dissipation and dispersion than other numerical schemes. In this thesis, grid sizes and time steps were carefully chosen to meet the requirements of numerical stability as for the CIP method.

The non-advection phase I includes a viscous term and a source term. The time integration is solved by the Euler explicit scheme. The spatial derivatives are computed by applying the central differencing method.

$$\frac{u_i^{**} - u_i^*}{\Delta t} = \frac{2\mu}{\rho^*}\frac{\partial}{\partial x_j}(S_{ij}^* - \frac{1}{3}\delta_{ij}S_{kk}^*) + f_i \tag{2.11}$$

where $*$ denotes intermediate variables calculated from the advection phase, $**$ denotes intermediate variables obtained from the non-advection phase I.

For the non-advection phase II, a Poisson-type equation can be obtained from Eqs. (2.9) and (2.10):

$$\frac{\partial}{\partial x_i}(\frac{1}{\rho^*}\frac{\partial p^{n+1}}{\partial x_i}) = \frac{p^{n+1} - p^*}{\rho^* C_s^2 \Delta t^2} + \frac{1}{\Delta t}\frac{\partial u_i^{**}}{\partial x_i} \tag{2.12}$$

where $n+1$ denotes the calculated values of variables in the next time step. For incompressible flow, Eq. (2.12) becomes:

$$\frac{\partial}{\partial x_i}(\frac{1}{\rho^*}\frac{\partial p^{n+1}}{\partial x_i}) = \frac{1}{\Delta t}\frac{\partial u_i^{**}}{\partial x_i} \tag{2.13}$$

The pressure equation is discretized using the central differencing method. The bi-conjugate gradient stabilized method with Jacobi preconditioner (see Appendix B) is applied to solve the equation.

2.4 Discretization Method

A staggered Cartesian grid system, where different variables are stored in different locations within a grid, is used to discretize the computational domain. As shown in Fig. 2.2, four sets of nodes are embedded in the computational domain. The P nodes, denoted by circles, store the pressure values and other physical properties, such as the density of fluid ρ, the dynamic viscosity μ and the sound speed C_s. The U nodes (squares), the V nodes (triangles) and the W nodes (stars) store the velocity components in the x-axis, the y-axis and the z-axis, respectively. For each computational grid, the P node is located at the centre of the cell, the U node is on the right hand vertical cell surface, the V node is positioned at the back vertical cell surface, the W node is positioned at the upper horizontal cell surface. Care must be taken to evaluate the derivatives at different locations. In the formulations, the calculation of the following spatial derivatives are necessary. They are evaluated using the central difference method and are summarized in Appendix C.

2.5 Interface Capturing

The water entry problem is considered as a multi-phase problem involving water, air and solid phases. As Eqs. (2.12) and (2.13) are valid for all three phases, the

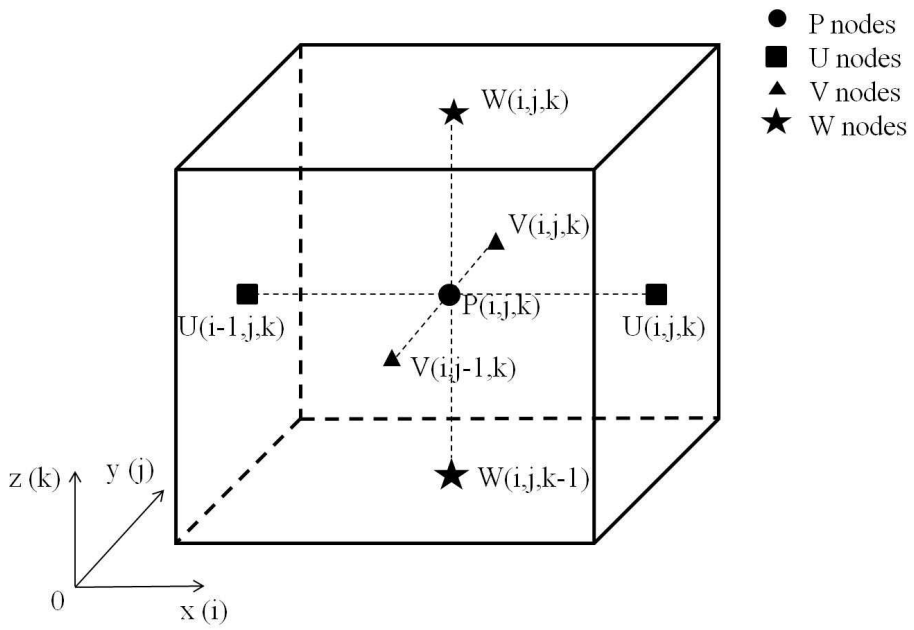

Figure 2.2: Staggered grid system

pressure field can be computed in the whole computational domain discretized by a fixed Cartesian grid. The solid body boundary and the water surface interface are immersed in the fixed Cartesian grids with a fractional volume technique. The boundary conditions on the interfaces between different phases are not needed. The density functions, ϕ_m, $m = 1, 2, 3$, are used to capture the interfaces between solid body, water and air, where ϕ_1 denotes the water phase, ϕ_2 represents the air phase, and ϕ_3 denotes the solid phase. The density functions have values between 0 and 1 and satisfy the following relationship at each grid node:

$$\sum_{m=1}^{3} \phi_m = 1.0 \tag{2.14}$$

At each time step, ϕ_3, is calculated from the position of the rigid body and the volume fraction of a grid cell inside the rigid body. The volume fraction for grid

(i, j, k) is determined by using the Gaussian quadratures as follows:

$$\begin{aligned}\phi_3(i,j,k) &= \frac{1}{\Delta x \Delta y \Delta z} \iiint_{\Omega} \phi_3(x,y,z) dx dy dz \\ &= \frac{1}{\Delta x \Delta y \Delta z} \sum_{a=1}^{N} \sum_{b=1}^{N} \sum_{c=1}^{N} w_a w_b w_c \mid J \mid \phi_3(X_a, Y_b, Z_c)\end{aligned} \tag{2.15}$$

where Ω is the grid cell at (i, j, k), $\phi_3(x, y, z) = 1$ if a point (x, y, z) is inside or on the solid body surface, and $\phi_3(x, y, z) = 0$ otherwise, N is the number of Gaussian points, w's are weights, X's, Y's and Z's are the coordinates at Gaussian points and J is the Jacobian of the transformation between the global and local coordinate system.

The density function of water phase, ϕ_1, is obtained by solving the advection equation, Eq. (2.16), using the THINC/WLIC interface capturing scheme, and ϕ_2 is determined from Eq. (2.14) at each computational cell.

$$\frac{\partial \phi_1}{\partial t} + u_i \frac{\partial \phi_1}{\partial x_i} = 0 \tag{2.16}$$

Eq. (2.16) can be solved by applying the CIP method described in a previous section. This research also studied two other interface capturing schemes, the THINC scheme and the THINC/WLIC scheme. The THINC/WLIC scheme, proposed by Yokoi [107], is a combination of the WLIC method and the THINC scheme. The THINC scheme, proposed by Xiao et al. [95] for incompressible free surface flow, allows for conservation of mass as well as reduced oscillation and smearing on the interfaces. The formulation of the one-dimensional THINC scheme is described below. Multi-dimensional applications are performed by the dimensional splitting method so that only one-dimensional formulation is needed.

The one-dimensional advection equation, Eq. (2.16), can be written in the con-

servation form as follows (in x-axis):

$$\frac{\partial \phi_1}{\partial t} + \frac{\partial (u\phi_1)}{\partial x} = \phi_1 \frac{\partial u}{\partial x} \tag{2.17}$$

where u is the velocity field and is a function of t and x. Eq. (2.17) is discretized using a finite volume method over a computational cell $[x_{P\{i-1/2\}}, x_{P\{i+1/2\}}]$ and a time step $[t^n, t^{n+1}]$ and yields:

$$\begin{aligned} \bar{\phi_1}^{n+1} =& \bar{\phi_1}^{n} - \frac{\Psi_{P\{i+1/2\}} - \Psi_{P\{i-1/2\}}}{\Delta x_i} \\ &+ \frac{\Delta t}{\Delta x_i} \bar{\phi_1}^{n} (u^n_{P\{i-1/2\}} - u^n_{P\{i+1/2\}}) \end{aligned} \tag{2.18}$$

where $\bar{\phi_1}^{n} = \frac{1}{\Delta x_i} \int_{x_{P\{i-1/2\}}}^{x_{P\{i+1/2\}}} \phi_1 dx$ is the cell-averaged density function of water at time instance t^n, $\Psi_{P\{i+1/2\}} = \int_{t^n}^{t^{n+1}} (u\phi_1)_{P\{i+1/2\}} dt$ is the flux across the cell boundary $x = x_{P\{i+1/2\}}$ over the time step $\Delta t = t^{n+1} - t^n$, $\Delta x_i = x_{P\{i+1/2\}} - x_{P\{i-1/2\}}$. The fluxes on cell boundaries are calculated by a semi-Lagrangian method. Instead of using a polynomial function as in the CIP method, the THINC scheme uses a stepwise modified hyperbolic tangent function to approximate the profile in the upwind cell:

$$\Gamma_i(x) = \frac{1}{2} \left\{ 1 + \gamma \tanh \left[\beta \left(\frac{x - x_{P\{i-1/2\}}}{\Delta x_i} - \delta \right) \right] \right\} \tag{2.19}$$

where γ, β and δ are parameters to be determined. $\beta = 3.5$, as suggested by Xiao et al. [95] and Yokoi [107], is used in this work. δ is calculated by solving the following equation:

$$\bar{\phi_1}^{n} = \frac{1}{\Delta x_i} \int_{x_{P\{i-1/2\}}}^{x_{P\{i+1/2\}}} \Gamma_i(x) dx \tag{2.20}$$

γ is determined by:

$$\gamma = \begin{cases} 1 & \text{if } \bar{\phi}_{1,i+1} \geq \bar{\phi}_{1,i-1} \\ -1 & \text{if } \bar{\phi}_{1,i+1} < \bar{\phi}_{1,i-1} \end{cases} \tag{2.21}$$

After $\Gamma(x)$ is determined in each cell, the fluxes at the cell boundaries can be calculated by using it in the upwind cell. The fluxes are then later used in updating $\bar{\phi_1}^{n+1}$. The detailed formulation of the THINC scheme can be found in the work of [95] and [31].

Yokoi [107] improved the multi-dimensional THINC scheme by superimposing three line interfaces along x, y and z directions, $\phi_{1,x}$, $\phi_{1,y}$ and $\phi_{1,z}$, respectively. The line interfaces are constructed like the classic simple line interface calculation (SLIC) method or the VOF by Hirt and Nichols [25]. By making use of the surface normal, $\vec{n} = (n_x, n_y, n_z)^T$, the three line interfaces are combined using weights:

$$\phi_1 = w_x(\vec{n})\phi_{1,x} + w_y(\vec{n})\phi_{1,y} + w_z(\vec{n})\phi_{1,z} \tag{2.22}$$

where $w_x(\vec{n})$,$w_y(\vec{n})$ and $w_z(\vec{n})$ are the weights calculated from the surface normal vectors, $\vec{n}$.

$$\begin{aligned} w_x &= \frac{|n_x|}{|n_x| + |n_y| + |n_z|} \\ w_y &= \frac{|n_y|}{|n_x| + |n_y| + |n_z|} \\ w_z &= \frac{|n_z|}{|n_x| + |n_y| + |n_z|} \end{aligned} \tag{2.23}$$

$\phi_{1,x}$, $\phi_{1,y}$ and $\phi_{1,z}$ are the constructed line interfaces. They satisfy:

$$\begin{aligned} \bar{\phi_1} &= \frac{1}{\Delta x \Delta y \Delta z} \int_{x_{P\{i-1/2\}}}^{x_{P\{i+1/2\}}} \int_{y_{P\{j-1/2\}}}^{y_{P\{j+1/2\}}} \int_{z_{P\{k-1/2\}}}^{z_{P\{k+1/2\}}} \phi_{1,x}(x,y,z)dxdydz \\ &= \frac{1}{\Delta x \Delta y \Delta z} \int_{x_{P\{i-1/2\}}}^{x_{P\{i+1/2\}}} \int_{y_{P\{j-1/2\}}}^{y_{P\{j+1/2\}}} \int_{z_{P\{k-1/2\}}}^{z_{P\{k+1/2\}}} \phi_{1,y}(x,y,z)dxdydz \\ &= \frac{1}{\Delta x \Delta y \Delta z} \int_{x_{P\{i-1/2\}}}^{x_{P\{i+1/2\}}} \int_{y_{P\{j-1/2\}}}^{y_{P\{j+1/2\}}} \int_{z_{P\{k-1/2\}}}^{z_{P\{k+1/2\}}} \phi_{1,z}(x,y,z)dxdydz \end{aligned} \tag{2.24}$$

In the THINC/WLIC scheme, $\phi_{1,x}$ is constructed using Eq. 2.19 and $\phi_{1,z} = \phi_{1,y} = \bar{\phi}_1$ for the advection in the direction along the x-axis. Similar formulations are obtained in the y-axis and the z-axis. Considering the constructed line interfaces, fluxes can then be calculated as below:

$$\Psi_{i+1/2,j,k} = w_x \Psi_{x,i+1/2,j,k} + (1 - w_x)\bar{\phi}_{1,is,j,k} u_{i+1/2,j,k} \Delta t \tag{2.25}$$

$$\Psi_{i,j+1/2,k} = w_y \Psi_{y,i,j+1/2,k} + (1 - w_y)\bar{\phi}_{1,i,js,k} v_{i,j+1/2,k} \Delta t \tag{2.26}$$

$$\Psi_{i,j,k+1/2} = w_z \Psi_{z,i,j,k+1/2} + (1 - w_z)\bar{\phi}_{1,i,j,ks} w_{i,j,k+1/2} \Delta t \tag{2.27}$$

where $\Psi_{x,i+1/2,j,k}$, $\Psi_{y,i,j+1/2,k}$ and $\Psi_{z,i,j,k+1/2}$ are the fluxes calculated based on the THINC scheme, u, v and w are the velocity components and the subscripts is, js and ks denote the upwind grids in the x, y and z directions, respectively. Details on the formulations can be found in the work of Yokoi [107].

2.6 Parallel Computing Algorithm

Since Eqs. (2.12) and (2.13) are solved for all three phases and the pressure distribution is solved in the whole computational domain, parallel computing techniques can be applied in a straightforward way. In this work, a message passing interface (MPI) scheme is employed. As shown in Fig. 2.3, the whole computational domain is firstly partitioned into $N_{proc} = NX_{proc} \times NY_{proc} \times NZ_{proc}$ sub-domains based on a Cartesian topology. Similar or equal number of grids are evenly distributed in these sub-domains. Each sub-domain is then assigned to one processor or CPU with a unique identity number. The Cartesian topology was applied to handle the assignment of processors to sub-domains. The identity numbers of the neighbouring

processors are then acquired and stored. Each processor uses its local memory.

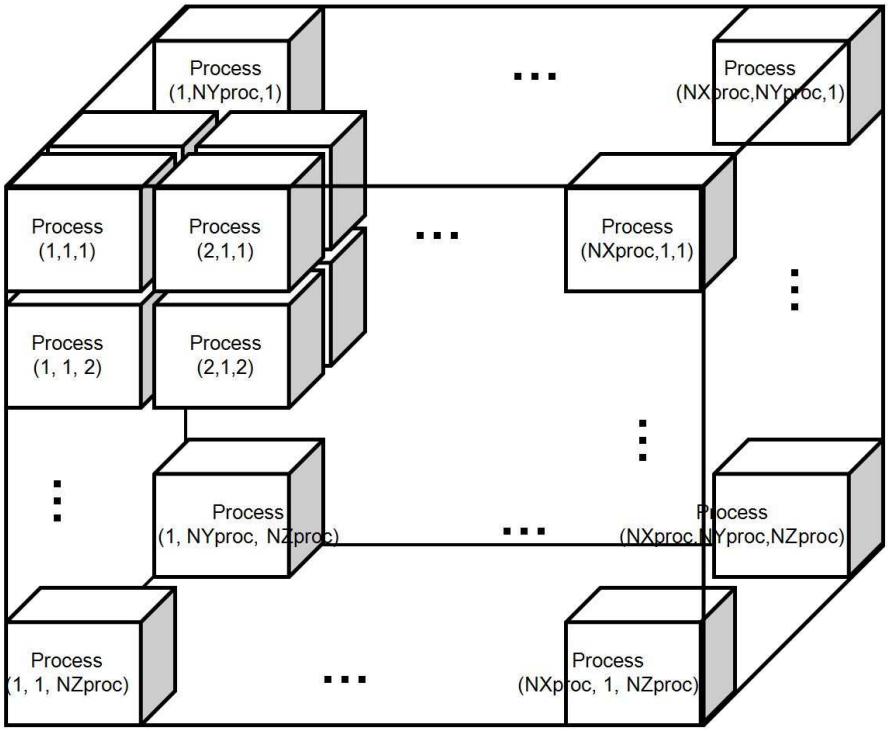

Figure 2.3: Illustration of domain decomposition

Since the computation of spatial derivatives on the boundary grids in a sub-domain requires values in neighbouring processors (refer to Section 2.4), communications with neighbouring processors are involved to share the values on the boundaries between sub-domains. In the parallel computations, all processors need to store one additional layer of nodes on the boundaries. The values in these nodes need to be updated from neighbouring processors before they can be used. The communications between processors are achieved by the MPI approach.

The speed-up performance was studied by simulating the water entry of a 3-D wedge using various numbers of processors on a work station. It can be seen from

Fig. 2.4 that the parallelization speeds up the simulation. As an illustration, the water entry of a 3-D wedge section with prescribed motion from Zhao et al. [111] was simulated on a workstation with 2 Intel Xeon X5670 CPUs (2.93 GHz), providing 24 computing cores. $273,735$ grids were used and 240 time steps were solved. The computation consumed 12 minutes, comparing 110 minutes with single CPU.

It should be noted that very minor (less than 0.01%) difference in the predicted slamming force can be found for the water entry case when varying the number of processors and using different partition schemes. This is due to the machine error which can be built up in the computations. However, the difference is still negligible.

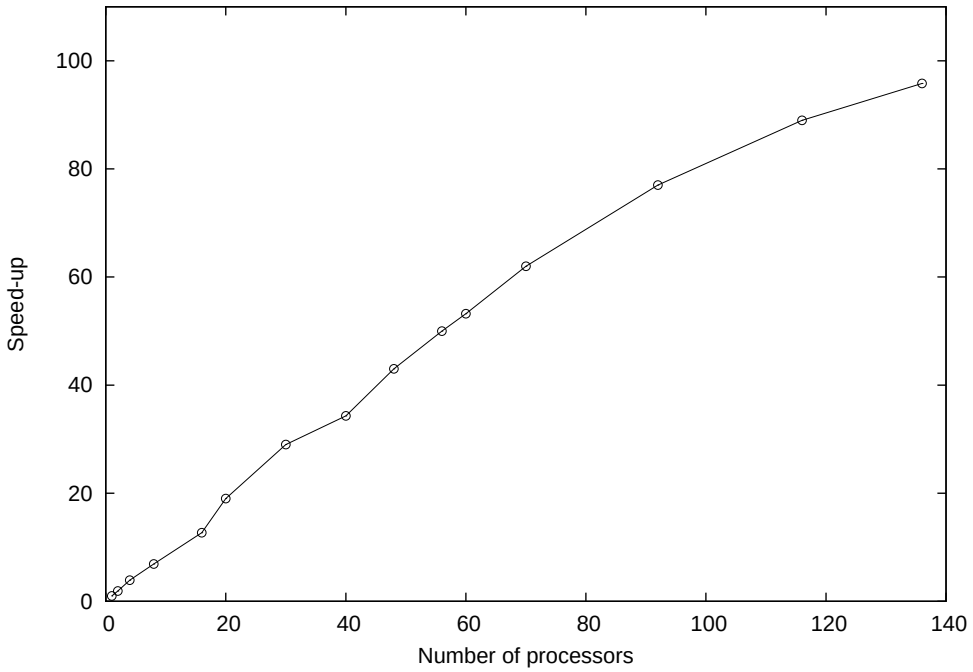

Figure 2.4: Speed-up performance

2.7 Solving the Equations of Motion

Once the pressure distribution in the computational domain is obtained, the hydrodynamic force acting on the solid body can be calculated by integrating the pressure on its surface. By applying Gauss's theorem, the hydrodynamic force, $\vec{F} = (F_x, F_y, F_z)^T$ can be expressed as:

$$F_x = -\oint_\Omega \frac{\partial p}{\partial x}\phi_2 d\Omega \tag{2.28}$$

$$F_y = -\oint_\Omega \frac{\partial p}{\partial y}\phi_2 d\Omega \tag{2.29}$$

$$F_z = -\oint_\Omega \frac{\partial p}{\partial z}\phi_2 d\Omega \tag{2.30}$$

where F_x, F_y and F_z are the force components in x, y and z direction, Ω denotes the computational domain, ϕ_2 is the density function of the solid phase. The moment, $\vec{M} = (M_x, M_y, M_z)^T$, with respect to the center of gravity, $\vec{x}_c = (x_c, y_c, z_c)$, can be obtained as:

$$M_x = -\oint_\Omega \left[(y - y_c)\frac{\partial p}{\partial z} - (z - z_c)\frac{\partial p}{\partial y}\right]\phi_2 d\Omega \tag{2.31}$$

$$M_y = -\oint_\Omega \left[(z - z_c)\frac{\partial p}{\partial x} - (x - x_c)\frac{\partial p}{\partial z}\right]\phi_2 d\Omega \tag{2.32}$$

$$M_z = -\oint_\Omega \left[(x - x_c)\frac{\partial p}{\partial z} - (z - z_c)\frac{\partial p}{\partial x}\right]\phi_2 d\Omega \tag{2.33}$$

After the hydrodynamic forces and moment are obtained, the translational and rotational motions of the solid body can be obtained by solving the equations of motion. The state variable vector for a rigid body, $\mathbf{SV}(t)$, can be defined as:

$$\mathbf{SV}(t) = \begin{pmatrix} \vec{x}_c(t) \\ \vec{q}(t) \\ \vec{P}(t) \\ \vec{L}(t) \end{pmatrix} \tag{2.34}$$

where $\vec{x}_c(t)$ is the center of gravity in the global coordinate system, $\vec{q}(t) = (q_0, q_1, q_2, q_3)^T$ is the quaternion vector denoting the orientation of the solid body, $\vec{P}(t) = (P_x, P_y, P_z)^T$ is the translational momentum vector, and $\vec{L}(t) = (L_x, L_y, L_z)^T$ is the angular momentum vector. The equations of motion can be written in the vector form as follows:

$$\frac{d}{dt}\mathbf{SV}(t) = \frac{d}{dt}\begin{pmatrix} \vec{x}_c(t) \\ \vec{q}(t) \\ \vec{P}(t) \\ \vec{L}(t) \end{pmatrix} = \begin{pmatrix} \vec{v}(t) \\ \frac{1}{2}\vec{\omega}(t)\vec{q}(t) \\ \vec{F}(t) \\ \vec{M}(t) \end{pmatrix} \tag{2.35}$$

where the multiplication $\vec{\omega}(t)\vec{q}(t)$ denotes the quaternion multiplication between the quaternions $(0, \vec{\omega})$ and $\vec{q}$, $\vec{v}(t)$ is the linear velocity vector and $\vec{\omega}(t)$ is the angular velocity vector. In this work, the Euler explicit scheme is applied to solve the equations of motion. Thus, the following expression can be obtained:

$$\begin{pmatrix} \vec{x}_c(t) \\ \vec{q}(t) \\ \vec{P}(t) \\ \vec{L}(t) \end{pmatrix}^{n+1} = \begin{pmatrix} \vec{v}(t) \\ \frac{1}{2}\vec{\omega}(t)\vec{q}(t) \\ \vec{F}(t) \\ \vec{M}(t) \end{pmatrix} \Delta t + \begin{pmatrix} \vec{x}_c(t) \\ \vec{q}(t) \\ \vec{P}(t) \\ \vec{L}(t) \end{pmatrix}^{n} \tag{2.36}$$

The external forces and moments, $\vec{F}(t)$ and $\vec{M}(t)$ are calculated from Eqs. (2.28) - (2.33). The linear velocity, $\vec{v}(t)$, and the angular velocity, $\vec{\omega}(t)$, can be calculated by:

$$\vec{v}(t) = \frac{\vec{P}(t)}{m} \tag{2.37}$$

$$\vec{\omega}(t) = I(t)^{-1}\vec{L}(t) \tag{2.38}$$

where m is the mass of the solid body, $I(t)$ is the inertia tensor of the solid body about its center of gravity specified in the global coordinate system and it can be

evaluated by $I(t) = R(t)I_0R(t)^T$. I_0 is the inertia tensor specified in the body fixed coordinate system and is constant over the simulation. m and I_0 are known before the simulation starts. $R(t)$ is the rotation matrix and is changing as the orientation of the solid body changes. It can be calculated using the quaternions:

$$R(t) = \begin{pmatrix} 1-2q_2^2-2q_3^2 & 2q_1q_2-2q_0q_3 & 2q_1q_3+2q_0q_2 \\ 2q_1q_2+2q_0q_3 & 1-2q_1^2-2q_3^2 & 2q_2q_3-2q_0q_1 \\ 2q_1q_3-2q_0q_2 & 2q_2q_3+2q_0q_1 & 1-2q_1^2-2q_2 \end{pmatrix} \tag{2.39}$$

2.8 Numerical Wave Tank

A three-dimensional numerical wave tank is generated by simulating a physical wave tank. As shown in Fig. 2.5, a piston-type wave maker is positioned in one end of the tank. Regular water waves can be produced by imposing a prescribed horizontal velocity $U_b(t)$ on the piston-type wave maker. A sinusoidal motion is defined for the wave maker.

$$U_b(t) = \frac{S_b}{2} 2\pi f_b \cos(2\pi f_b t) \tag{2.40}$$

where S_b and f_b are the stroke and the frequency of the wave maker.

Based on the wave maker theory by Dean and Dalrymple [14], the relationship between the wave maker stroke, S_b, and the generated wave height, H_w, for the piston-type wave maker is:

$$\frac{H_w}{S_b} = \frac{2(\cosh 2k_wD - 1)}{\sinh 2k_wD + 2k_wD} \tag{2.41}$$

where k_w is the wave number and D is the water depth.

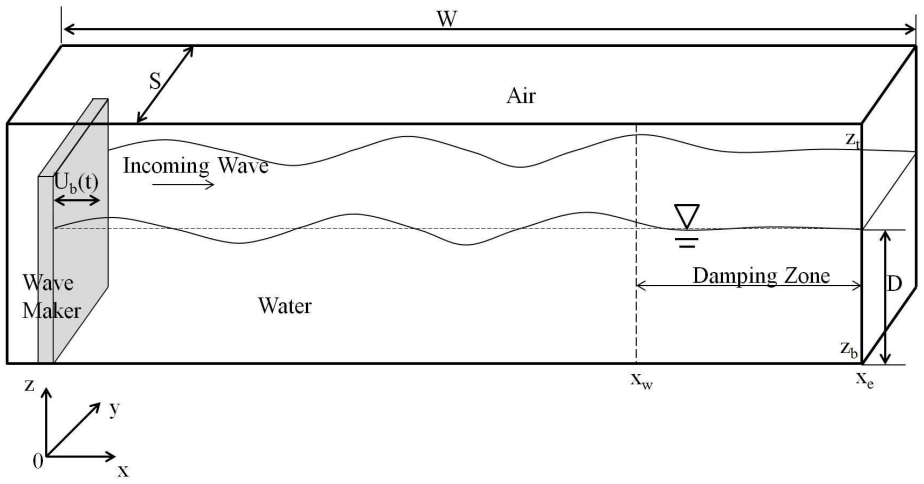

Figure 2.5: Numerical wave tank

In order to perform simulations in a numerical wave tank with a finite computational domain, a non-reflective outlet boundary condition is required. In this work, an artificial damping zone is employed near the downstream boundary ($X_w < x < X_e$, $Z_b < z < Z_t$). A vertical artificial damping force (in z direction), f_d, is added to the body force term in Eq. 2.2.

$$f_d(x,z) = \frac{1}{2\Delta t}\left(\frac{x - X_w}{X_w - X_e}\right)^a \left(1 - |\frac{z - Z_f}{Z_t - Z_b}|\right)^b w \tag{2.42}$$

where Z_f is the position of the average free surface, w is the velocity component in z direction, $a = 4$ and $b = 1$. The slip wall boundary condition is implemented on other boundaries.

2.9 Evaluation of Spatial Discretization Errors

Uncertainties in the numerical solutions due to spatial discretization errors are evaluated in this work using the grid convergence index (GCI) method proposed by Celik

et al. [7]. The procedure based on the Richardson extrapolation is briefly summarized as follows:

- Three sets of grid are chosen with grid sizes, h_1, h_2 and h_3, where the grid h_1 is the finest. Computations are carried out using these three grids and the values of interested variables are obtained, for example, the maximum slamming force. The results are denoted as α_1, α_2 and α_3, where α represents the maximum slamming force.

- Introducing $r_{21} = h_2/h_1$ and $r_{32} = h_3/h_2$, the apparent order k is calculated using:

$$k = \frac{1}{\ln(r_{21})} \mid \ln \mid \varepsilon_{32}/\varepsilon_{21} \mid + q(k) \mid \tag{2.43}$$

  where $\varepsilon_{32} = \alpha_3 - \alpha_2$, $\varepsilon_{21} = \alpha_2 - \alpha_1$, $q(k) = \ln\left[\dfrac{(r_{21})^k - s}{(r_{32})^k - s}\right]$, $s = \text{sign}(\varepsilon_{32}/\varepsilon_{21})$ and $q(k) = 0$ in the case of $r_{21} = r_{32}$.

- The extrapolated values are calculated from:

$$\alpha_e^{21} = \left[(r_{21})^k \alpha_1 - \alpha_2\right] / \left[(r_{21})^k - 1\right] \tag{2.44}$$

- The approximate relative error, the extrapolated relative error and the GCI are obtained using the following equations, respectively:

$$e_a^{21} = \mid \frac{\alpha_1 - \alpha_2}{\alpha_1} \mid \tag{2.45}$$

$$e_e^{21} = \mid \frac{\alpha_e^{21} - \alpha_1}{\alpha_e^{21}} \mid \tag{2.46}$$

$$\text{GCI} = \frac{1.25 e_a^{21}}{(r_{21})^k - 1} \tag{2.47}$$

Chapter 3

Water Entry of Two-dimensional Bodies in Calm Water

This chapter presents numerical solutions of 2-D wedges and ship sections entering calm water. The present study focused on the prediction of local pressures/forces on wedges with different tilted angles and a ship section with different drop heights. Three different schemes for interface capturing were compared, including the CIP method, the THINC method and the THINC/WLIC method. The incompressible and the compressible solvers were used to examine their effects on the solutions. A motion solver was developed to enable the free fall motion simulation. Convergence studies were carried out using various domain sizes, grid sizes and time steps. The grid convergence index (GCI) was employed to estimate the uncertainties due to the spatial discretization errors. In the validation studies, experimental data from model tests of a 2-D wedge and a 2-D ship section conducted by KRISO (Kim et al. [38]) were used. Table 3.1 summarises the test conditions. It should be pointed out

that a stiff spring was installed near the bottom of the guide rail in the experiments to decelerate the tested body and prevent it from hitting the tank bottom. In the numerical simulations, the spring was not modelled since the focus was on the peak forces and pressures at the instants of water impact rather than at the subsequent stages. In the computations, 2-D non-uniform Cartesian grids were employed and the time step was kept constant.

Table 3.1: Summary of 2-D cases

Case ID	Body shape	Tilted angle (degree)	Drop height H_d (m)
A	Wedge	0	0.5
B	Wedge	20	0.5
C	Ship section	0	0.17
D	Ship section	0	0.3

The time histories of local slamming force and pressure were compared with experimental results. For each force/pressure time history, the peak value P_0 or F_0, the rise time t_R, the delay time t_D, and the pressure/force momentum m_0 were presented. They are defined according to Fig. 3.1. The time lag between the pressure peak occurs on different locations were examined as well.

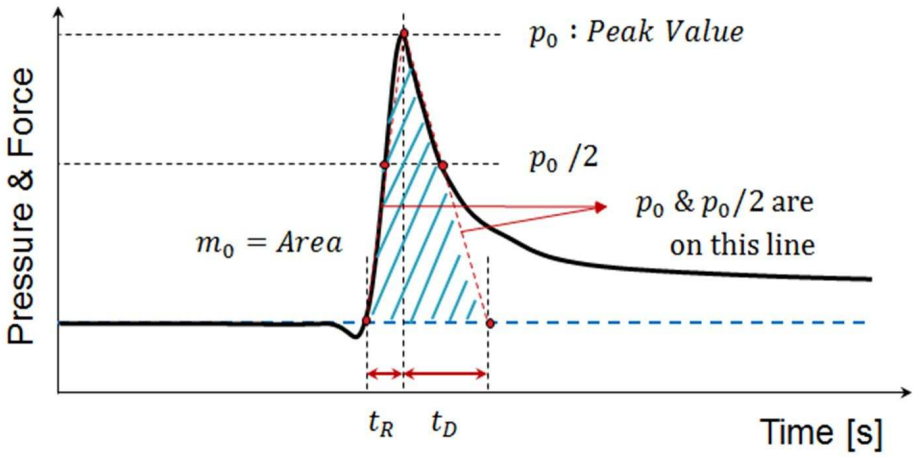

Figure 3.1: Definitions of parameters for 2-D cases (from KRISO)

3.1 Case A: Two-dimensional Wedge

The deadrise angle of the wedge is 30°. The width of the wedge is 0.6 m. The computational domain is illustrated in Fig. 3.2, where the width and the depth of the computational domain are denoted as W and D, respectively. The drop height was $H_d = 0.5$ m. In the experiments, a local force sensor and two local pressure sensors were installed and their locations are shown in Fig. 3.2. The force and pressure at the same locations were predicted in the simulations.

3.1.1 Sensitivity Studies

Sensitivity studies were carried out to investigate the effect of domain size, grid size and time step on the solution. The results presented below were based on the solutions using the THINC/WLIC interface capturing scheme, the incompressible solver and the prescribed body motion (i.e., the time histories of the drop velocities measured in

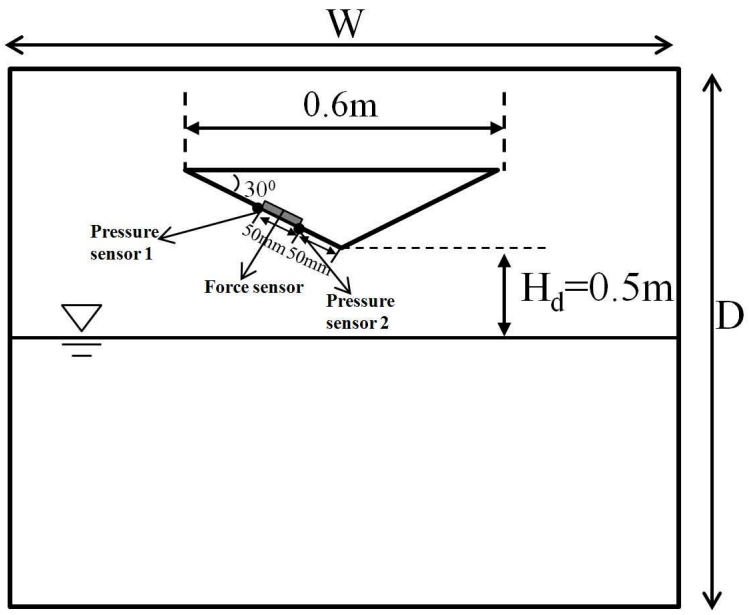

Figure 3.2: Computational domain for wedges

the experiments were used in the simulations). The prescribed body motion was used by default for the validation cases in this chapter, unless a free fall motion simulation was performed.

Domain Size. In the sensitivity study on the domain size, three domain widths ($W = 3$ m, 4 m and 6 m) and three domain depths ($D = 3$ m, 4 m and 6 m) were used. Time histories of the predicted local force and pressure are shown in Figs. 3.3 and 3.4 in comparison with experimental data. It can be seen that the results were not sensitive to the domain size. Therefore, $W = 3$ m and $D = 3$ m were used in the following studies.

Grid Size. Three sets of non-uniform grids with the minimum grid sizes, 0.008 m, 0.004 m and 0.002 m, were used in the grid sensitivity studies. Fine grids were concentrated near the body surface and the free surface. A summary of three sets of

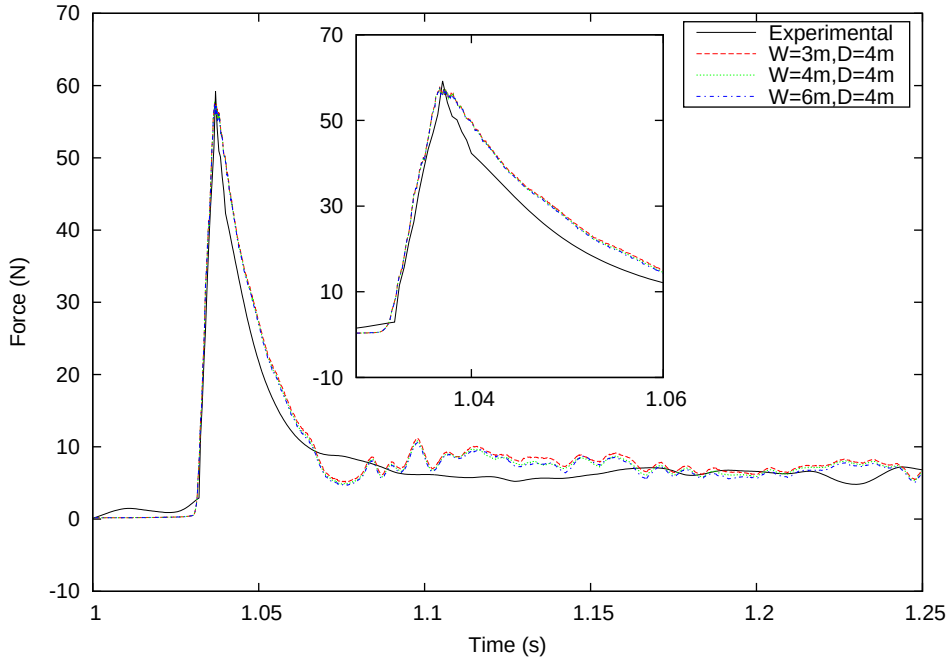

Figure 3.3: Local forces in convergence study on domain size (Case A)

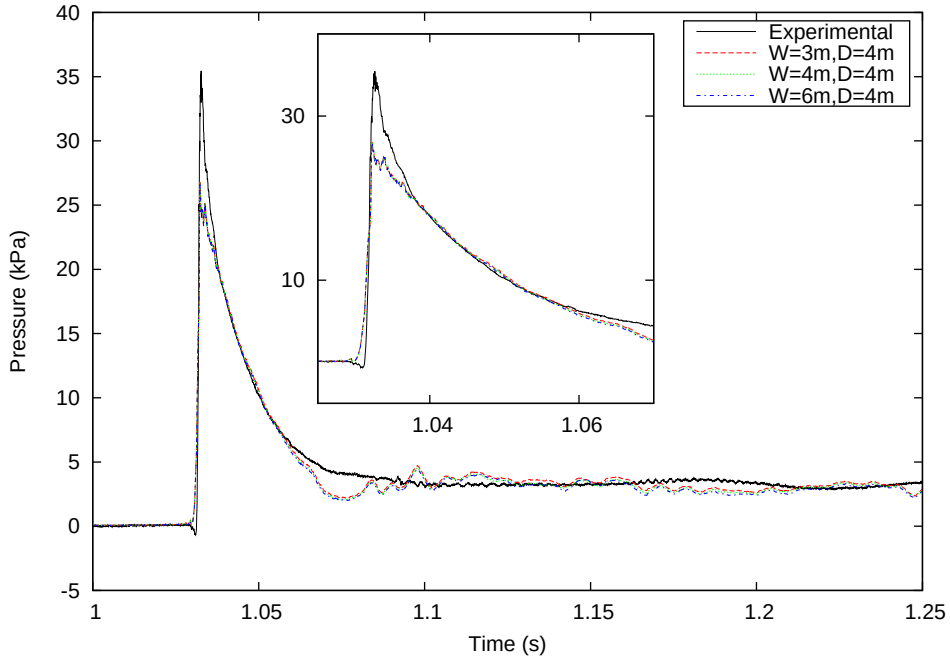

Figure 3.4: Local pressure at P1 in convergence study on domain size (Case A)

grids is given in Table 3.2. The number of grids varied from $88,000$ to $1,357,000$. As examples, the predicted local forces and local pressures at location, P1, are shown in Fig. 3.5 and 3.6, respectively, in comparison with the experimental data. The solutions were sensitive to the grid sizes and the results converged as the grid size was decreased. It can be observed that coarse grids led to lower predicted peak force/pressure and higher rise time.

Table 3.2: Summary of grids in the convergence studies (Cases A and B)

	Δx_{min} (m)	N_x	N_z	N_{total}
Grid 1	0.008	297	297	88,209
Grid 2	0.004	517	517	267,289
Grid 3	0.002	1,165	1,165	1,357,225

Based on the predicted peak pressures and rise times using the three sets of grids, the GCI's were evaluated and are summarized in Table 3.3, including the intermediate details. The uncertainties in the predicted peak pressure due to spatial discretization errors are under 1% and the uncertainties for the predicted t_R are around 5%.

Time Step. In the convergence studies on the time step, three time steps, 0.0001 s, 0.00005 s, and 0.000025 s were used. The predicted local forces are shown in Fig. 3.7 and compared with the experimental data. As shown in the figure, the numerical solution is insensitive to the time step. The time step of 0.0001 s was thus used in the following studies. The oscillations in the numerical results were thought due to the re-calculation of the solid color function according to the position of the solid body

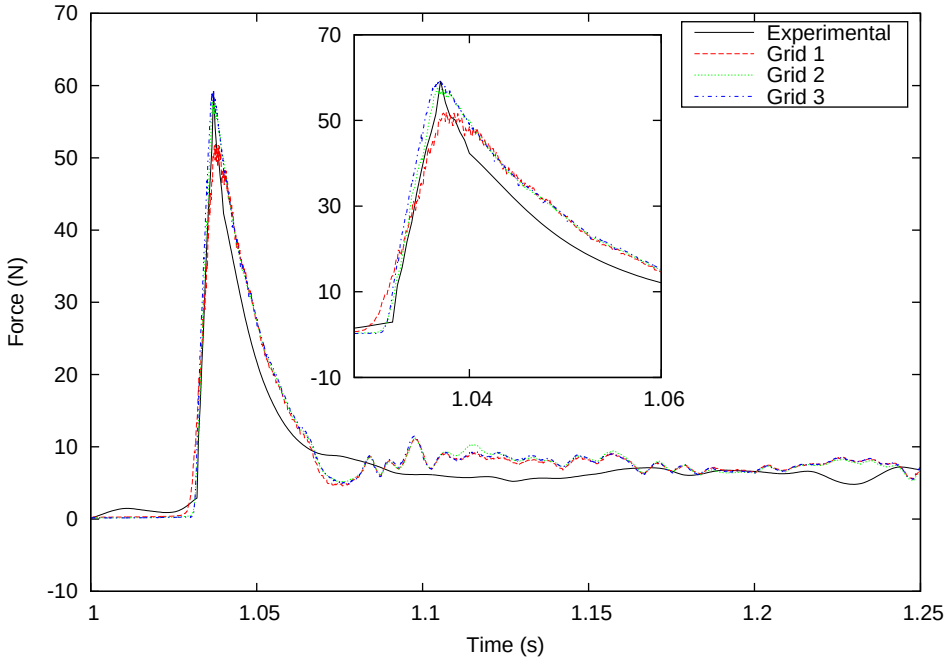

Figure 3.5: Local forces in convergence study on grids (Case A)

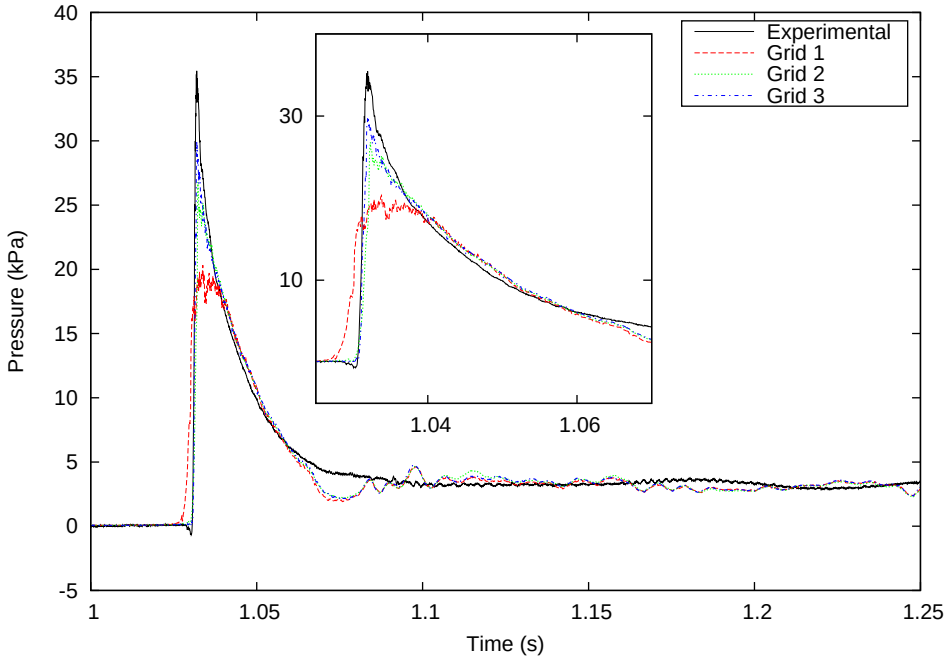

Figure 3.6: Local pressures at P1 in convergence study on grids (Case A)

Table 3.3: Uncertainties due to spatial discretization errors (Case A)

	P_0 at P1	P_0 at P2	t_R at P1	t_R at P2
α_1	29.88	27.55	0.0012	0.0031
α_2	28.76	27.32	0.0017	0.0033
α_3	20.32	24.59	0.0074	0.0038
k	2.92	3.56	3.51	1.32
α_e^{21}	30.05	27.57	0.0012	0.0030
e_a^{21}	3.7%	0.8%	41.7%	6.5%
e_e^{21}	0.6%	0.1%	4.2%	4.5%
GCI	0.7%	0.1%	5.0%	5.4%

at each time step.

3.1.2 Schemes for Interface Capturing

The effects of the interface capturing schemes, the CIP method, the THINC and the THINC/WLIC schemes, on the the predicted forces are shown in Fig. 3.8. It can be observed that the CIP method under-estimated the peak force while the THINC and the THINC/WLIC schemes gave similar predictions which agreed better with the experimental results. In addition, the predicted force using the CIP scheme did not reach to its peak value as quickly as that by the other two schemes, which means that the CIP method over-estimated the rise time.

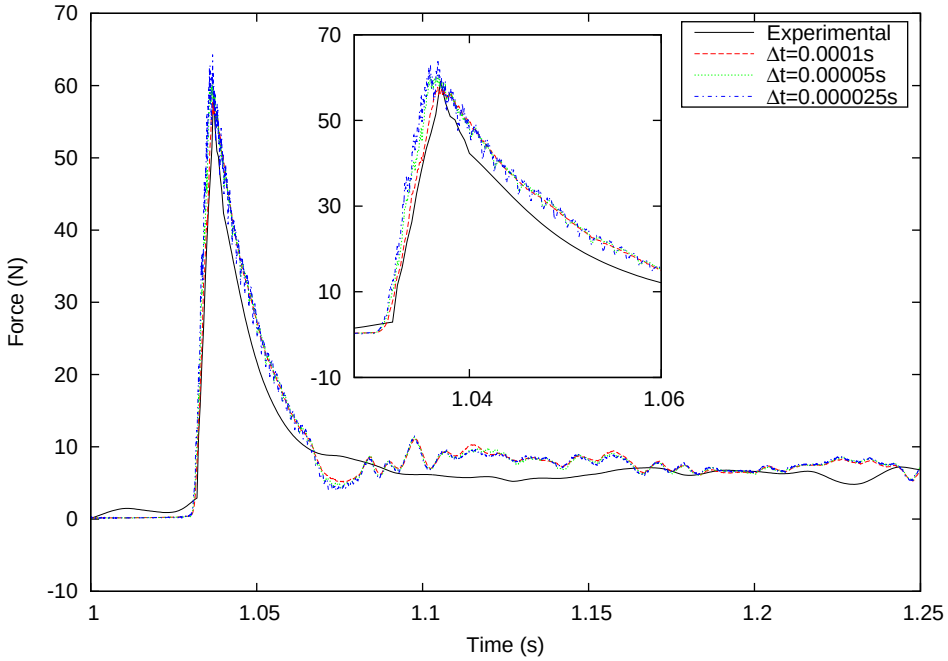

Figure 3.7: Local forces in convergence study on time step (Case A)

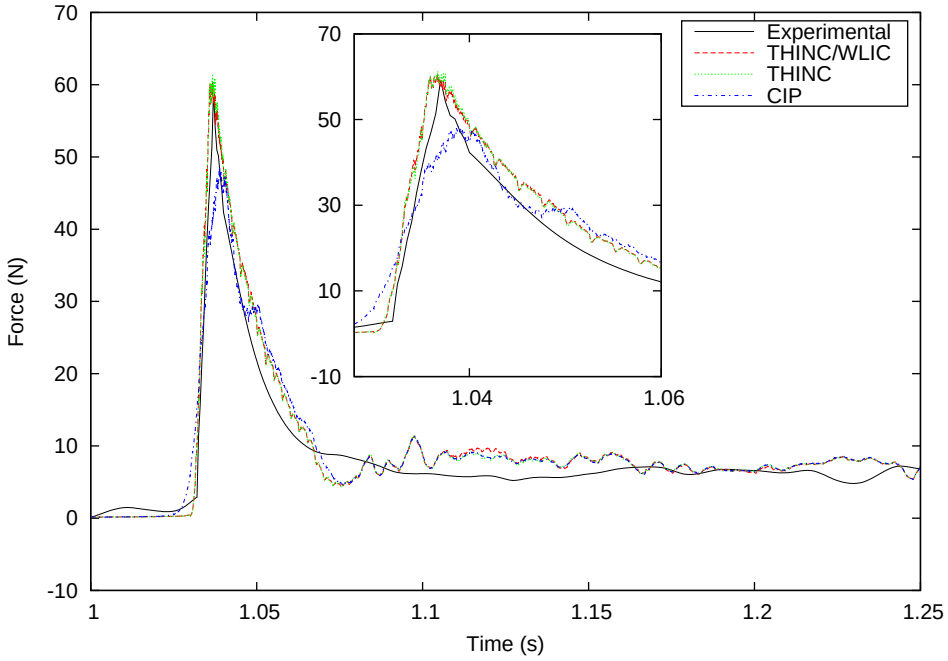

Figure 3.8: Local forces based on three interface capturing schemes (Case A)

3.1.3 Free Fall Motion

Prescribed motions were used in previous studies. In this section, the effect of free fall motion on the solution was investigated. In the simulation, the THINC/WLIC scheme and the incompressible solver were applied. The simulation started at $t = 1.0$ s, which is the same as that in the experimental tests. As indicated earlier, the restraining spring was not considered in the simulation. The simulation ended around $t = 1.25$ s just before the spring came into effect in the experiments. The predicted time history of the wedge velocity is compared with the experimental one in Fig. 3.9. The velocities were slightly under-predicted after the impact. Fig. 3.10 presents the predicted local force considering the free fall motion and those using prescribed motion. The predicted forces are in good agreements with the experimental data.

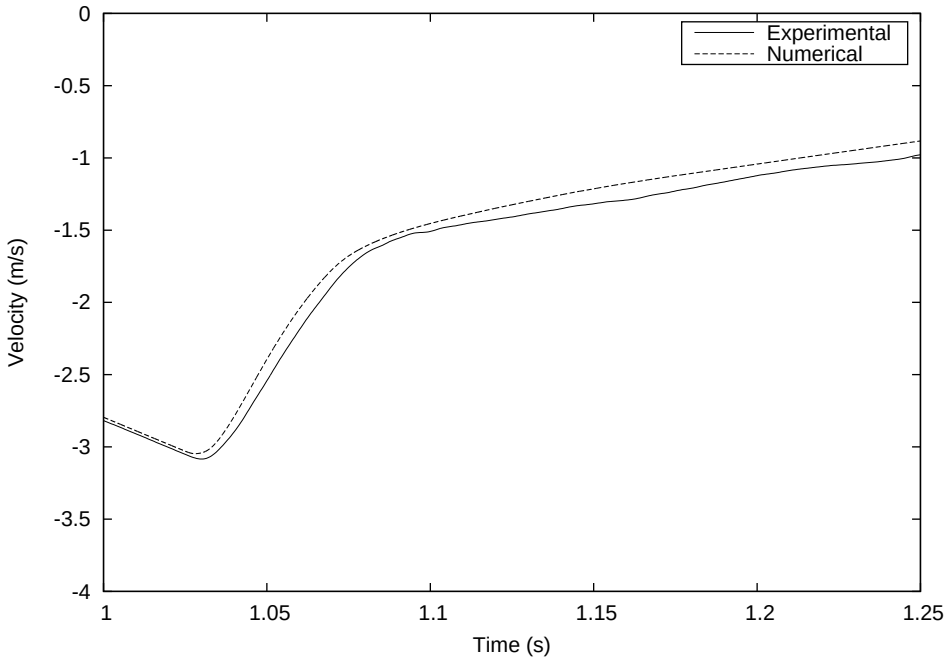

Figure 3.9: Drop velocity of wedge (Case A)

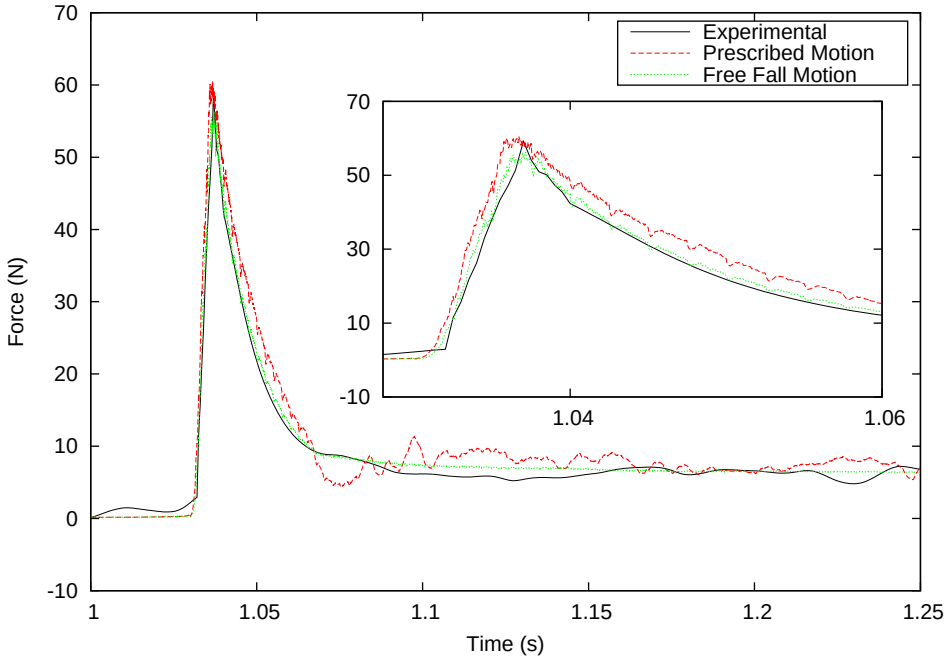

Figure 3.10: Local forces based on free fall motion (Case A)

3.1.4 Compressible Solver

The compressible solver was then examined, along with the THINC/WLIC scheme and the prescribed motion. The predicted local forces are compared with those based on the incompressible solver in Fig. 3.11. It is clear that the predicted forces are generally identical.

Table 3.4 summarizes all the results using the finest mesh, the incompressible solver with the THINC/WLIC scheme and the prescribed motion. Note that the relative errors were calculated based on the experimental results. The pressures and forces were well predicted. The predicted time difference between the peak pressures at the two pressure sensor locations, ΔT, was also in a good agreement with the experimental data.

Table 3.4: Summary of results (Case A)

		$P_0(kPa)$ or $F_0(N)$	$t_R(s)$	$t_D(s)$	$m_0(kPas$ or $Ns)$	ΔT
	CIP	29.88	0.0012	0.0226	0.36	0.0062
P1	Exp.	35.45	0.0015	0.0148	0.29	0.0067
	Error	16%	18%	52%	23%	8%
	CIP	27.55	0.0031	0.0181	0.29	
P2	Exp.	20.73	0.0034	0.0169	0.21	
	Error	33%	8%	7%	39%	
	CIP	59.25	0.0068	0.0241	0.91	
F	Exp.	59.22	0.0055	0.0174	0.68	
	Error	0%	24%	38%	35%	

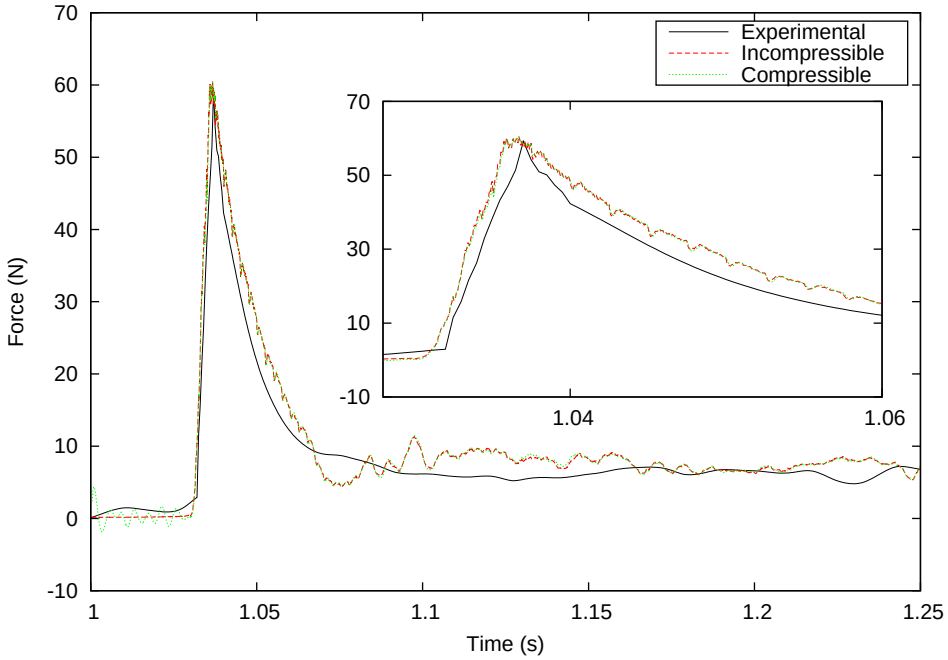

Figure 3.11: Local forces based on compressible and incompressible solvers (Case A)

3.2 Case B: Two-dimensional Tilted Wedge

The numerical set-up for the tilted wedge (20°) was similar as that for Case A (Fig. 3.2). In the model tests, the locations of the pressure and force sensors remained the same on the body surface. The sensitivity studies on the domain size were also conducted and it was found that the results are not sensitive to the domain size. In the following cases, the computational domain was set with a width of $W = 3$ m and a depth of $D = 3$ m. In the computations, the incompressible solver with the THINC/WLIC scheme and the prescribed drop velocity (from the drop test) was employed.

Figs. 3.12 and 3.13 present the results of convergence studies on the grid size and the time step, respectively. The grids are summarized in Table 3.2. It can be

observed that the solution is sensitive to the grid size. The coarse grid led to lower predicted peak forces. The solution is relatively insensitive to the time step.

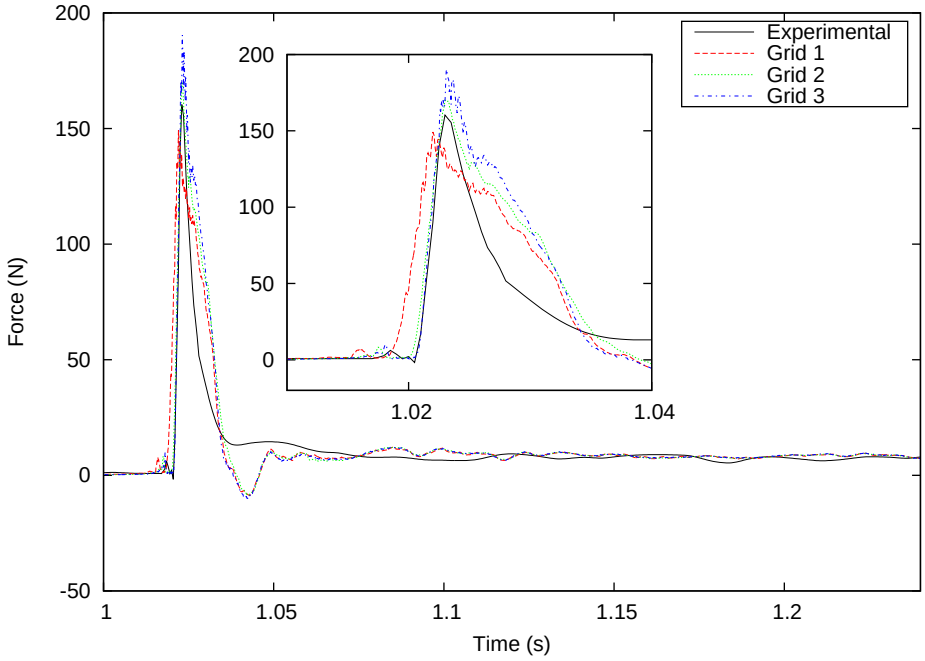

Figure 3.12: Local forces in convergence study on grid size (Case B)

Based on the predicted peak pressures and rise times using the three sets of grids, the GCI's were evaluated and are summarized in Table 3.5. The uncertainties in the predicted variables are less than 7%.

The three schemes for interface capturing were also examined for this case. The predicted forces are compared in Fig. 3.14. Similarly, the results are sensitive to the scheme for interface capturing. The peak force and the rise time were better predicted by the THINC and THINC/WLIC schemes.

The free fall motions were predicted using the THINC/WLIC scheme and the incompressible solver with the same starting time ($t = 1.0$ s) in the model tests. The

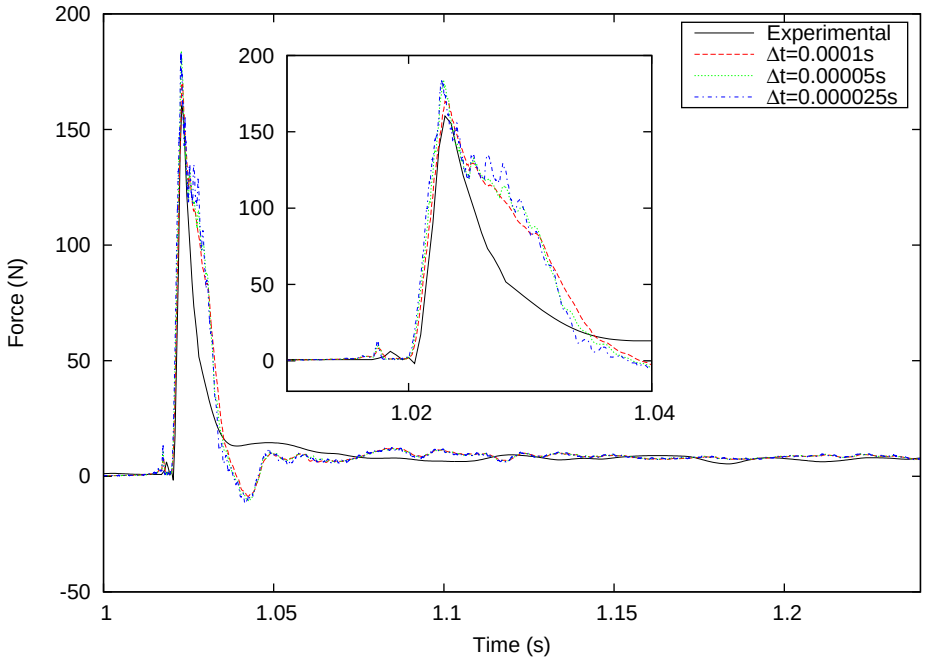

Figure 3.13: Local forces in convergence study on time step (Case B)

Table 3.5: Uncertainties due to spatial discretization errors (Case B)

	P_0 at P1	P_0 at P2	t_R at P1	t_R at P2
α_1	72.13	105.52	0.0007	0.0012
α_2	65.99	98.28	0.0010	0.0012
α_3	49.91	70.68	0.0051	0.0020
k	1.39	1.93	3.77	6.30
α_e^{21}	75.92	108.09	0.0007	0.0012
e_a^{21}	8.5%	6.9%	42.9%	0.8%
e_e^{21}	5.0%	2.4%	3.5%	0.0%
GCI	6.6%	3.0%	4.2%	0.0%

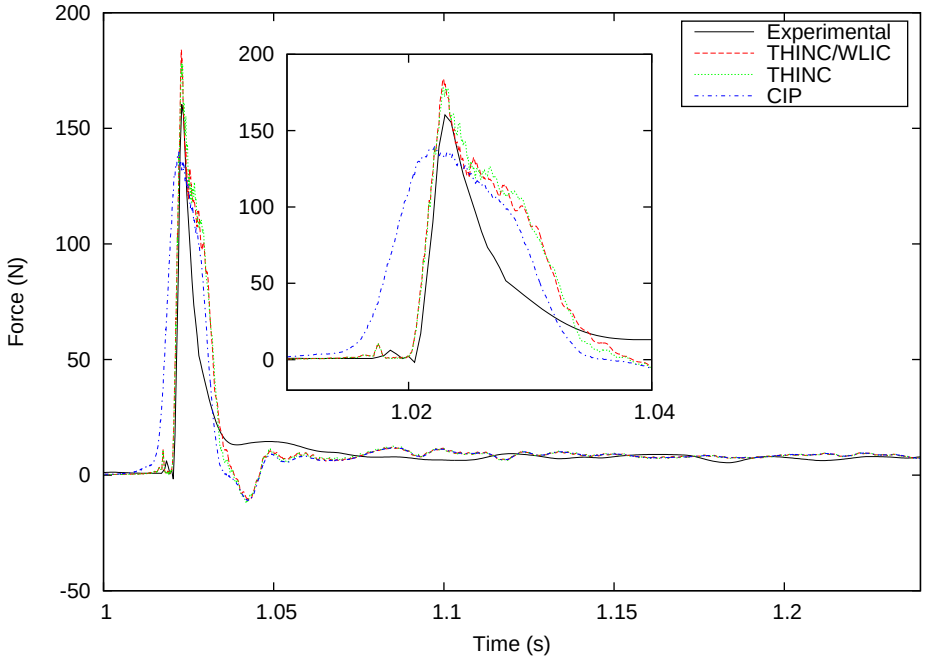

Figure 3.14: Local forces based on three interface capturing schemes (Case B)

predicted wedge velocities are compared with the experimental results in Fig. 3.15. Reasonable agreement can be observed. The predicted velocity is generally smaller than the measurement after the water impact. Figure 3.16 presents the predicted local forces using the free fall motion solver and the prescribed motions. In this case, the peak force was however under-estimated using the free fall motion solver.

The compressible solver along with the THINC/WLIC scheme and prescribed motion was also examined. The predicted local forces are compared with those based on the incompressible solver in Fig. 3.17. No significant difference can be observed in the predicted force using compressible and incompressible solvers.

As a summary, the results using the finest mesh, the incompressible solver, the THINC/WLIC scheme for interface capturing, and the prescribed motion are presented in Table 3.6. Greater discrepancies can be observed in t_R for P2. The differ-

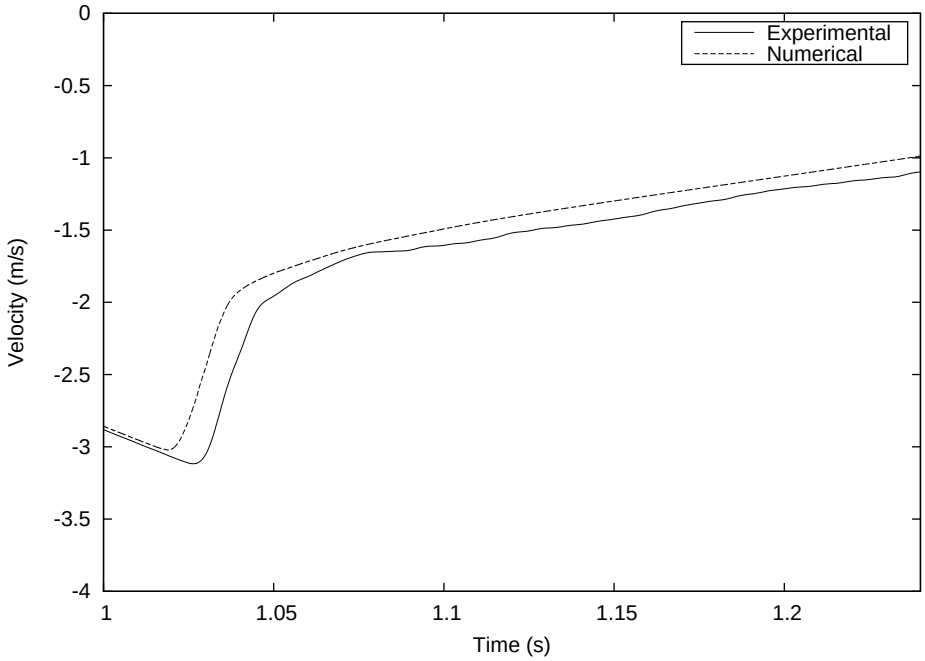

Figure 3.15: Drop velocity of tilted wedge (Case B)

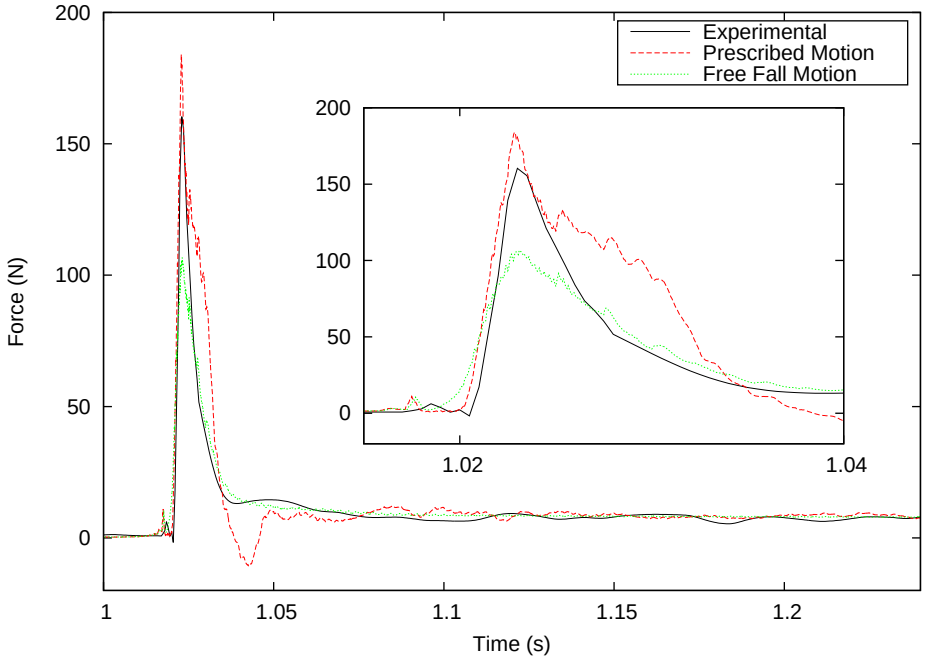

Figure 3.16: Local forces based on free fall motion (Case B)

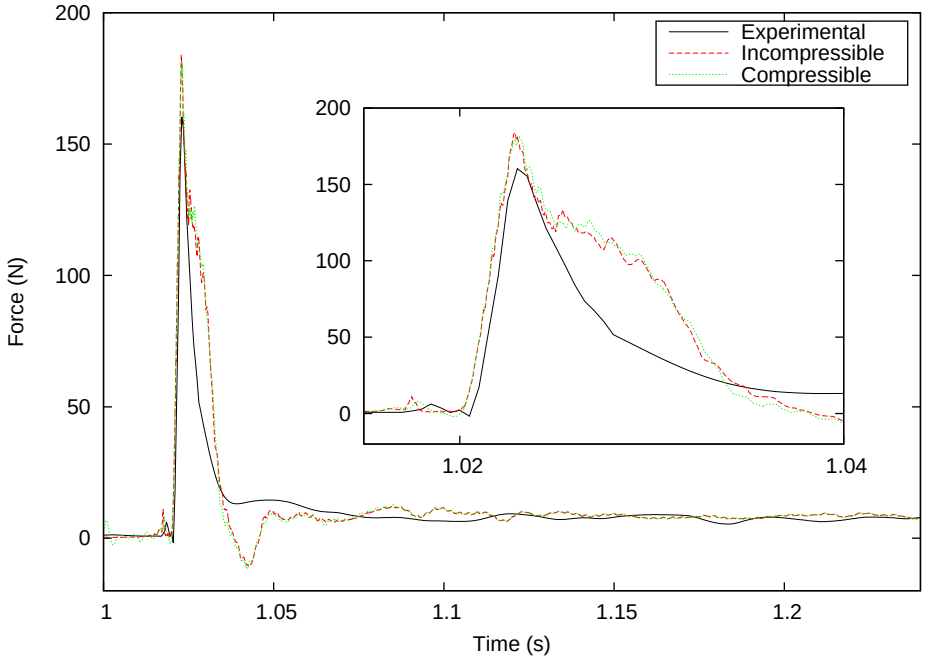

Figure 3.17: Local forces based on compressible and incompressible solvers (Case B)

ence might be due to the uncertainty in the experimental data. Further investigation is needed. The delay times t_D were over-predicted. The time difference between the peak pressures at two pressure sensor locations, ΔT, was also over-predicted.

3.3 Case C: Two-dimensional Ship Section (H_d = 170 mm)

The geometry of the ship section and the computational domain for the ship section are shown in Fig. 3.18. Locations of three local force sensors and three local pressure sensors are also given in Fig. 3.18.

Sensitivity studies on the domain size were conducted by using various widths (W = 3 m, 4 m and 6 m) and depths (D = 4 m, 6 m, and 9 m), which are demon-

Table 3.6: Summary of results (Case B)

		$P_0(kPa)$ or $F_0(N)$	$t_R(s)$	$t_D(s)$	$m_0(kPas$ or $Ns)$	ΔT
	CIP	72.13	0.0007	0.0094	0.36	0.0025
P1	Exp.	70.09	0.0010	0.0051	0.24	0.0017
	Error	3%	33%	83%	51%	44%
	CIP	105.52	0.0012	0.0067	0.42	
P2	Exp.	62.65	0.0002	0.0059	0.19	
	Error	68%	650%	14%	120%	
	CIP	190.35	0.0025	0.0127	1.44	
F	Exp.	160.37	0.0020	0.0070	0.75	
	Error	19%	25%	81%	92%	

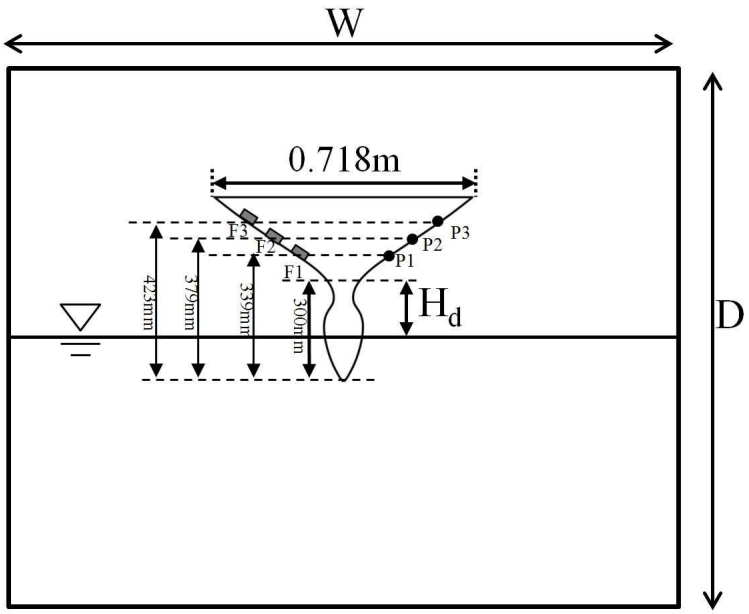

Figure 3.18: Computational domain for ship sections

strated in Figs. 3.19 and 3.20, respectively. It was found that the effect of the size of the domain depth on the solution was very minimal. However, the domain width had relatively greater effect on the solution. The width and the depth of the computational domain were then set as $W = 4$ m and $D = 4$ m, respectively, for the following simulations.

In the sensitivity study on the grid size, non-uniform grids with concentration in the middle of the domain were used. A summary of grids is given in Table 3.7. The number of grids varies from $113,000$ to $1,739,000$. Fig. 3.21 presents the predicted local forces at F1 in terms of various grid sizes. It was found the solutions were sensitive to the grid size. Based on the predicted peak pressures and rise times at three sensor locations, P1, P2 and P3, using the three sets of grids, the calculated GCI's are presented in Table 3.8. The GCI values indicate that the solutions converged as

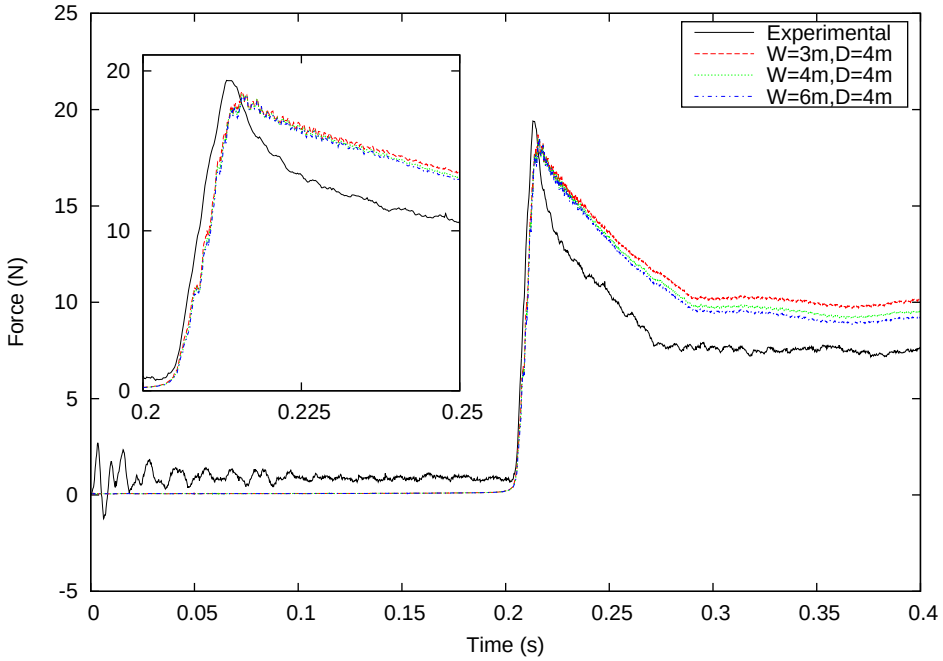

Figure 3.19: Local forces at F1 in convergence study on domain width (Case C)

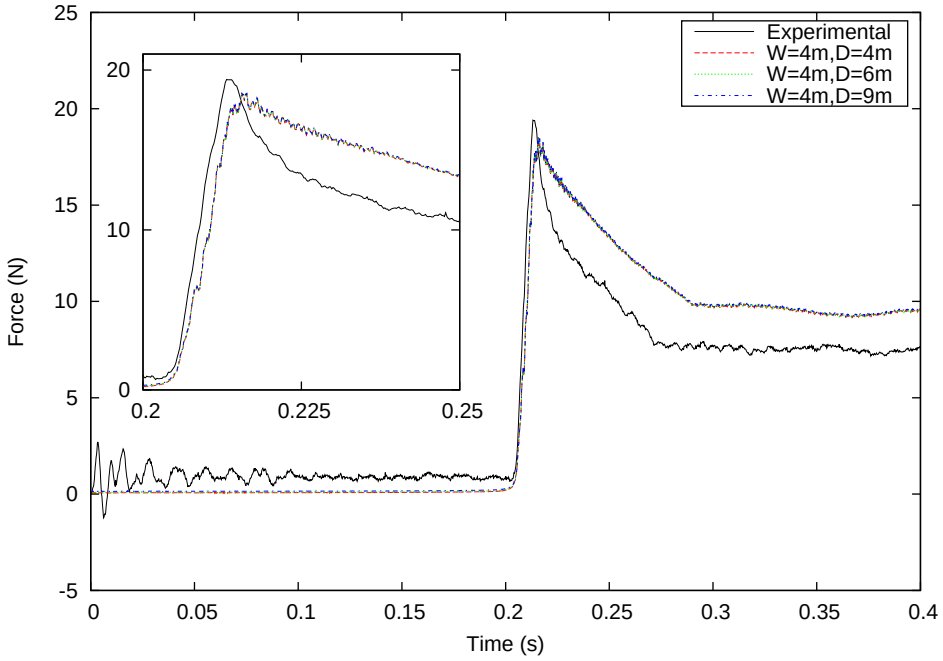

Figure 3.20: Local forces at F1 in convergence study on domain height (Case C)

the number of grids was increased.

Table 3.7: Summary of grids in convergence studies (Cases C and D)

	Δx_{min} (m)	N_x	N_z	N_{total}
Grid 1	0.008	337	337	113,569
Grid 2	0.004	595	595	354,025
Grid 3	0.002	1,319	1,319	1,739,761

Sensitivity studies on time steps were also conducted. Three time steps 0.0002 s, 0.0001 s, and 0.00005 s were studied. Fig. 3.22 presents the predicted local forces at F1 in terms of various time steps. It can be seen that the solutions were sensitive to the time steps. The time step 0.0001 s was used for the following simulations.

Table 3.8: GCI's for Cases C and D

Case	P_0 at P1	P_0 at P2	P_0 at P3	t_R at P1	t_R at P2	t_R at P3
C	9.8%	4.5%	1.6%	0.4%	28.9%	0.0%
D	34.2%	1.9%	0.2%	123.7%	33.4%	0.0%

Note that the sensitivity studies on the domain size, the grid size and the time step were based on the incompressible solver with the THINC/WLIC scheme for interface capturing and the prescribed drop velocities.

Figure 3.23 presents the predicted forces using three interface capturing schemes. The peak values of the predicted forces based on THINC/WLIC and THINC agree

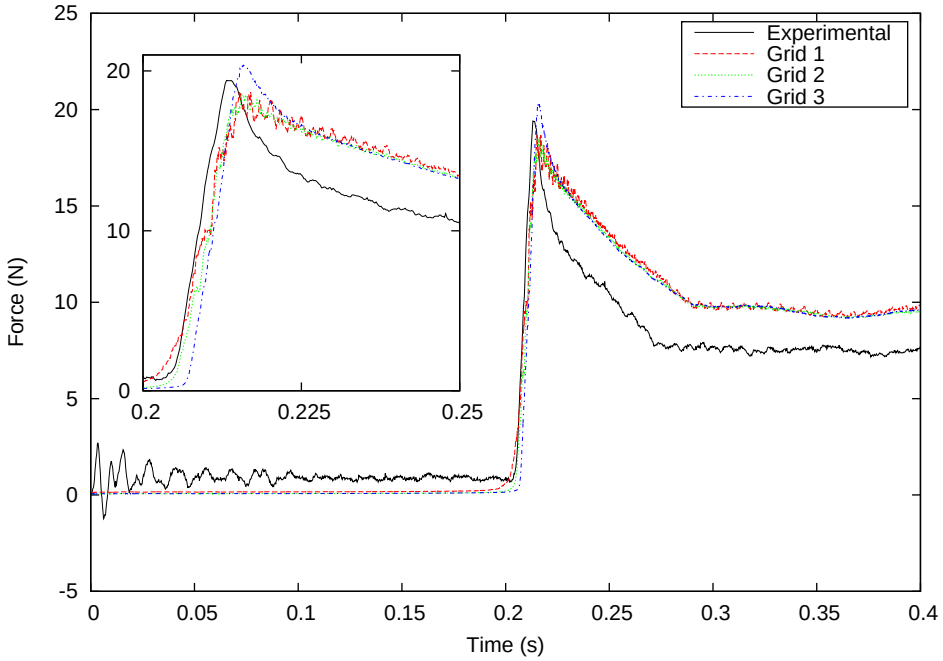

Figure 3.21: Local forces at F1 in convergence study on grid size (Case C)

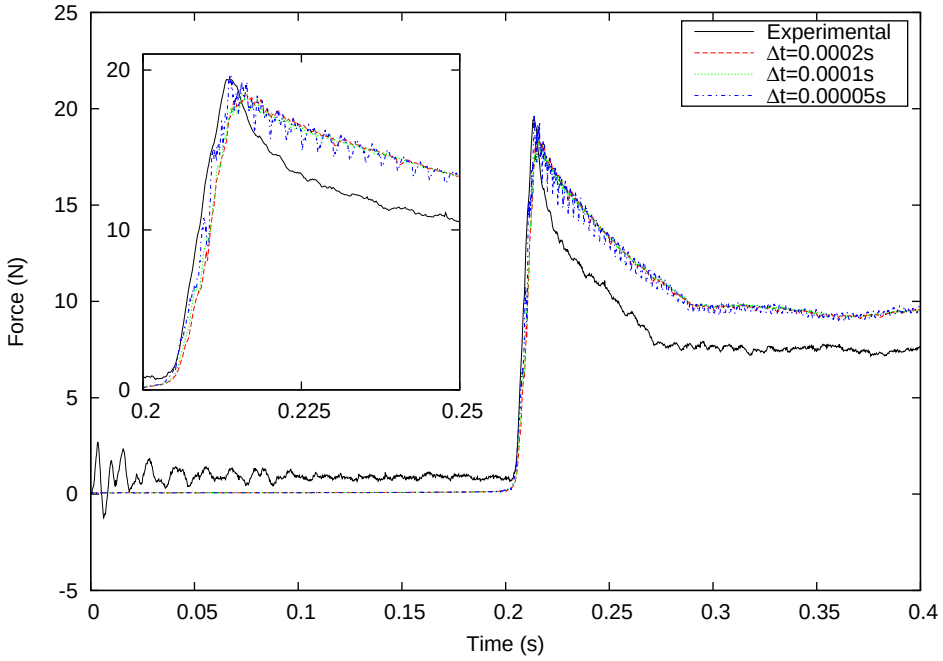

Figure 3.22: Local forces at F1 in convergence study on time step (Case C)

well with the experimental data. The forces were over-predicted after the peak values by the three schemes.

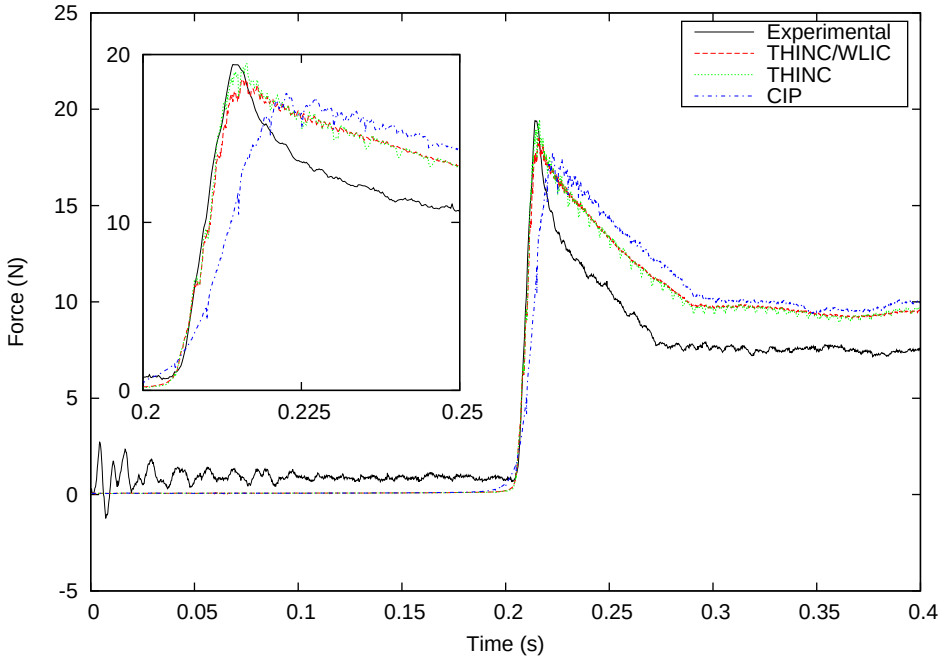

Figure 3.23: Local forces at F1 using three schemes for interface capturing (Case C)

The free fall simulation for the ship section was carried out using the THINC/WLIC scheme and the incompressible solver. The simulation started at $t = 0.0$ s, the same time as that in the model test. The predicted drop velocities are in a good agreement with the experimental data as shown in Fig. 3.24. The predicted peak pressure at the location P1 is presented, as an example, in Fig. 3.25, which agrees well with the experimental results. The delay time was however over-predicted. Similarly, the motion solver led to lower pressures after the impact, but a better agreement with the experimental data.

The predicted local forces with the compressible solver are compared with those

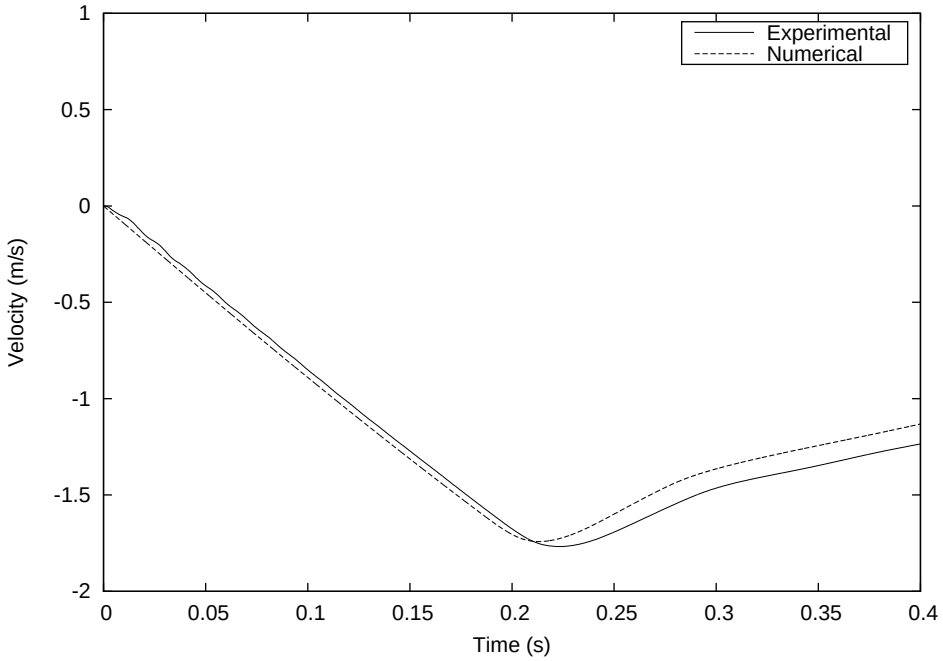

Figure 3.24: Drop velocity of ship section (Case C)

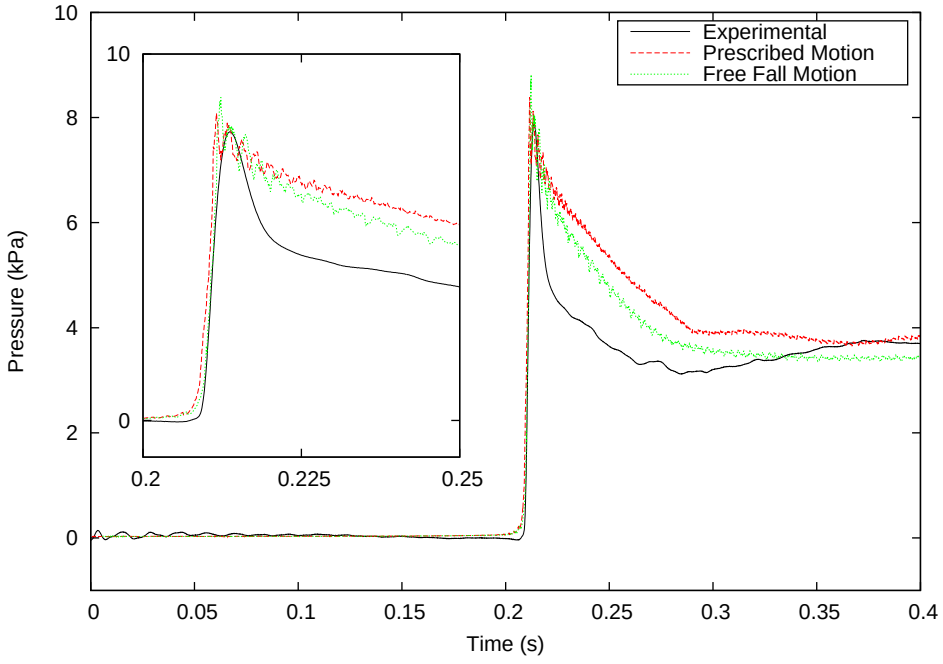

Figure 3.25: Pressures at P1 based on free fall motion (Case C)

based on the incompressible solver in Fig. 3.26. Only slight differences can be observed in the predicted forces. Note that the THINC/WLIC scheme and the prescribed motion were employed in the simulation.

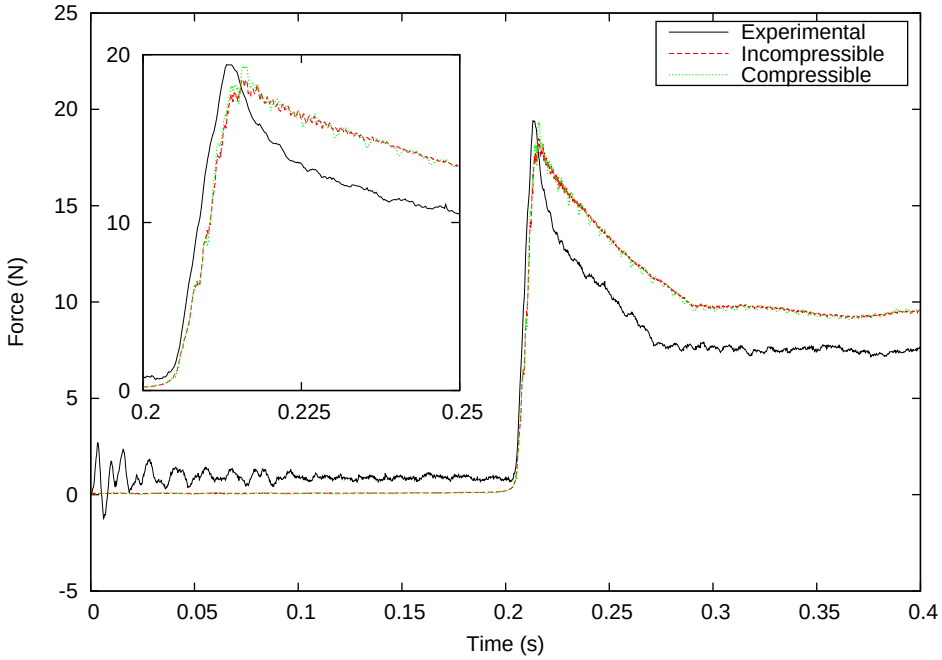

Figure 3.26: Local forces at F1 based on compressible and incompressible solvers (Case C)

The results of the predicted peak forces and pressures, rise time and delay time are summarized in Table 3.9 and compared with the experimental data. Overall, the delay time was over-predicted, which led to the over-predicted momentum. The peak pressures/forces, the rise time and the time differences in peak pressures at three locations ($\Delta T = T2 - T1$ and $\Delta T = T3 - T2$) were better predicted.

The snap shots of free surfaces at three time instants, $t = 0.18$ s, 0.24 s and 0.30 s, are presented and compared with experimental data in Fig. 3.27. Due to the

Table 3.9: Summary of results (Case C)

		P_0 (kPa) or F_0 (N)	$t_R(s)$	$t_D(s)$	m_0 $(kPas)$ or (Ns)
	Num.	10.08	0.0028	0.0847	0.44
P1	Exp.	7.88	0.0056	0.0579	0.25
	Error	28%	50%	46%	76%
	Num.	8.45	0.0039	0.0838	0.37
P2	Exp.	6.16	0.0068	0.0396	0.14
	Error	37%	43%	112%	160%
	Num.	6.57	0.0073	0.0847	0.30
P3	Exp.	4.97	0.0094	0.0791	0.22
	Error	32%	22%	7%	37%
	Num.	20.36	0.0094	0.1412	1.53
F1	Exp.	19.41	0.0092	0.0850	0.91
	Error	5%	3%	66%	68%
	Num.	18.40	0.0124	0.1092	1.12
F2	Exp.	16.30	0.0124	0.0782	0.74
	Error	13%	0%	40%	52%
	Num.	15.12	0.0148	0.0892	0.79
F3	Exp.	12.89	0.0136	0.0610	0.48
	Error	17%	9%	46%	64%
$\Delta T =$	Num.	0.0123			
$T_2 - T_1$	Exp.	0.0123			
	Error	0%			
$\Delta T =$	Num.	0.0164			
$T_3 - T_2$	Exp.	0.0164			
	Error	0%			

narrow section, some air could be trapped as the impact happens so quickly that the air fails to escape from the splashed zone. The trapped air pockets can be clearly observed in Fig. 3.27 (b) and (c), which were well predicted. It should be pointed out that in Fig. 3.27(c) (left), the water and bubbles above the ship section were observed in the experiments due to the gap between the ship section model and the tank wall. Splashed water out of the gap can also be observed in 3.27(b) (left). This might introduce some 3-D effect and contribute to the discrepancies between 2-D predictions and the experimental results.

3.4 Case D: Two-dimensional Ship Section (H_d = 300 mm)

Validation studies were further carried out for the ship section with a greater drop height ($H_d = 0.3$ m). The numerical set-up and convergence studies were the same as those in Case C. The domain sizes were set as $W = 4$ m and $D = 4$ m after the sensitivity studies on the domain size, which are demonstrated in Figs. 3.28 and 3.28.

The non-uniform grids presented in Table 3.7 were used in the sensitivity study on grid size. The solutions were sensitive to the grid sizes. Based on the predicted peak pressures and rise times using the three sets of grids, the GCI values for Case D are given in Table 3.8.

Sensitivity studies on the time step were also conducted using three time steps: 0.0001 s, 0.00005 s and 0.000025 s. The solutions were also sensitive to the time steps. Compared to Case C, a smaller time step was necessary due to the greater

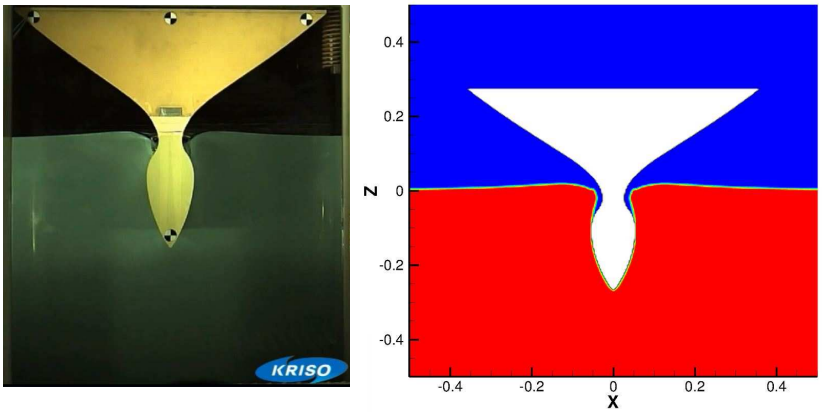

(a) t=0.18 s

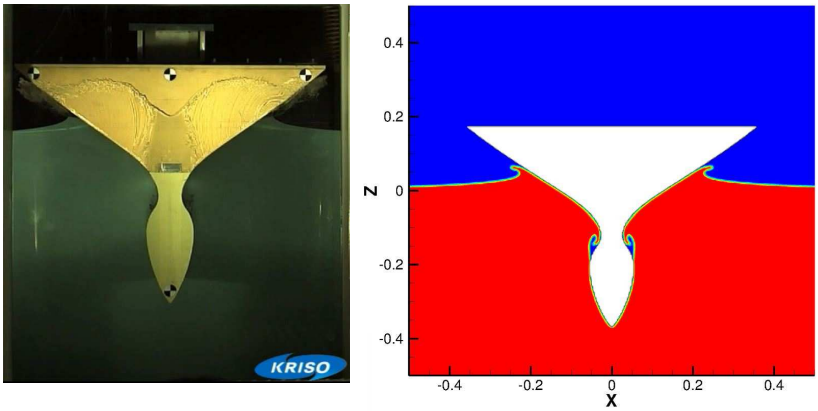

(b) t=0.24 s

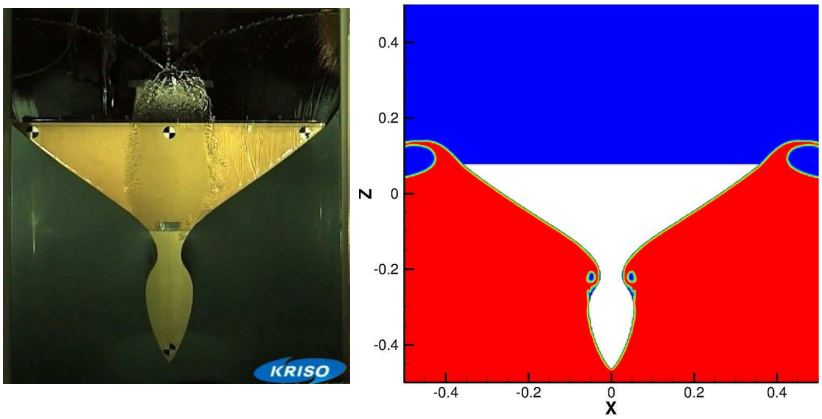

(c) t=0.30 s

Figure 3.27: Snap shots of water surface (Case C)

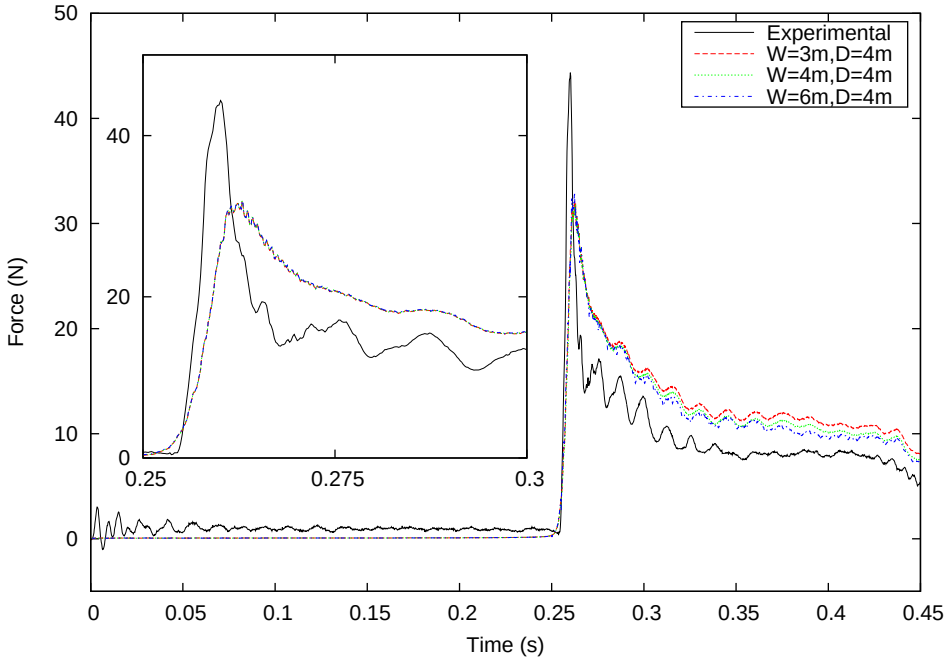

Figure 3.28: Local forces at F1 in convergence study on domain width (Case D)

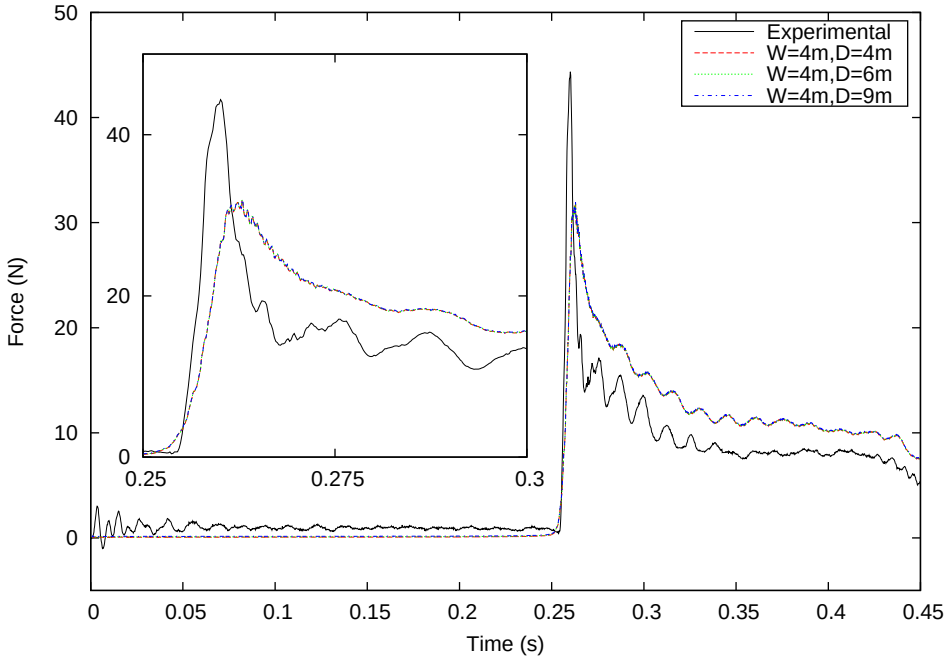

Figure 3.29: Local forces at F1 in convergence study on domain height (Case D)

drop height. The time step of 0.00005s was used in the following simulations.

Figure 3.30 presents results based on three schemes for interface capturing. Similarly, the THINC and the THINC/WLIC schemes gave better predictions of peak pressures/forces and rise times. The CIP method under-estimated the peak force and over-estimated the rise time. All three schemes over-estimated the delay time.

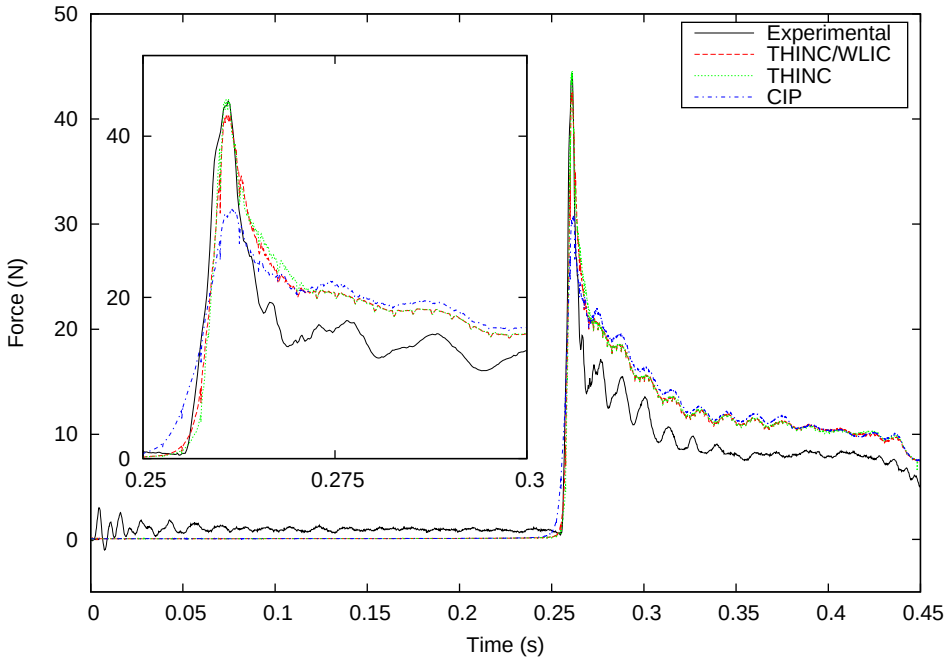

Figure 3.30: Local forces using three schemes for interface capturing (Case D)

The free fall simulation was carried out using the THINC/WLIC scheme for interface capturing and the incompressible solver. The simulation started at $t = 0.0$ s. The predicted velocities are in a good agreement with the experimental results as shown in Fig. 3.31. The predicted local pressure at P1 is presented in Fig. 3.32. The peak pressures were well predicted with the free fall solver.

Fig. 3.33 presents the predicted local forces at F1 based on the compressible

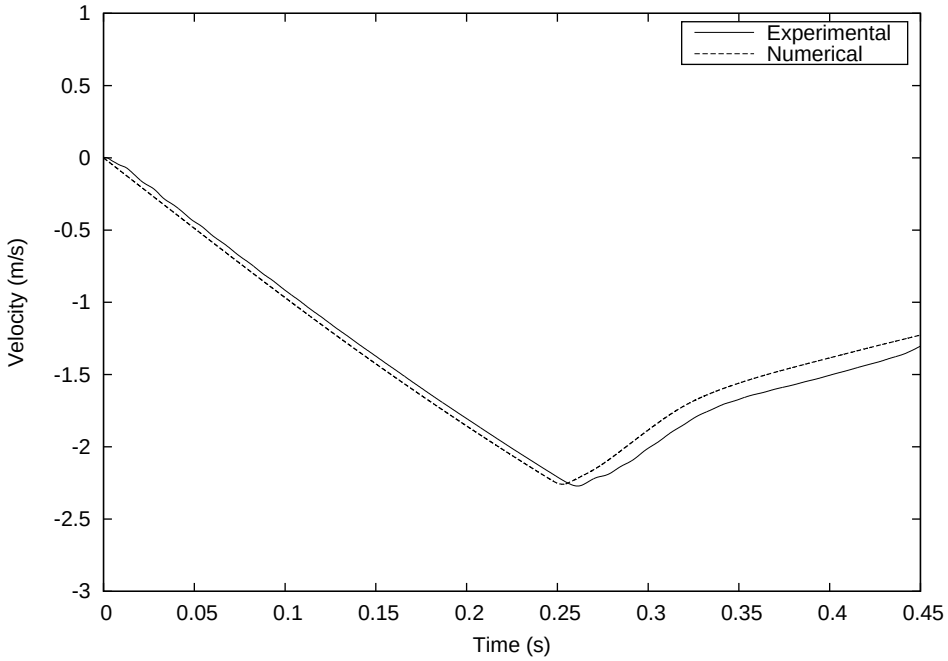

Figure 3.31: Drop velocity of ship section (Case D)

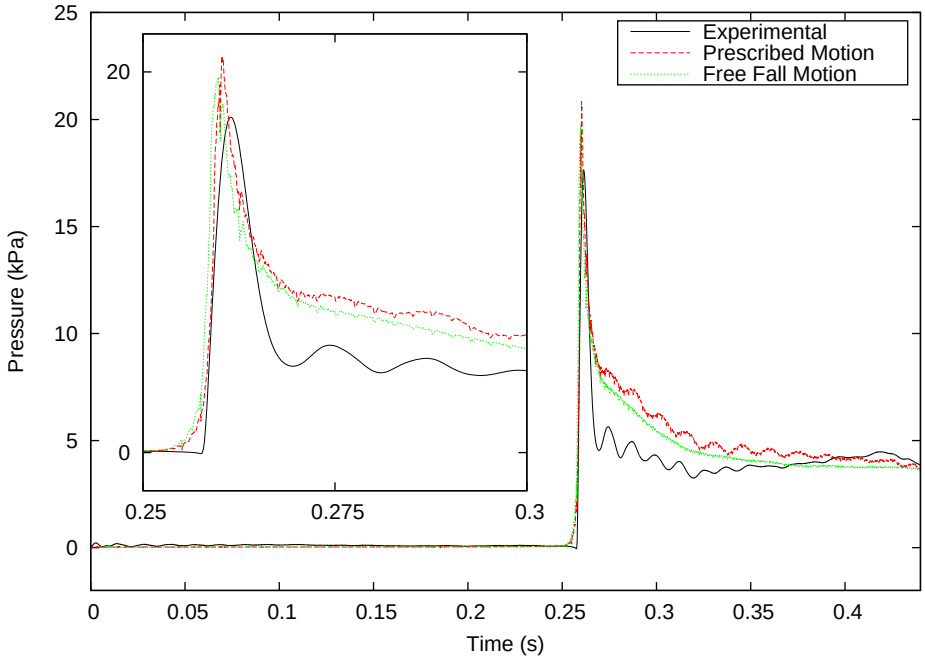

Figure 3.32: Pressures at P1 based on free fall motion (Case D)

and incompressible solvers and using the THINC/WLIC scheme and the prescribed motion were applied. It can be seen that the predicted local forces are generally identical before $t = 0.27$ s. The peak force and the rise time are very similar. The local forces are however different after the first impact. It can be observed that the predicted forces based on the compressible solver are more oscillating than those by the incompressible solver. The oscillations can also be seen in the experimental results, but with smaller amplitudes. The difference is thought to be caused by the trapped air pockets near the force sensor.

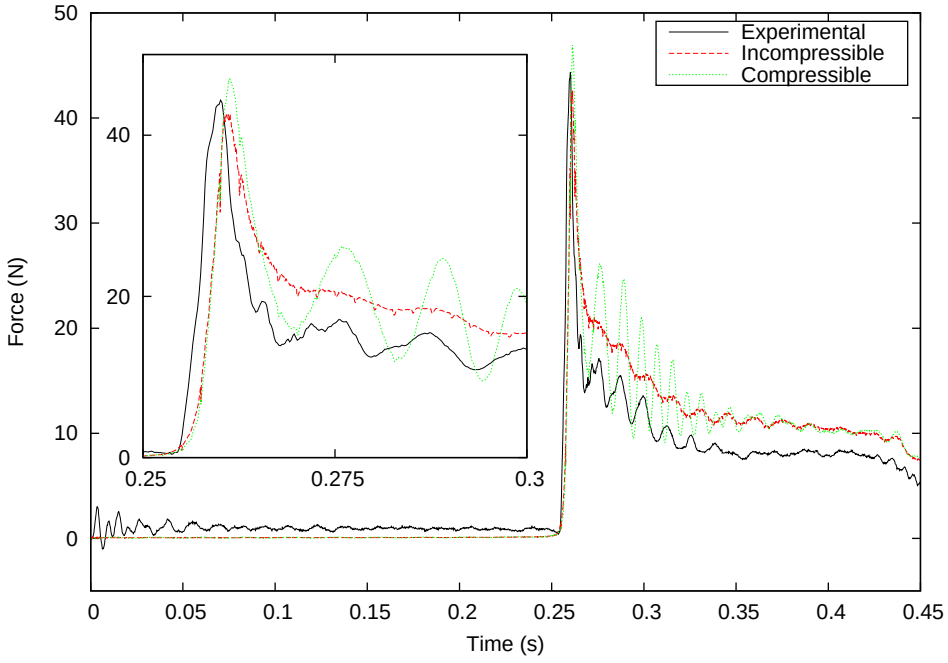

Figure 3.33: Local forces at F1 based on compressible and incompressible solvers (Case D)

The numerical results are summarized in Table 3.10, which were obtained using the incompressible solver with the THINC/WLIC scheme and the prescribed motion.

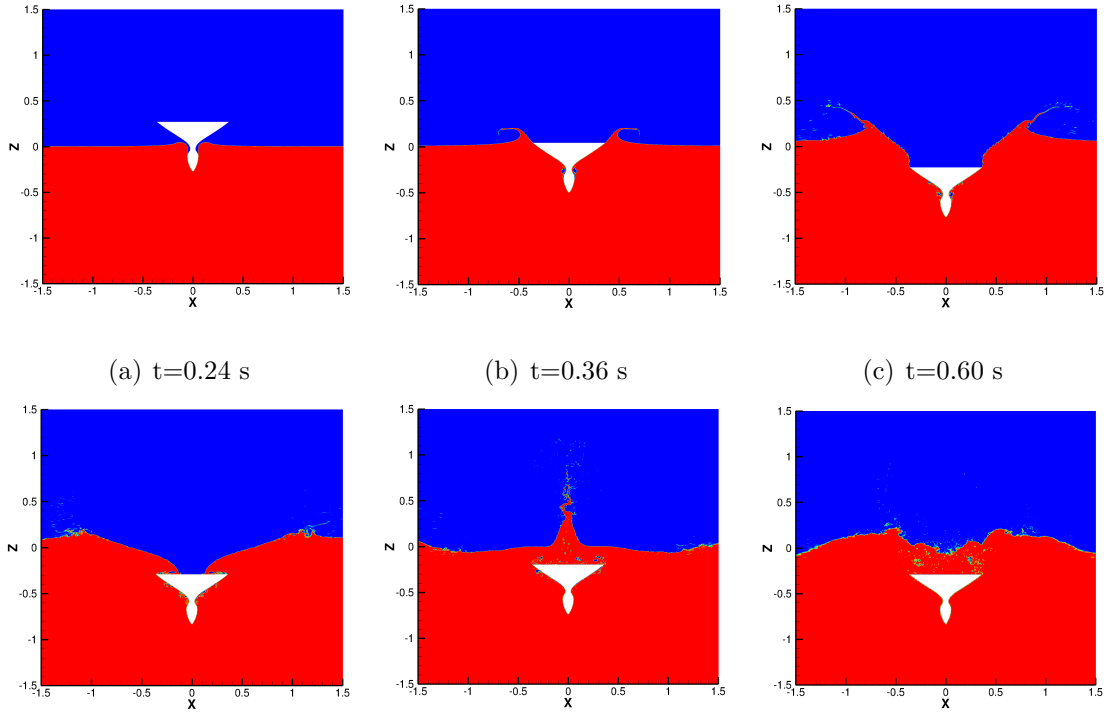

(a) t=0.24 s (b) t=0.36 s (c) t=0.60 s

(d) t=0.80 s (e) t=1.25 s (f) t=1.80 s

Figure 3.34: Snap shots of predicted water surface (Case D)

The agreements with the experimental data are generally good for this case, including the time differences in peak pressures at three sensor locations.

The snap shots of the predicted free surfaces based on the free fall motion at six time instants, $t = 0.24$ s, 0.36 s, 0.60 s, 0.80 s, 1.25 s and 1.75 s, are presented in Fig. 3.34. The process of water entry, first impact, deceleration due to the impact force, water on deck, water splash on deck and the fully submerged stage can be observed. The trapped air pockets were also captured. The bubbles broke in the later phases. A large splash was shown in Fig. 3.34(e). Water was mixed with air bubbles in the later phases of the water entry. Breaking water can also be observed near the free surface.

Table 3.10: Summary of results (Case D)

		P_0 (kPa) or $F_0(N)$	$t_R(s)$	$t_D(s)$	m_0 $(kPas)$ or (Ns)
	Num.	20.85	0.00235	0.0096	0.13
P1	Exp.	17.62	0.0044	0.0078	0.11
	Error	18%	47%	24%	16%
	Num.	12.37	0.0024	0.0504	0.33
P2	Exp.	7.27	0.0058	0.0450	0.18
	Error	70%	59%	12%	76%
	Num.	7.68	0.01368	0.0701	0.32
P3	Exp.	5.47	0.0128	0.0730	0.23
	Error	40%	7%	4%	37%
	Num.	20.36	0.0049	0.0167	0.46
F1	Exp.	44.35	0.0052	0.0072	0.27
	Error	54%	6%	132%	67%
	Num.	22.88	0.0098	0.0988	1.24
F2	Exp.	17.87	0.0075	0.0792	0.77
	Error	28%	31%	25%	60%
	Num.	18.01	0.0188	0.08775	0.96
F3	Exp.	15.19	0.0140	0.0676	0.62
	Error	19%	34%	30%	55%
$\Delta T=$	Num.	0.00705			
$T_2 - T_1$	Exp.	0.0062			
	Error	14%			
$\Delta T=$	Num.	0.0182			
$T_3 - T_2$	Exp.	0.0169			
	Error	8%			

Chapter 4

Water Entry of Three-dimensional Bodies in Calm Water

The present method was further extended to three-dimensional simulations. This chapter presents numerical solutions of the water entry of a 3-D wedge, a free falling Wigley hull (with various drop heights H_d) and a free falling inclined cylinder. The numerical results were compared with experimental data and those by other numerical methods. Table 4.1 summarizes the 3-D simulation cases.

In the computations, block computational domains were employed. As shown in Fig. 4.1, D is the water depth, W is the width of the computational domain and S is the span-wise length of the computational domain. The solid body, for example, a 3-D wedge section, is located in the middle of the domain. Non-uniform Cartesian grids were used with finer grids distributed near the path of the body. Fig. 4.2 presents a cross section of the non-uniform grids. The time step was kept constant in the computations. The THINC/WLIC scheme and the incompressible solver were used

Table 4.1: Summary of 3-D cases

Case ID	Body shape	Drop height H_d	Entry velocity	Inclined angle
E	Wedge	2.0 m	6.15 m/s	0°
F1	Wigley hull	0.5 m	3.13 m/s	0°
F2	Wigley hull	0.4 m	2.80 m/s	0°
F3	Wigley hull	0.3 m	2.43 m/s	0°
F4	Wigley hull	0.2 m	1.98 m/s	0°
G1	Circular cylinder	2.0 m	6.17 m/s	20.7°
G2	Circular cylinder	2.0 m	6.12 m/s	48.6°
G3	Circular cylinder	2.0 m	6.11 m/s	55.6°

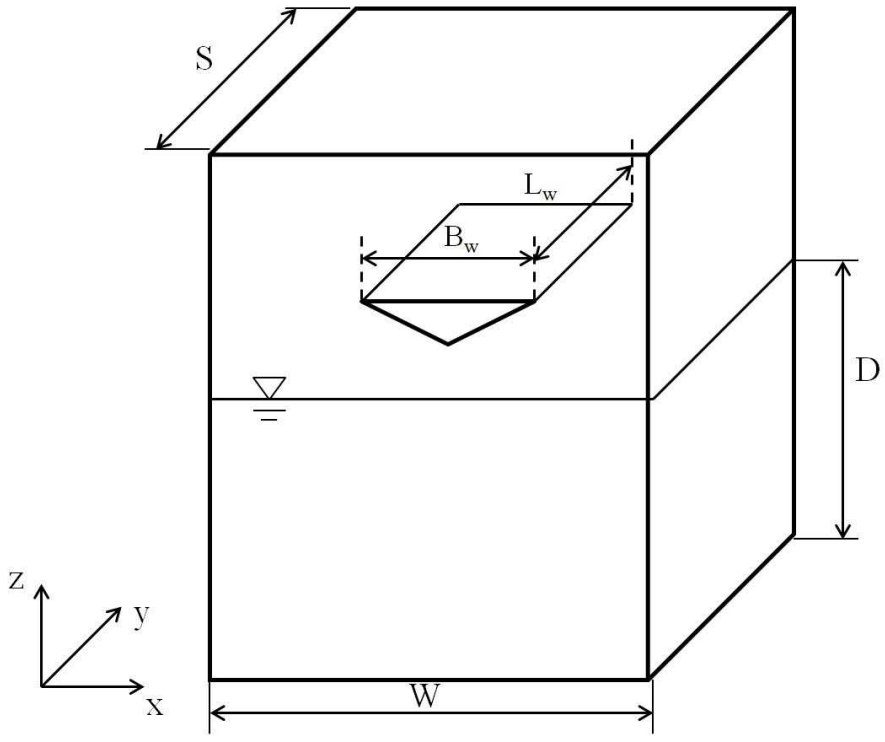

Figure 4.1: Computational domain for 3-D water entry

in the following computations.

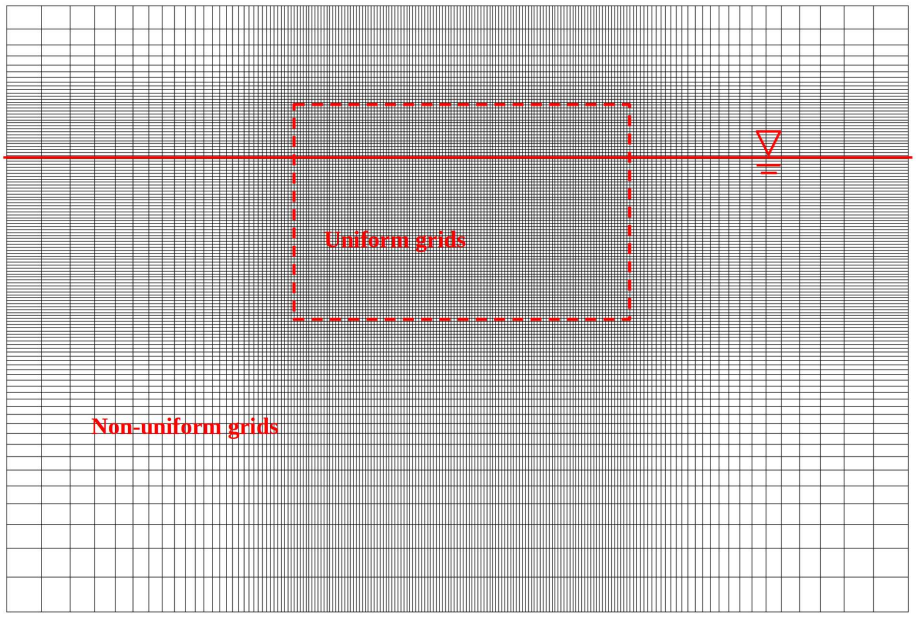

Figure 4.2: A cross section view of the non-uniform grids

4.1 Case E: Three-dimensional Wedge

In the experiments on the water entry of a 3-D wedge by Zhao et al. [111], the width of the wedge was $B_w = 0.5$ m, length $L_w = 1.0$ m and its deadrise angle was 30°. The length of the measuring segment was 0.2 m. The time history of the drop velocity in the tests by Zhao et al. [111] was taken as prescribed one in the simulations. The initial time is denoted as the moment when the wedge touched the water surface.

The sensitivity of the numerical solutions to the size of the computational domain was investigated. The simulations were performed using various domain widths W, domain lengths, S, and water depths D. In the sensitivity study of the domain width,

$W = 1.6$ m, 2.4 m and 3.0 m, were used while $D = 1.5$ m and $S = 1.5$ m. Three water depths, $D = 0.5$ m, 1.0 m and 1.5 m, were examined with fixed domain width and length, $W = 2.4$ m and $S = 1.5$ m. The numerical solutions are presented in Figs. 4.3 and 4.4, respectively. It can be seen that the results converged as the domain sizes increased. In the following computations, $W = 2.4$ m and $D = 1.0$ m were used.

The sensitivity study on the domain length, S was also conducted with $S = 2.2$ m, 2.4 m and 2.6 m, and the results are presented in Fig. 4.5. It is shown that the numerical results were insensitive to the domain length and $S = 2.2$ m were therefore chosen for the following computations.

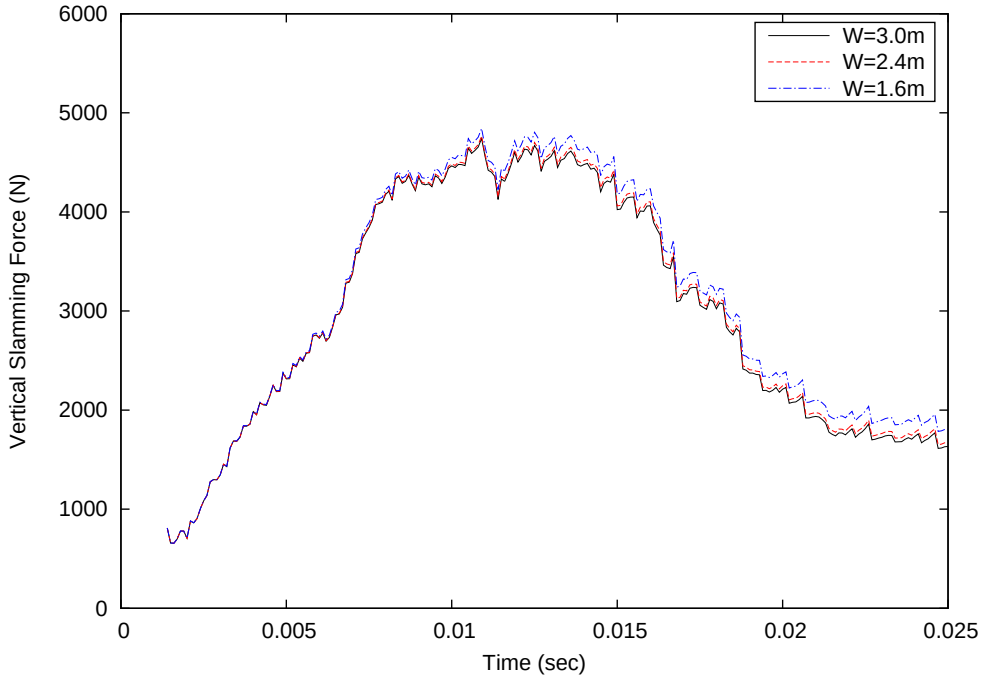

Figure 4.3: Sensitivity of slamming force to domain width (Case E)

Effects of the grid resolution and the time step on the solutions were also investigated. In terms of studies on the grid size, the minimum grid spacings, $\Delta x = 0.02$ m,

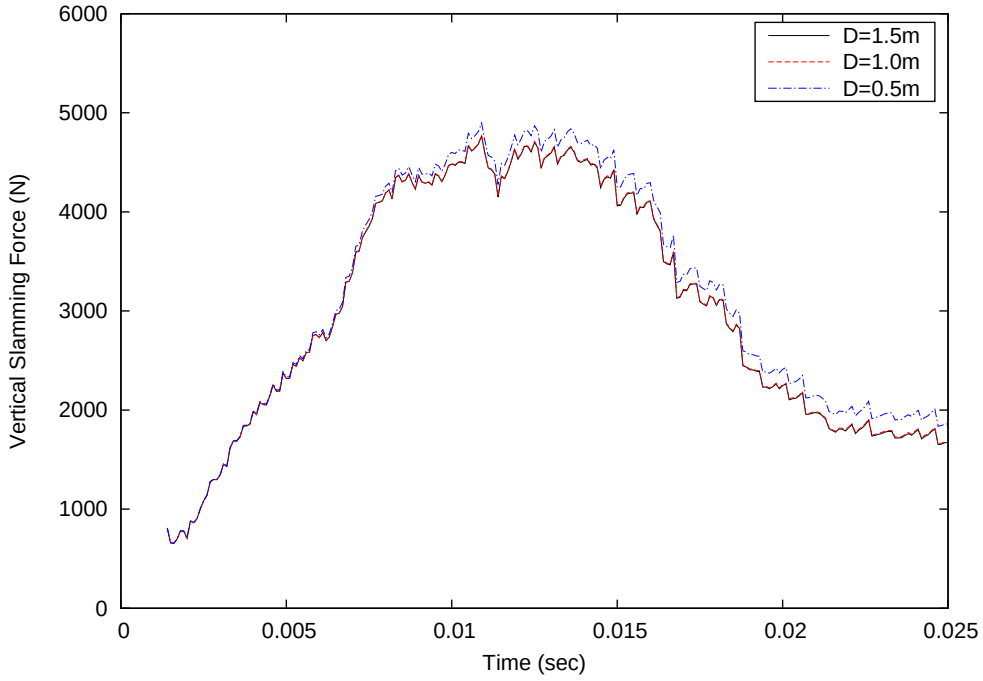

Figure 4.4: Sensitivity of slamming force to water depth (Case E)

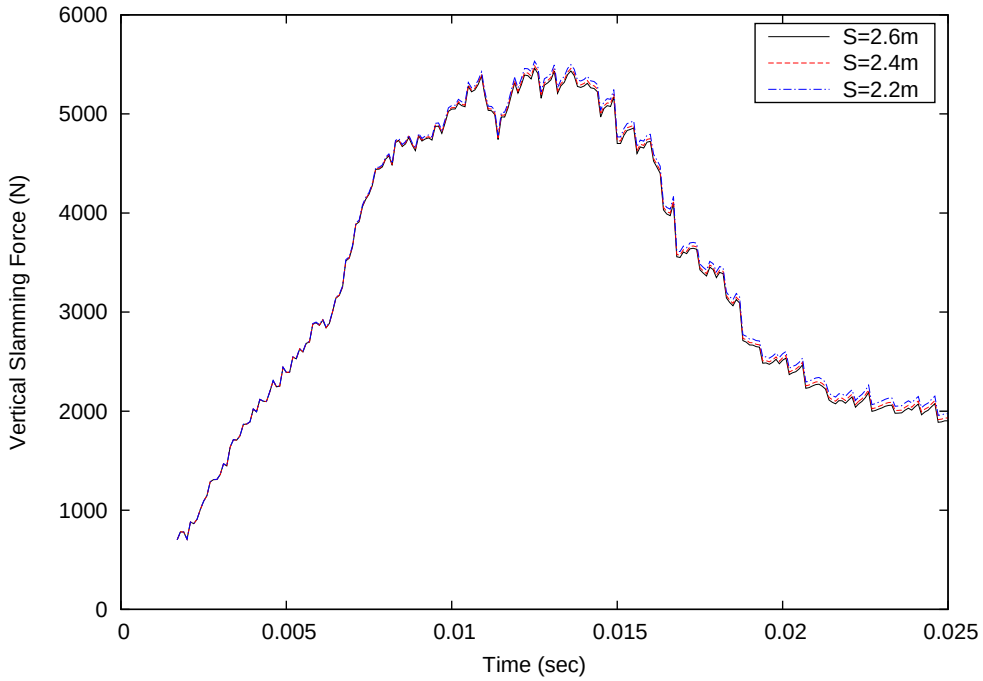

Figure 4.5: Sensitivity of slamming force to domain length (Case E)

0.01 m and 0.005 m, were employed and the time step was set as $\Delta t = 0.0001$ s. The total number of grids varied from $274,000$ to $13,500,000$. Three time steps, 0.0001 s, 0.00005 s and 0.000025 s, were used to examine the effect of the time step on the solutions with the finest grid. Their corresponding Courant numbers were around 0.15, 0.075 and 0.0375, respectively. Note that the wedge length, $L_w = 1.0$ m, was set in all sensitivity studies.

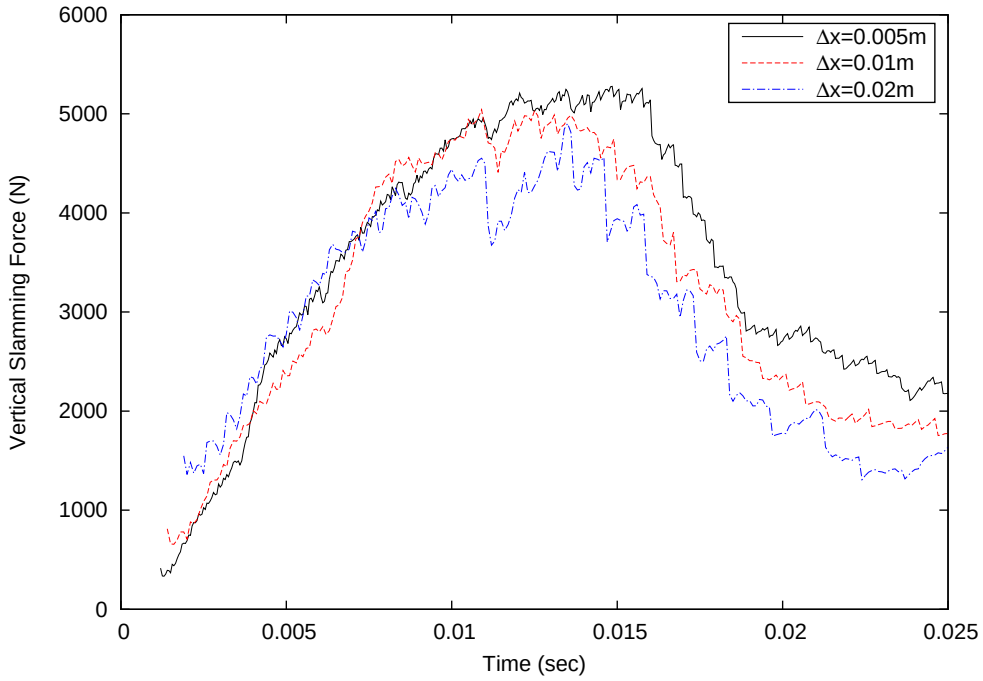

Figure 4.6: Sensitivity of slamming force to grid size (Case E)

The effects of grid size and time step on solutions are shown in Figs. 4.6 and 4.7, respectively. The results are sensitive to the grid size, but relatively insensitive to the time step and the chosen Courant numbers. It should be noted that low Courant numbers are required to better solve the advection equations and therefore the impulsive impact problems by the present method. The Courant numbers of less

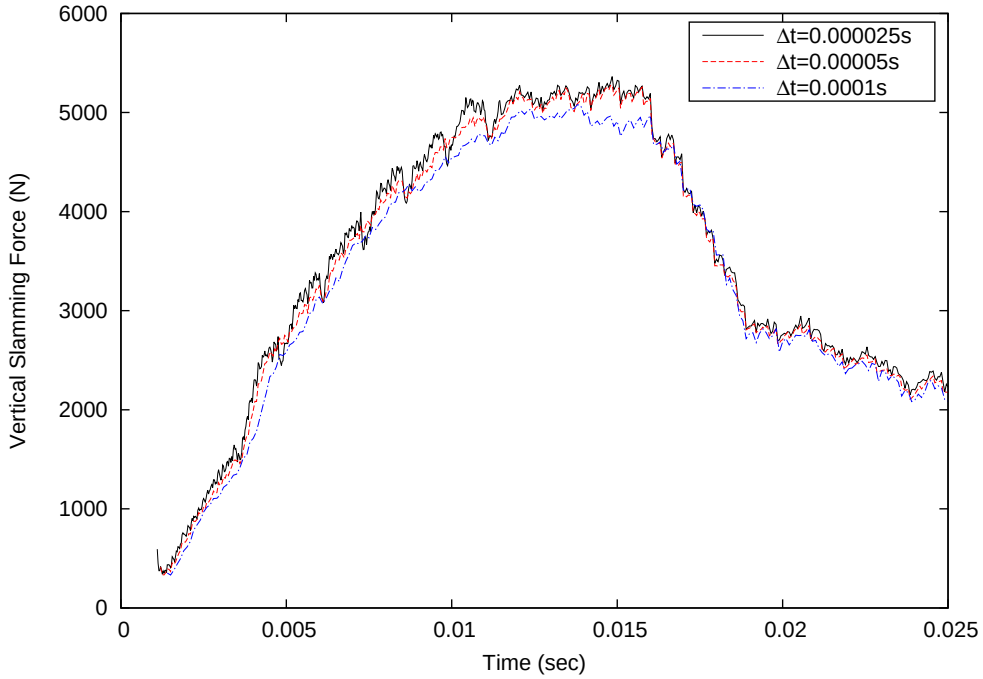

Figure 4.7: Sensitivity of slamming force to time step (Case E)

than 0.2 were thus set in all the following computations.

Based on the predicted maximum slamming forces using three sets of grids, the GCI was evaluated and is given in Table 4.2, along with the variables as defined in Eqs. (2.43) to (2.47). Note that α_1 denotes the predicted maximum slamming force based on the finest grid. The uncertainty in the predicted maximum slamming force due to spatial discretization errors is less than 1%.

The effect of the length of the wedge on the solution was investigated with $L_w = 0.6$ m, 0.8 m, 1.0 m and 1.5 m. Note that while L_w was varied, the length of measurement segment was kept the same as that in experiments (0.2 m). The solutions are presented in Fig. 4.8 in comparison with the two-dimensional results. It is apparent that a larger wedge length leads to a greater slamming force on the measurement segment. This is likely caused by 3-D effects. The two-dimensional solutions, in which L_w is considered

Table 4.2: Calculation of GCI's

Case	α_1	α_2	α_3	k	$q(k)$	α_e^{21}	e_a^{21}	GCI
E	5079 N	5041 N	4901 N	1.88	0	5093 N	0.75%	0.35%
F1	2740 N	2640 N	2368 N	5.05	0.45	2771 N	3.65%	1.40%
F2	2219 N	2139 N	1923 N	5.02	0.45	2244 N	3.61%	1.39%
G1	−0.1261 m	−0.1315 m	−0.155 m	2.26	0.60	−0.1253 m	4.28%	0.77%

infinite and no 3-D effect is involved, predicts larger maximum slammiing force than the three-dimensional results.

The effect of air compressibility on the predicted slamming force was further investigated. The solutions from compressible and incompressible solvers are presented in Fig. 4.9. As expected, no significant difference can be observed for the wedge with a deadrise angle of 30°. Note that the air compressibility has an effect on the slamming force only at low deadrise angles (less than 4°), where air compressed air cushions occur (Yang and Qiu [104]).

The time history of the computed vertical slamming force, using grids with a minimum spacing of 0.005 m and the time step of 0.00005 s, is presented in Fig. 4.10 and compared with experimental results and the numerical solutions based on the potential-flow theory by Zhao et al. [111], the VOF method by Kleefsman et al. [41], and the CIP method by Yang and Qiu [104]. Note that $L_w = 1.0$ m, the same value as that in the experiment by Zhao et al. [111], was used in the simulations. It is clearly observed that 2-D BEM over-predicted the slamming force. However,

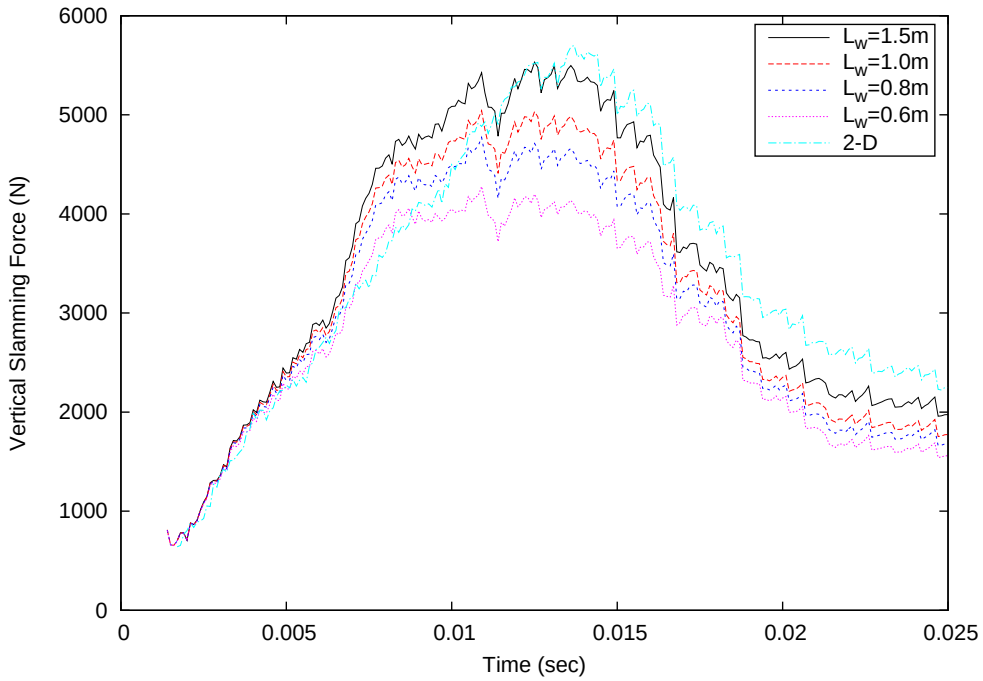

Figure 4.8: Sensitivity of slamming force to section length (Case E)

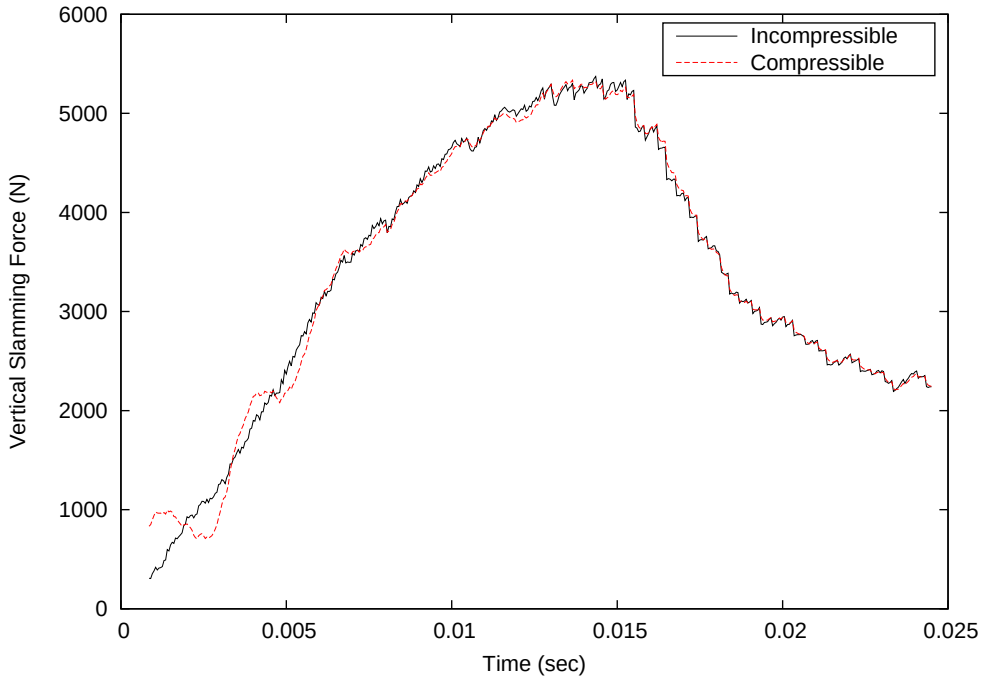

Figure 4.9: Sensitivity of the slamming force on a segment to the compressibility (Case E)

the BEM results with 3-D correction fall in the range of 3-D results by other CFD methods. The present method led to much better agreement with the experimental results. The numerical results are also compared with solutions based on a different interface capturing scheme, in which the governing advection equation for the water phase, Eq. 2.16, was solved by using the CIP method instead of the THINC/WLIC scheme. Discrepancies can be found between solutions based on the CIP method and the THINC/WLIC scheme. The slamming force was under-estimated by the CIP method. The results based on the parallel CIP method have similar trends with those based on the original CIP method by Yang and Qiu [104], but with suppressed oscillation. This may be due to the fact that the solid phase was treated differently in the CIP method by Yang and Qiu [104]. Yang and Qiu [104] used panels and distance functions from points on panels to grid cell surfaces to calculate the density function for solid. The present method used fourth order Gaussian quadrature to calculate the density function.

Local pressure distributions on the bottom of the wedge at three time instances during the water entry were compared with the numerical solutions and experimental data by Zhao et al. [111] in Fig. 4.11. In the figure, $p' = \frac{p-p_0}{\frac{1}{2}\rho V(t)^2}$, where $V(t)$ is the drop velocity at the moment, t, $t = 0$ s corresponds to the moment that the wedge keel touches the water surface, $p_0 = 0$ Pa is the reference pressure, ρ is the density of water, $z' = \frac{z}{\int_0^t V(t)dt}$ and z is the vertical position of a point on the wedge surface measuring from the wedge keel. It can be seen that the local pressures are generally in good agreement with experimental data and are better captured by the present method than those by BEM.

The snap shots for free surfaces at six time instants, $t = 0.0005$ s, 0.005 s, 0.01

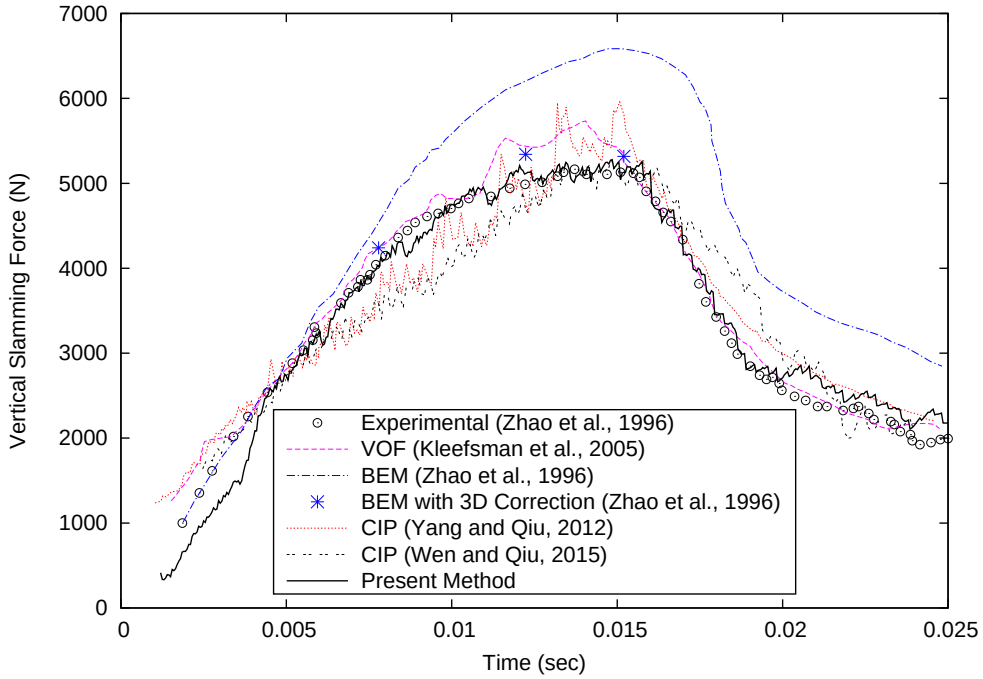

Figure 4.10: Slamming force on 3-D Wedge

s, 0.015 s, 0.02 s and 0.024 s, are presented in Fig. 4.12. Note that the free surface contours were obtained by using the density functions in the computational domain and the isosurface with $\phi_1 = 0.5$. It can be seen that the water sprays were well captured. The predicted pressure distributions on the wedge bottom at these time instances are also presented in the figures.

4.2 Case F: Wigley Hull

The present method with the motion solver was applied to the free fall of a modified Wigley hull entering calm water. The mathematical hull form is given as:

$$\eta = (1-\zeta^2)(1-\xi^2)(1+0.2\xi^2) + \zeta^2(1-\zeta^8)(1-\xi^2)^4 \tag{4.1}$$

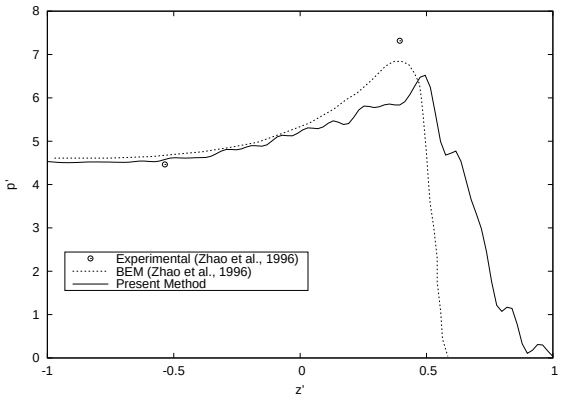

(a) $t = 0.00435$ s

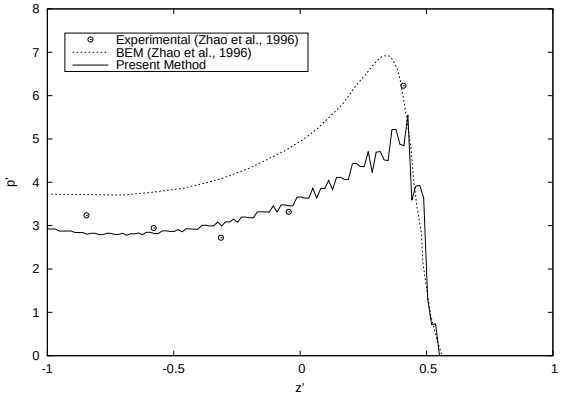

(b) $t = 0.0158$ s

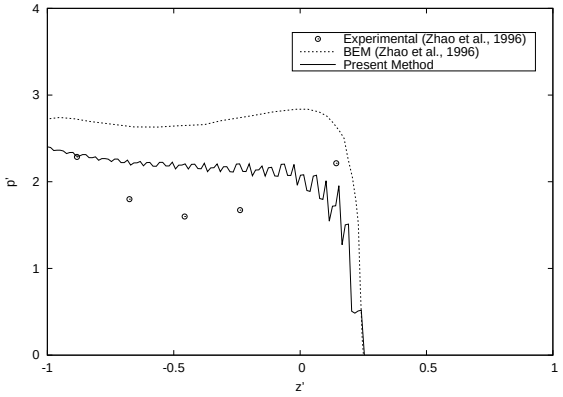

(c) $t = 0.0202$ s

Figure 4.11: Pressure distribution on a wedge section

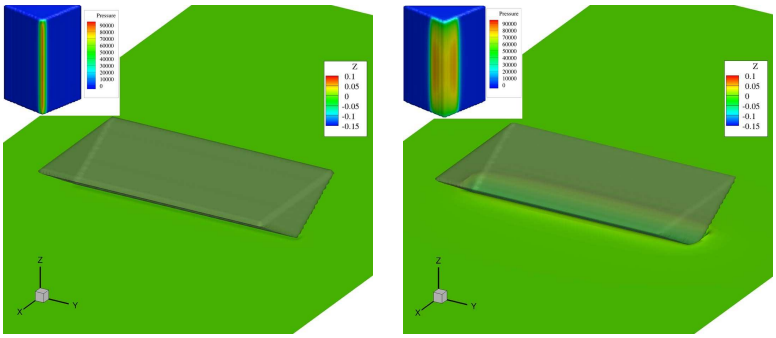

(a) $t = 0.0005$ s (b) $t = 0.005$ s

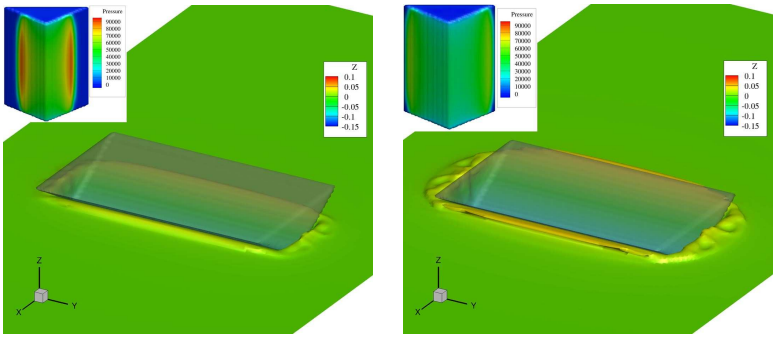

(c) $t = 0.01$ s (d) $t = 0.015$ s

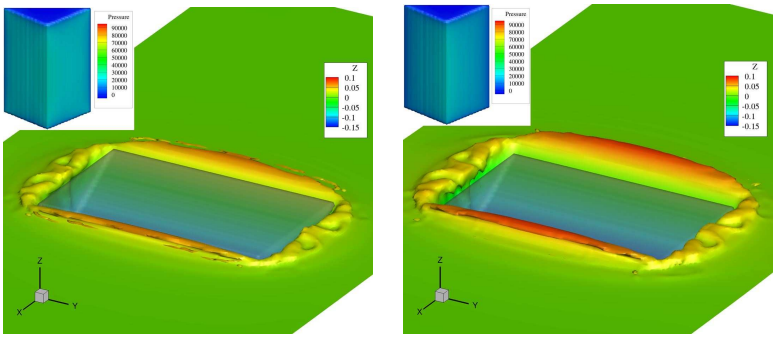

(e) $t = 0.02$ s (f) $t = 0.024$ s

Figure 4.12: Predicted water surfaces and pressure distribution (Case E)

where $\xi = 2x/L_s$, $\eta = 2y/B_s$ (positive to port side), $\zeta = z/D_s$ is the vertical axis positive upwards, $-L_s/2 \leq x \leq L_s/2$, $-B_s/2 \leq y \leq B_s/2$, $-D_s \leq z \leq 0$. The drop tests were carried out by Hong et al. [28]. The principal dimensional of the model were $L_s = 1.25$ m, $B_s = 0.25$ m, $D_s = 0.25$ m. The total mass of the model and the experimental apparatus including sensors was $m = 149.4$ kg. The dimensions of the tank used for the tests by Hong et al. [28] are 5 m long, 3 m wide. The water depth was 1.4 m.

Sensitivity studies on the size of the computational domain were carried out by using the actual tank size and a smaller domain with $W = 2.0$ m, $S = 1.0$ m and $D = 1.0$ m. In the sensitivity studies, the drop height was set as $H_d = 0.5$ m. As shown in Fig. 4.13, the numerical results are not sensitive to the domain size. As a result, $W = 2.0$ m, $S = 1.0$ m and $D = 1.0$ m were used in the following computations.

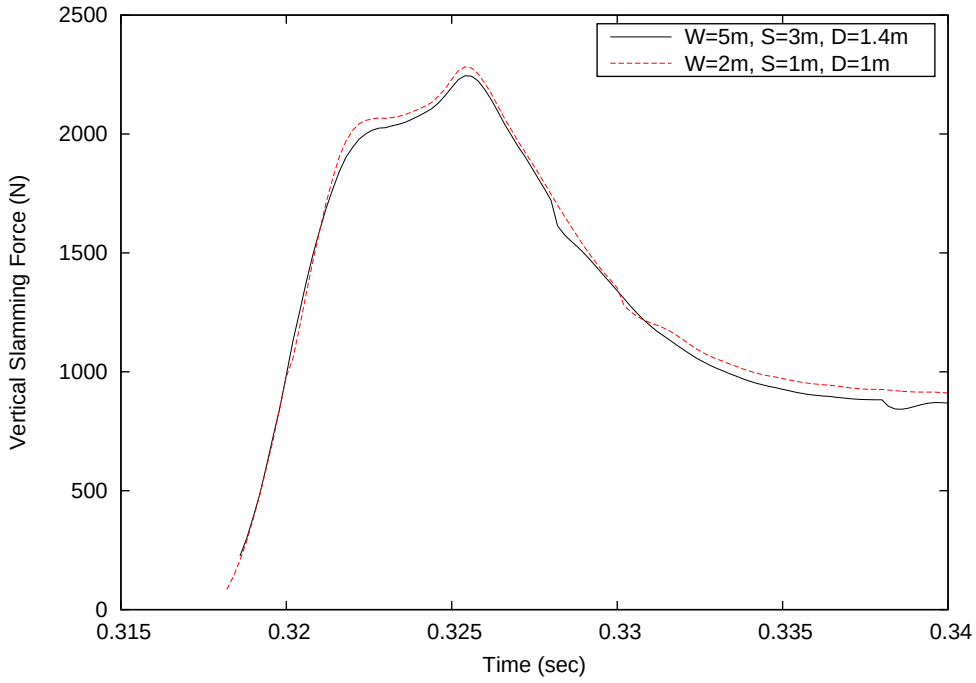

Figure 4.13: Sensitivity of slamming force to domain size (Case F1)

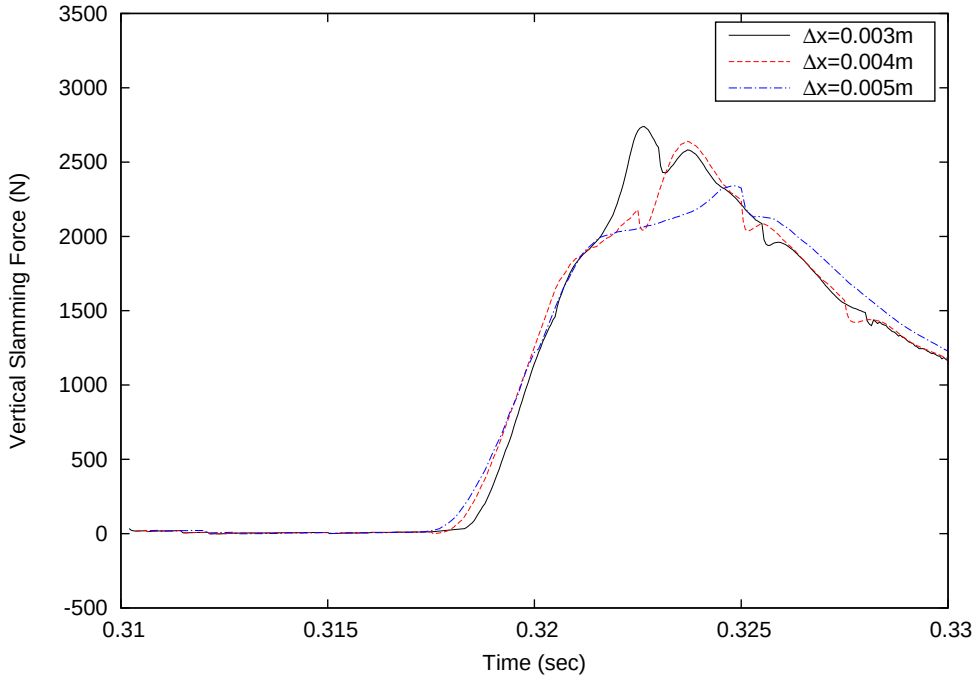

Figure 4.14: Sensitivity of slamming force to grid size (Case F1)

The convergences of the numerical solutions to the grid size and the time step are presented in Figs. 4.14 and 4.15, respectively, with the drop height of $H_d = 0.5$ m. Three sets of grids with minimum grids, $\Delta x = 0.005$ m, 0.004 m and 0.003 m, were employed and the corresponding numbers of grids varied from $10,700,000$ to $42,000,000$. Relatively finer grids than those in the case of the 3-D wedge were used due to the curvature of the Wigley hull surface. It can be observed from Fig. 4.14 that the predicted slamming forces are sensitive to the grid size. The maximum slamming forces based on coarser grids were smaller than those based on finer grids. Based on the predicted maximum slamming forces, the GCI for this case, denoted as Case F1, was evaluated and is presented in Table 4.2.

The same studies were extended to another drop height, $H_d = 0.4$ m. The calculated GCI is given in Table 4.2 (Case F2). The GCIs for both drop heights were less

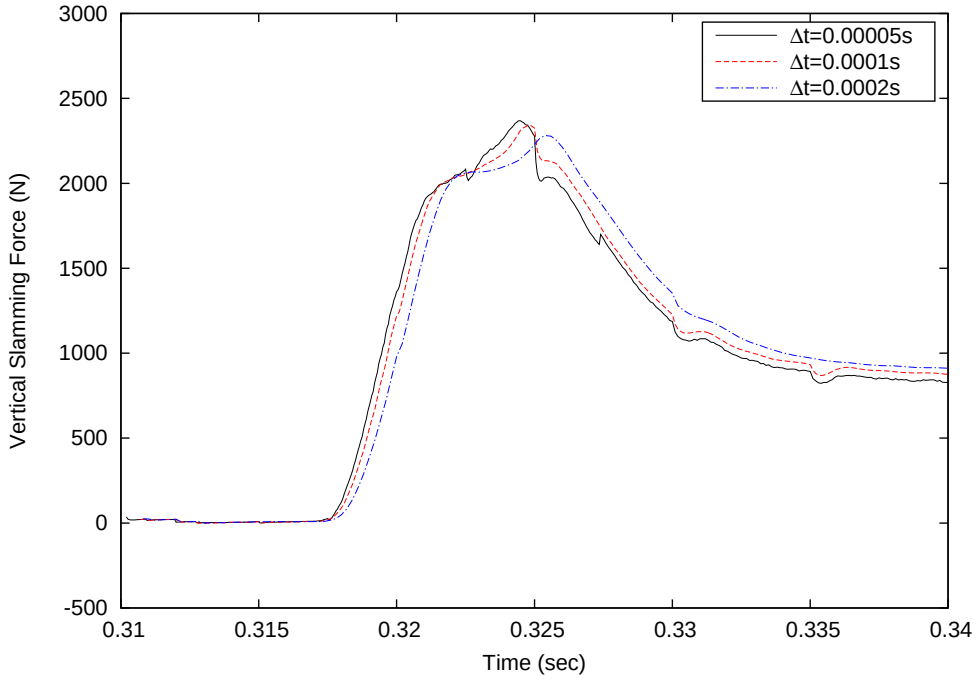

Figure 4.15: Sensitivity of slamming force to time step (Case F1)

than 2%.

In the convergence studies on the time step, three time steps, $\Delta t = 0.0002$ s, 0.0001 s and 0.00005 s were used. It can be observed from Fig. 4.15 that the time step had an insignificant effect on the predicted slamming force.

Four drop heights, $H_d = 0.2$ m, 0.3 m, 0.4 m, 0.5 m, were further studied using $\Delta x = 0.003$ m and $\Delta t = 0.00005$ s. The corresponding simulation conditions are summarized in Table 4.1.

As shown in Fig. 4.16, the predicted maximum vertical slamming forces, F_s, are in good agreement with the experimental results by Hong et al. [28], especially at low drop heights. At greater drop heights, $H_d = 0.4$ m and $H_d = 0.5$ m, the differences are less than 10%. It can be observed that the discrepancies between experimental and numerical results increase as the drop height increases. This is mainly due to the

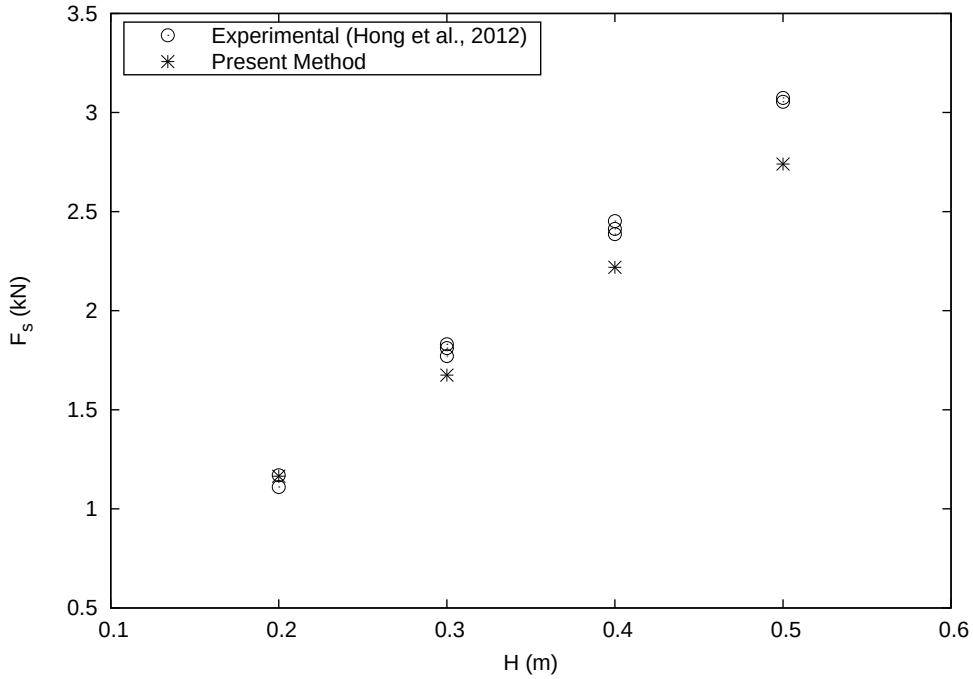

Figure 4.16: Maximum slamming force on Wigley hull

increased numerical dissipation and energy loss in water jets and bubbles.

4.3 Case G: Inclined Cylinder

The numerical method with the motion solver was further validated for the free fall of an inclined cylinder entering calm water. Experiments on the inclined cylinder were carried out by Wei and Hu [87]. The simulations are more challenging since the water entry involves not only the initial impact, but also the formation and collapse of cavities. Table 4.1 presents the properties of the entry conditions. The length and the diameter of the cylinder were 0.2 m and 0.05 m, respectively. The density of the cylinder was 900 kg/m^3. Three different inclined angles, $\theta_0 = 20.7°$, 48.6° and 55.6°, were investigated. In the experiments of Wei and Hu [87], the drop tests were

conducted in a water tank of 1.35 m × 1.35 m × 1.35 m. A high-speed camera was used to track the free surface and the motions of the cylinder. In the present studies, the predicted water surface and motions were compared with the experimental data.

Sensitivity studies on the domain size, the grid size and the time step were performed for Case G1 ($\theta_0 = 20.7°$). The effect of the computational domain size on the solution was first examined using the actual tank size and a smaller domain with $W = 1.0$ m, $S = 0.6$ m and $D = 1.0$ m. The predicted time histories of the velocity components in the x and z directions, U and W, the rotational angle, θ, and the angular velocity, $d\theta/dt$, are presented in Fig. 4.17. It can be seen that the numerical results are insensitive to the domain size. Therefore, $W = 1.0$ m, $S = 0.6$ m and $D = 1.0$ m were used for the following computations.

Sensitivity studies on the numerical solutions to spatial and temporal discretizations were further performed. Note that finer grids and smaller time steps were required for this case in comparison with the wedge and the Wigley hull cases due to the small diameter of the cylinder, the large drop velocities, cavities and violent free surfaces.

Five minimum grid sizes, $\Delta x = 0.01$ m, 0.005 m, 0.004 m, 0.0025 m and 0.002 m, were investigated. The numerical results are presented and compared with the experimental data in Fig. 4.18. It can be observed that the numerical solutions are sensitive to the grid size. As shown in Fig. 4.19(c) and (d), larger grid sizes led to much greater discrepancies in the angular velocity and rotational angle. However, the grid size has less effect on velocities, U and W. The GCI was evaluated for the vertical position of the center of gravity of the cylinder using three sets of grids, $\Delta x = 0.01$ m, 0.005 m and 0.002 m, and the value is presented in Table 4.2. The uncertainty is

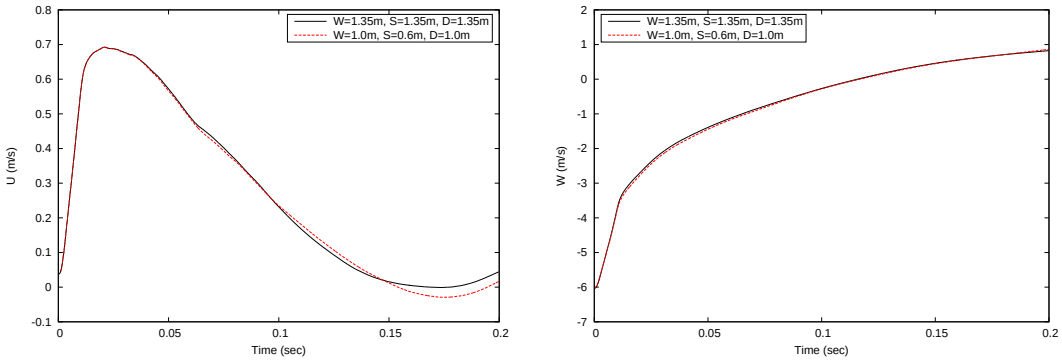

(a) U (b) W

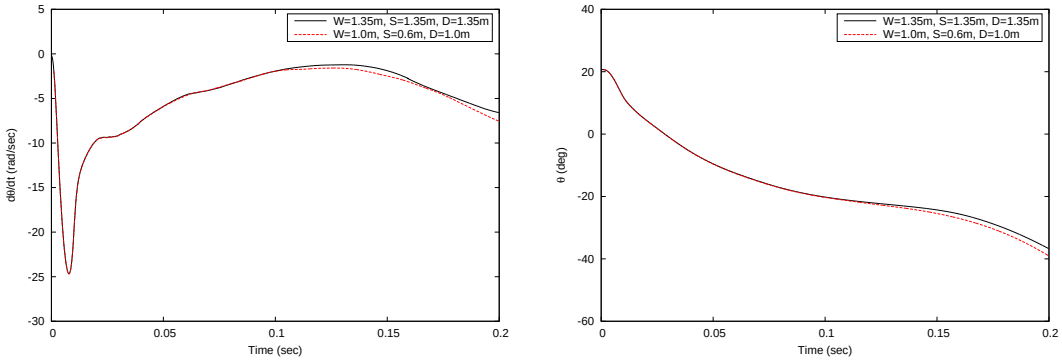

(c) $d\theta/dt$ (d) θ

Figure 4.17: Sensitivity study to domain size (Case G1)

less than 1%. It can also be seen in Fig. 4.19 that the time step has relatively small effect on the numerical solutions.

The numerical results for Cases G2 and G3 are presented in Figs. 4.20 and 4.21, respectively. The grid with a minimum grid size of 0.004 m was used and the time step was set as $\Delta t = 0.00005$ s. It can be found that the magnitude of the angular velocity increased more rapidly compared with the experimental results. The vertical velocities dropped more quickly than the experimental ones as well. The translational velocities, however, were better predicted. Although the present method works well in predicting impact forces for initial impact problems, it needs improvement for the

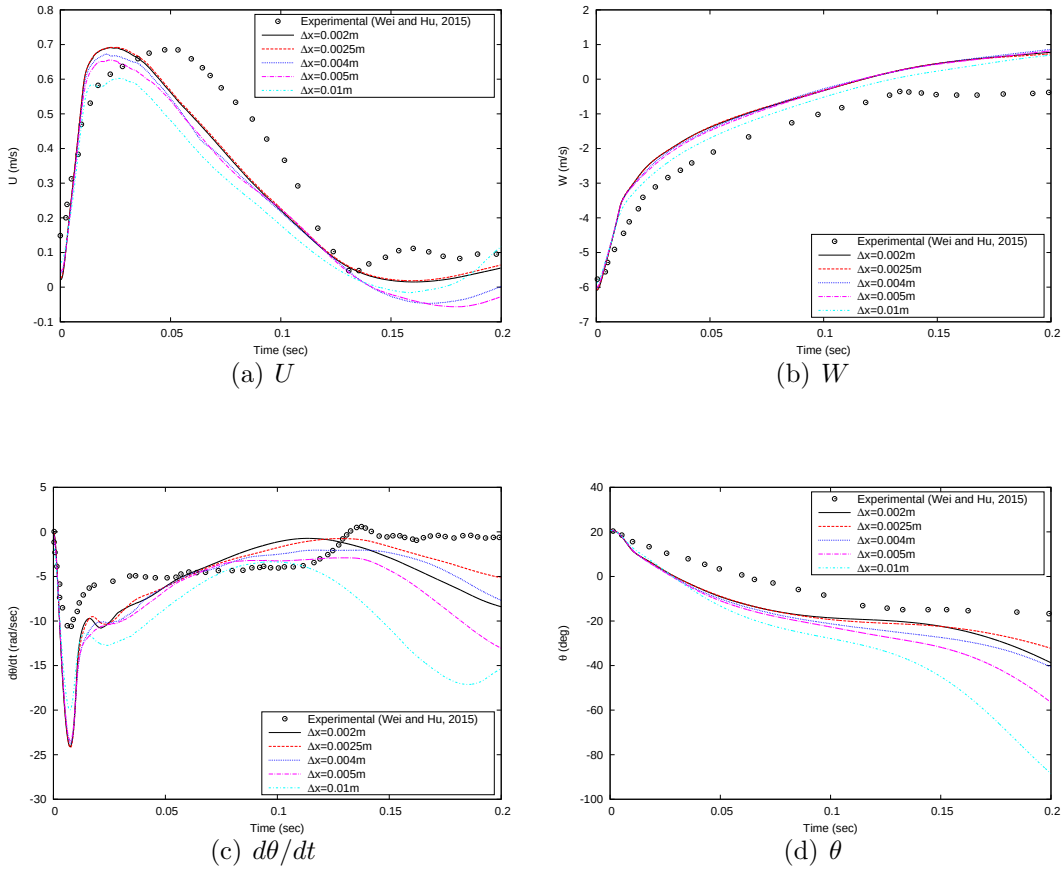

(a) U (b) W

(c) $d\theta/dt$ (d) θ

Figure 4.18: Sensitivity study to grid size (Case G1)

free fall of the inclined cylinder with rotational body motions, especially in simulating cavities and to include the exit phase.

The snap shots for flow fields at six time instants, $t = 0.002$ s, 0.013 s, 0.051 s, 0.100 s, 0.122 s and 0.143 s, are presented and compared with experimental ones in Fig. 4.22. Note that the results were based on the finest grid and $\Delta t = 0.00005$ s. The free surface contours were obtained by plotting the isosurfaces using $\phi_1 = 0.5$. The initial impact was shown in Fig. 4.22(a), and sprays at the left end were captured in Fig. 4.22(b). In Figs. 4.22(c) to (f), a cavity was formed and moved along the cylinder surface. The whole process was in general well captured by the present method.

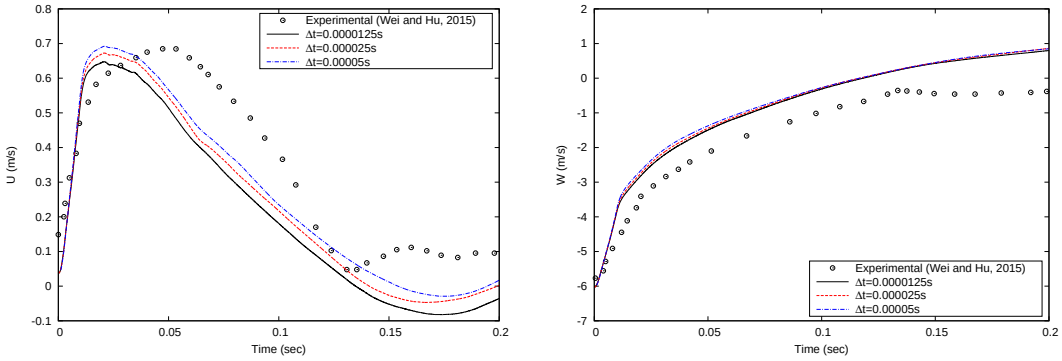

(a) U

(b) W

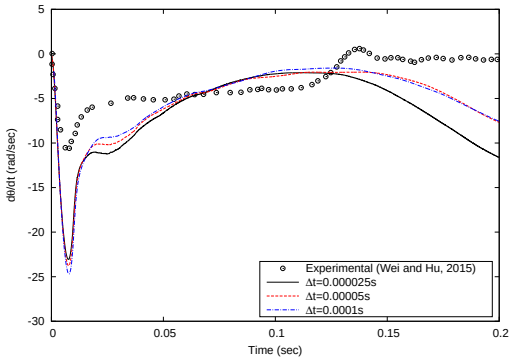

(c) $d\theta/dt$

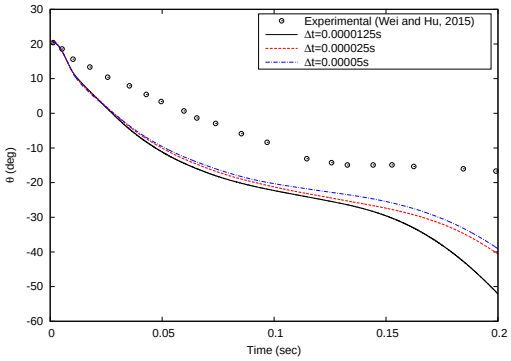

(d) θ

Figure 4.19: Sensitivity study to time step (Case G1)

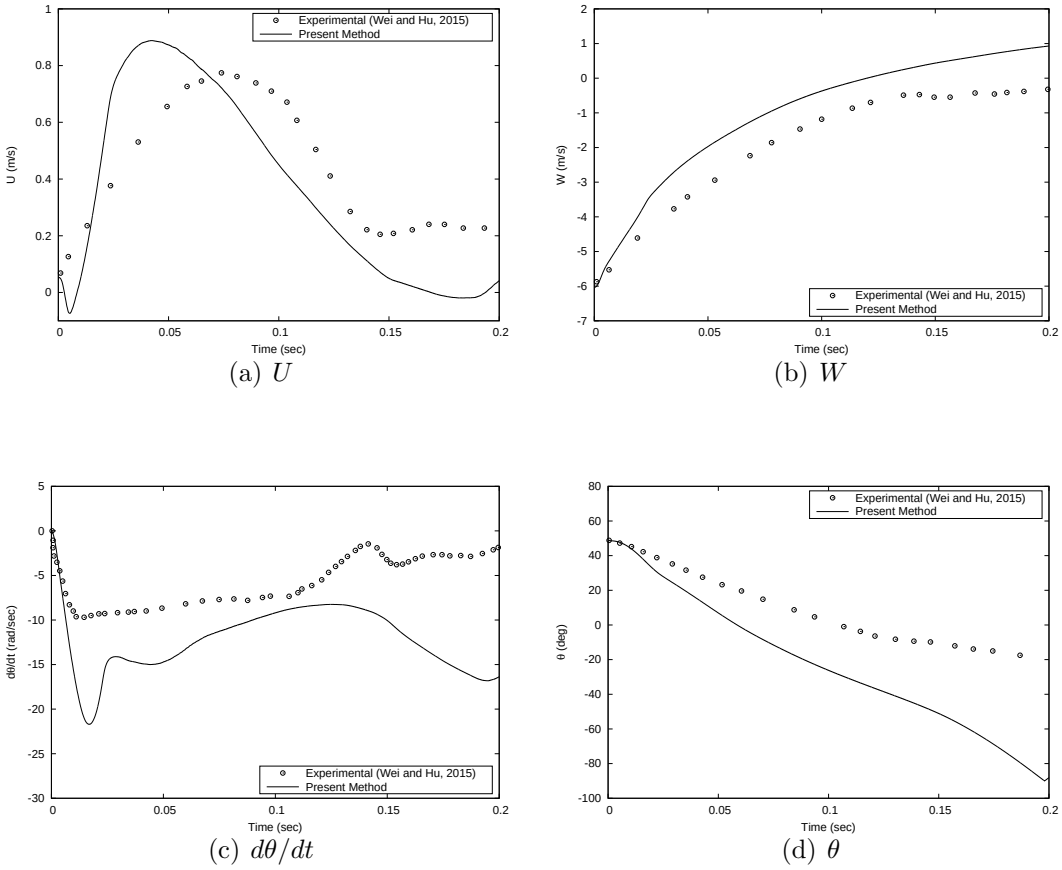

(a) U (b) W

(c) $d\theta/dt$ (d) θ

Figure 4.20: Motions of a free falling inclined cylinder (Case G2)

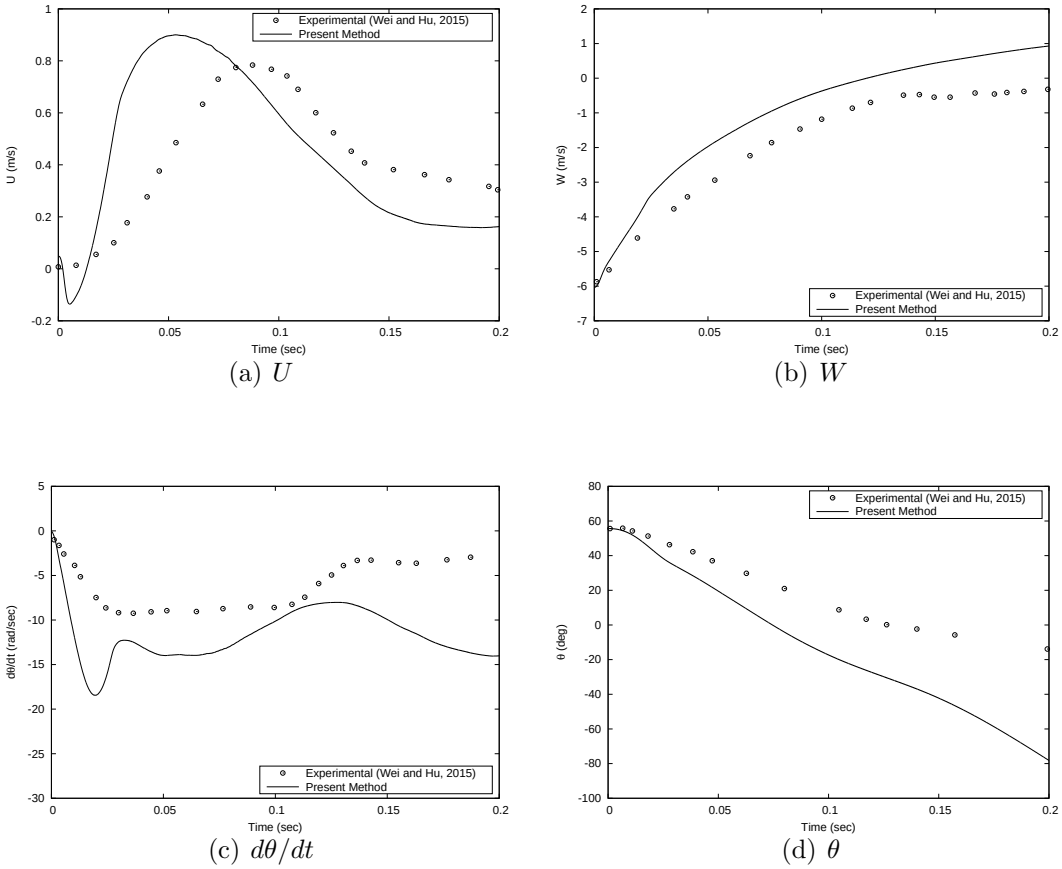

(a) U (b) W

(c) $d\theta/dt$ (d) θ

Figure 4.21: Motions of a free falling inclined cylinder (Case G3)

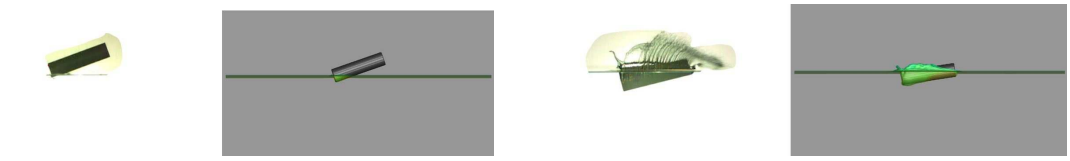

(a) $t = 0.002$ s

(b) $t = 0.013$ s

(c) $t = 0.051$ s

(d) $t = 0.1$ s

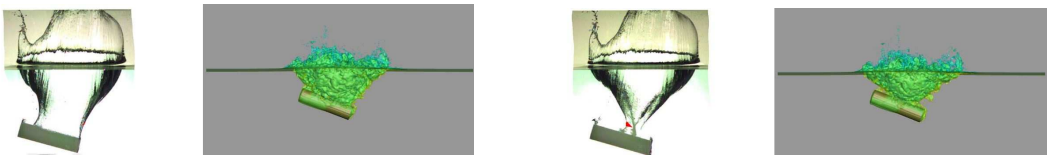

(e) $t = 0.122$ s

(f) $t = 0.143$ s

Figure 4.22: Predicted flow fields compared with experimental snapshots by Wei and Hu [87]

Chapter 5

Numerical Solutions of Water Entry in Waves

The present method was further developed to study the effect of waves in the water entry problem. First, a 3-D numerical wave tank (NWT) was implemented and the generation of propagating waves was validated. The sensitivity of the grid size was studied in both the wave height and the wave length directions. The sensitivity of the time step was also investigated.

Then, the problem of wave impact underneath fixed decks was examined. The impact wave forces on the decks were predicted and compared with experimental results by Baarholm and Faltinsen [3].

Lastly, the water entry of a 3-D wedge section into propagating waves was examined. Several parameters were varied, which included the wave height, the wave length, the entry velocity, the position of entry and the wave heading. The pressure distribution on the wedge bottom and the slamming forces were predicted and

compared with those obtained from calm water slamming.

5.1 Generation of Propagating Waves

The computational domain is demonstrated in Fig. 5.1. The width, the length and the water depth of the NWT are $W = 10$ m, $D = 1$ m and $S = 0.6$ m, respectively. The wave maker is located at one end of the tank, $x = -4.8$ m, and the damping zone is located at the other. The damping zone is defined as $X_w = 2.5$ m, $X_e = 5.0$ m, $Z_b = -1.0$ m and $Z_t = 0.1$ m. The wave is propagating along the positive x-axis.

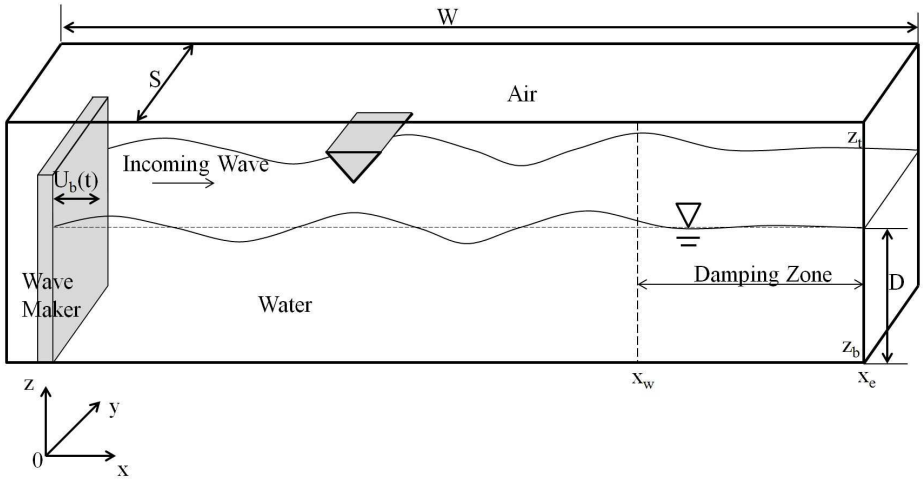

Figure 5.1: Computational domain of numerical wave tank

The wave conditions for the sensitivity studies are summarized in Table 5.1. Based on the wave maker theory by Dean [14], the stroke of the wave maker is set as $S_b = 0.054$ m. Non-uniform grids with fine grid concentrated near the water surface were used in the following computations. Fig. 5.2 presents the cross section of the mesh with an enlarged view. The grid size gradually increases towards the tank

bottom as well as in the damping zone. In the span-wise direction, the grid size was uniform.

Table 5.1: Wave conditions

	Value	Unit
Wave length λ_w	2.44	m
Wave frequency ω_w	5.02	rad/s
Wave period T_w	1.25	s
Wave height H_w	0.10	m
Wave maker stroke S_b	0.054	m

Sensitivity studies were performed on the grid sizes and the time steps. The number of grids per wave length (from 60 to 120), the number of grids per wave height (from 8 to 20) and the time step size (from 0.0002 s to 0.0004 s) were varied. The time histories of the predicted wave elevation at 2 m downstream of the wave maker are presented in Figs. 5.3 to 5.5. It is clear that the generated waves are sensitive to the change of grid sizes. The results converged with finer grid sizes. The time step size also has a slight effect on the wave elevations.

The targeted wave height was generally achieved with slightly smaller wave troughs. This is thought to be caused by the finite depth in the numerical wave tank. The free surface is presented by plotting the iso-surface of $\phi_1 = 0.5$. The snapshots of the free surface at eight time instances are shown in Fig. 5.6.

The NWT was then applied to develop waves of other wave conditions. The waves

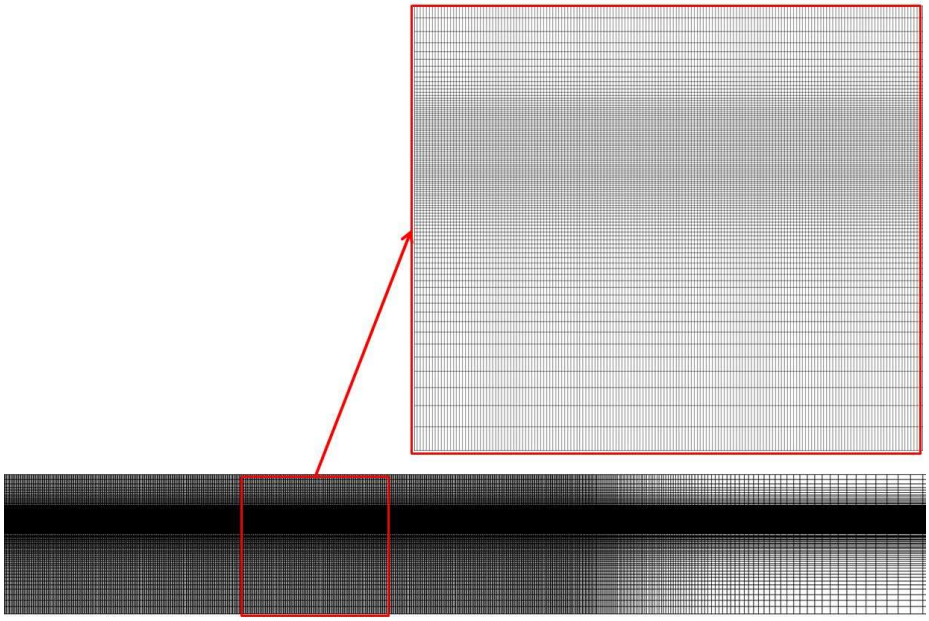

Figure 5.2: Cross section of non-uniform mesh

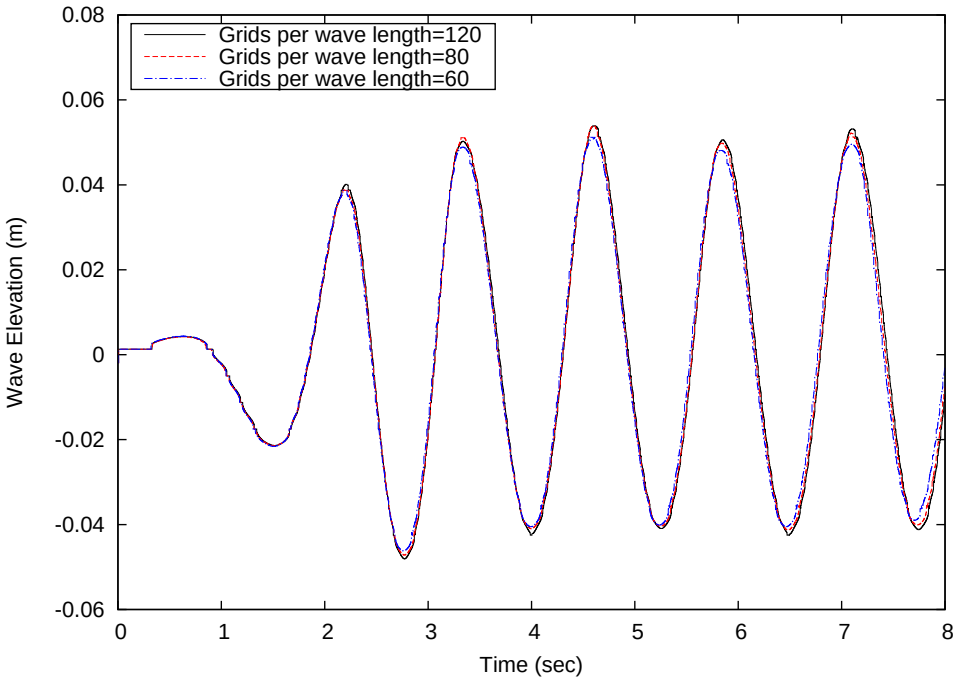

Figure 5.3: Sensitivity study on number of grids per wave length

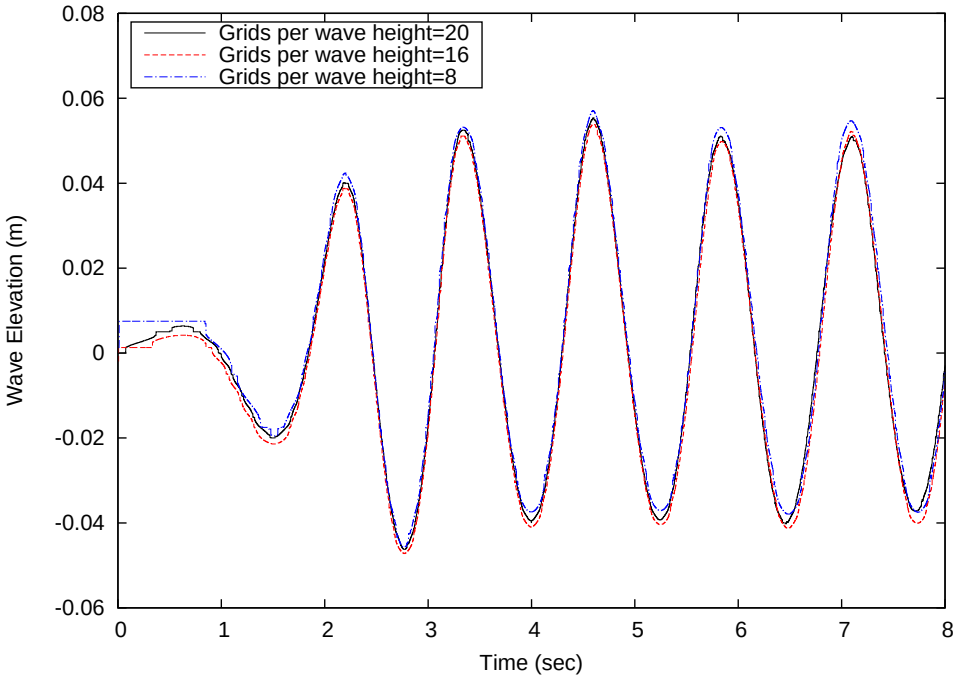

Figure 5.4: Sensitivity study on number of grids per wave height

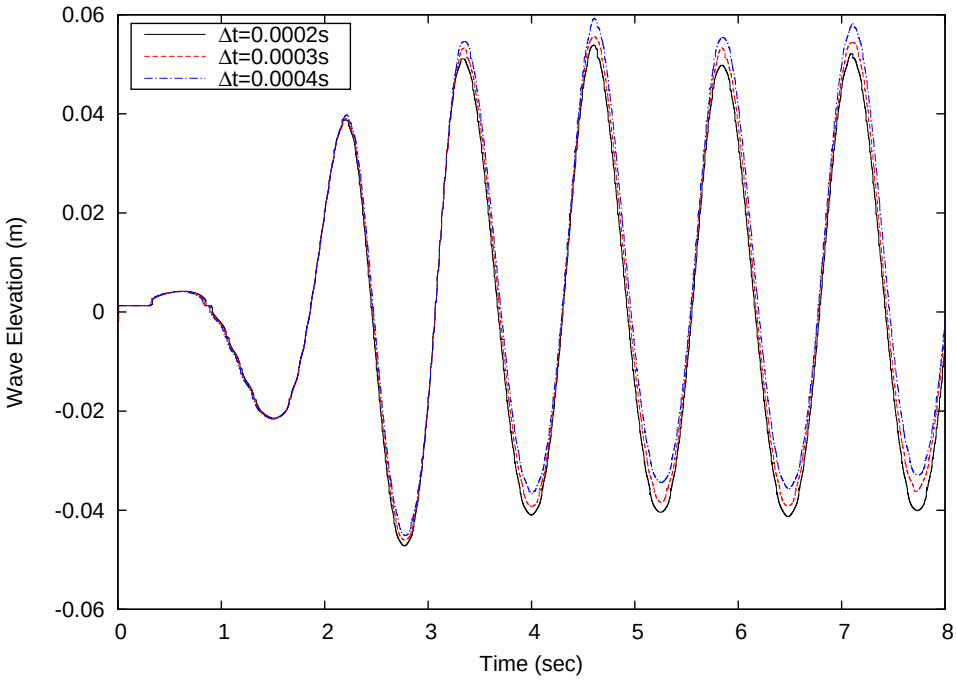

Figure 5.5: Sensitivity study on time step

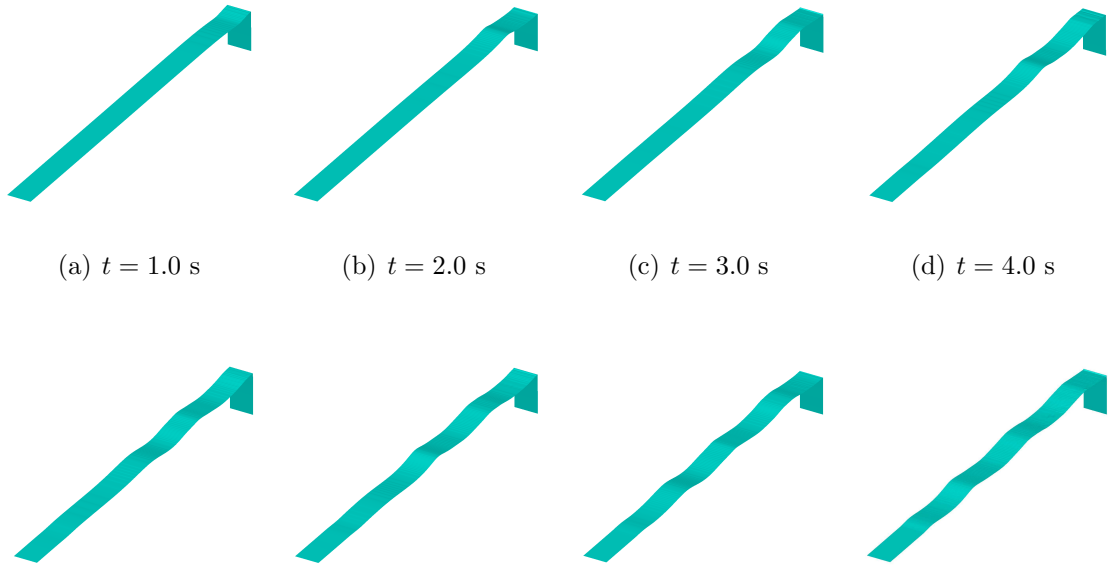

(a) $t = 1.0$ s (b) $t = 2.0$ s (c) $t = 3.0$ s (d) $t = 4.0$ s

(e) $t = 5.0$ s (f) $t = 6.0$ s (g) $t = 7.0$ s (h) $t = 8.0$ s

Figure 5.6: Predicted free surface in wave generation

with wave length of $\lambda_w = 2.44$ m and the wave height $H_w = 0.12$ m were developed. The stroke of the wave maker was set as $S_b = 0.064$ m. The wave elevation at four locations downstream of the wave maker are presented in Fig. 5.7.

Fig. 5.8 presents the wave elevations of the developed waves with $\lambda_w = 1.22$ m and $H_w = 0.03$ m at four different locations. The stroke of the wave maker for this case was set as $S_b = 0.015$ m.

5.2 Wave Impact on Fixed Decks

The problem of wave impact underneath fixed decks was then examined to further validate the numerical wave tank. The experiments conducted by Baarholm and Faltinsen [3] were simulated using the present method. The experiments were conducted in a flume with 13.5 m long, 1.3 m deep and 0.6 m wide. The platform deck,

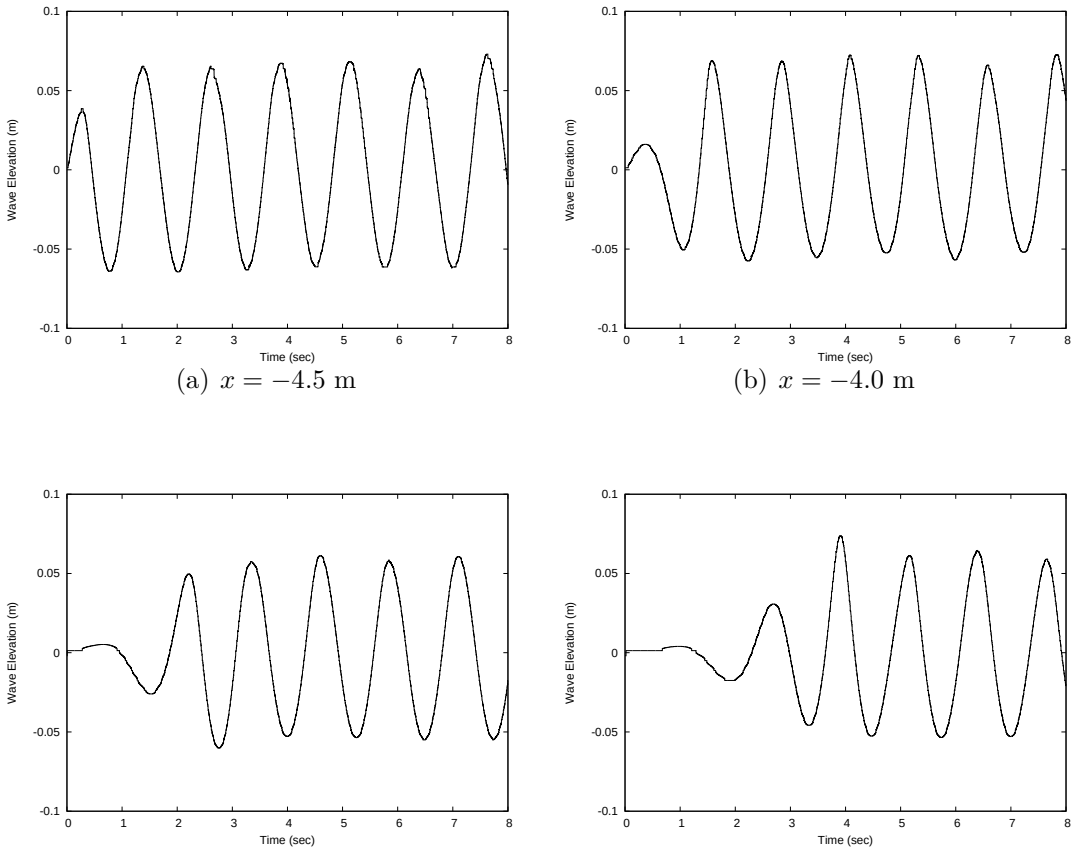

(a) $x = -4.5$ m (b) $x = -4.0$ m

(c) $x = -3.0$ m (d) $x = -2.0$ m

Figure 5.7: Time histories of wave elevation at various locations, $\lambda_w = 2.44$ m, $H_w = 0.12$ m

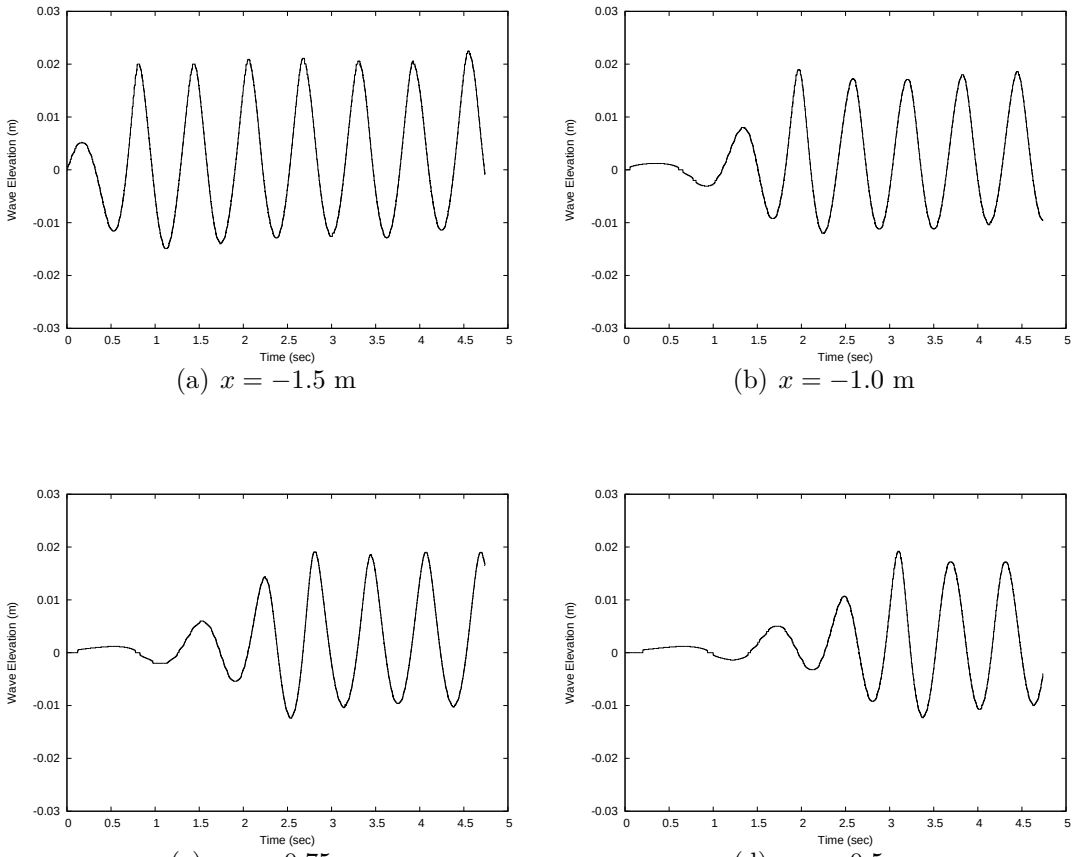

(a) $x = -1.5$ m (b) $x = -1.0$ m

(c) $x = -0.75$ m (d) $x = -0.5$ m

Figure 5.8: Time histories of wave elevation at various locations, $\lambda_w = 1.22$ m, $H_w = 0.03$ m

which was 0.63 m long and 0.56 m wide, was fixed 0.04 m above the mean free surface after the steady waves were generated. In the computations, the sizes of the numerical wave tank were kept the same as those in the experiments. Two wave conditions were used in the experiments, which are summarized in Table 5.2. The calculated strokes of the wave maker are also presented.

Table 5.2: Test conditions for wave impact on decks

Case ID	Wave length	Wave period	Wave height	Wave maker stroke
H1	2.44 m	1.25 s	0.10 m	0.054 m
H2	2.44 m	1.25 s	0.12 m	0.064 m

The vertical impact forces acting on the deck were predicted and compared with experimental data in Figs. 5.9 and 5.10 for cases H1 and H2, respectively. It can be seen that the impact forces were well predicted for both cases.

The water surfaces at eight time instances for case H2 were plotted and are presented in Fig. 5.11. The cross sections of the flow field near the deck are also shown.

5.3 Water Entry of Wedge in Waves

The present method was then extended to investigate the water entry of a 3-D wedge in propagating waves. The deadrise angle of the wedge was 45°, the breadth of the wedge, $B_w = 0.3$ m, and the length of the wedge, $L_w = 0.3$ m. The wedge entered the wave with a constant velocity, V_w. The computational domain is demonstrated

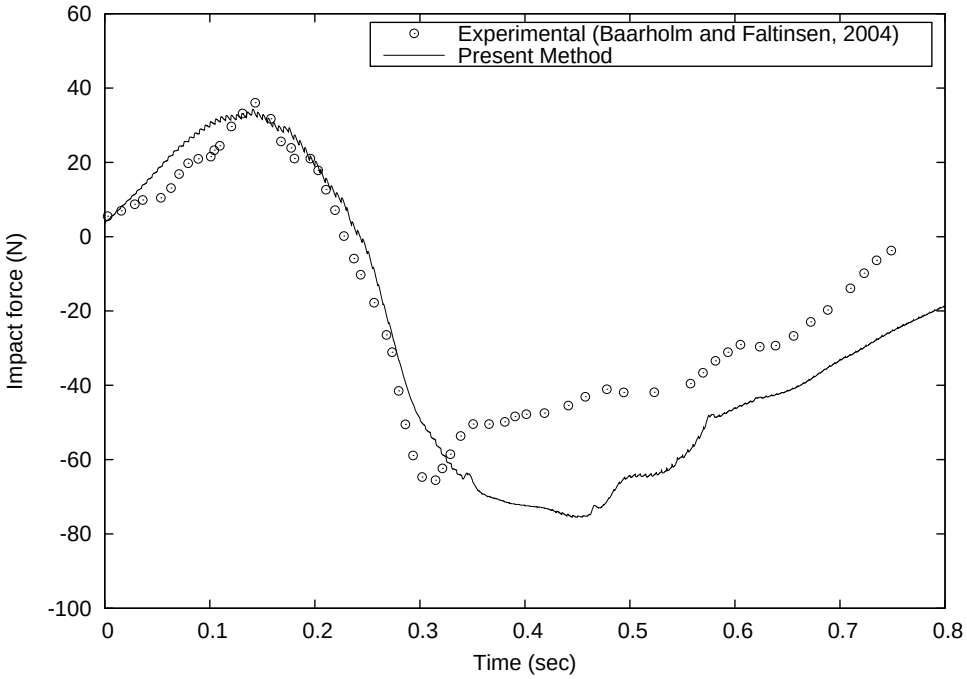

Figure 5.9: Impact force on deck (Case H1)

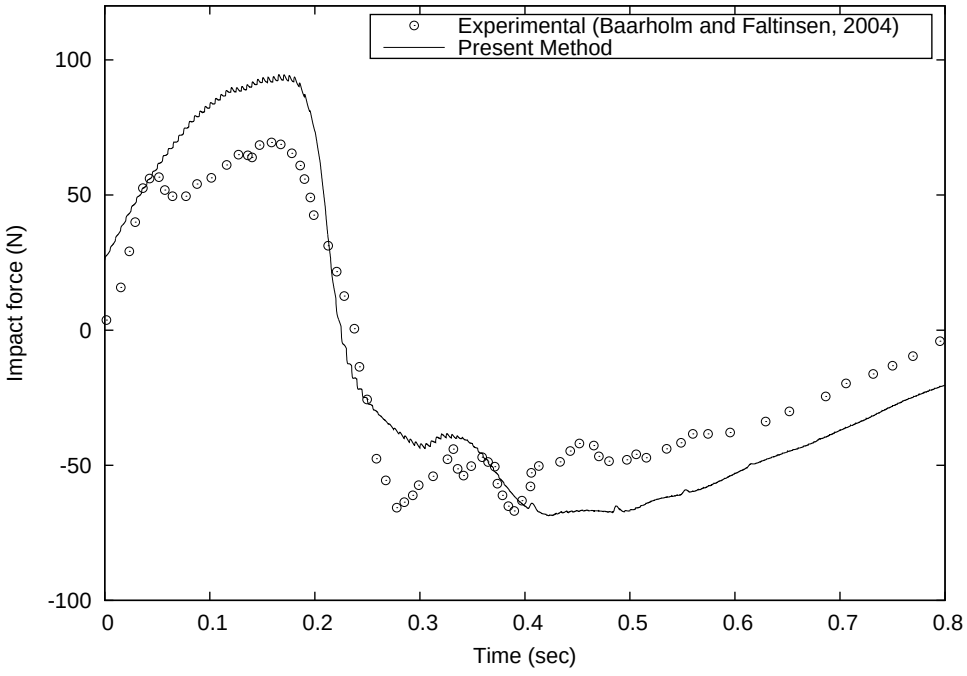

Figure 5.10: Impact force on deck (Case H2)

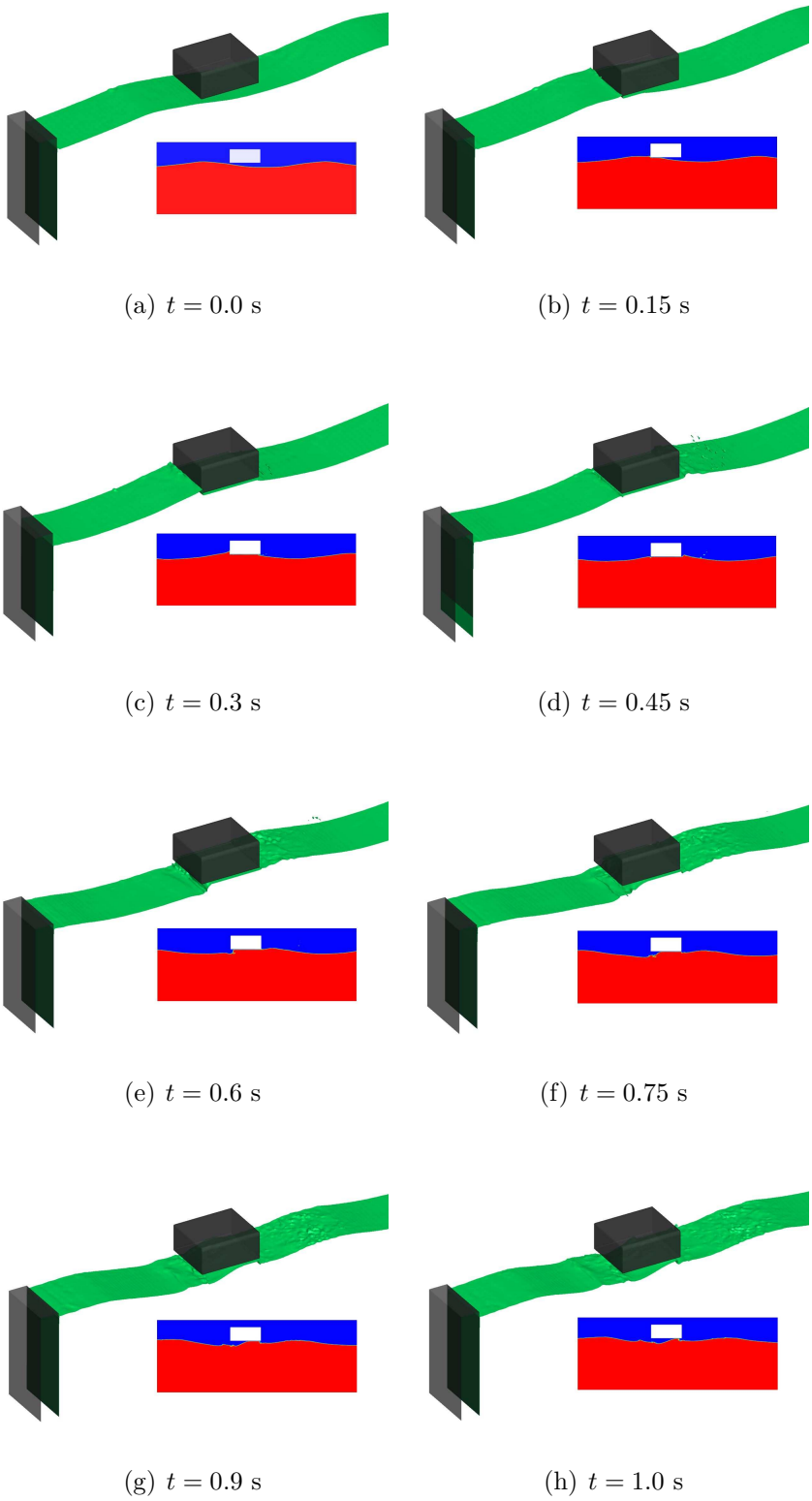

(a) $t = 0.0$ s (b) $t = 0.15$ s

(c) $t = 0.3$ s (d) $t = 0.45$ s

(e) $t = 0.6$ s (f) $t = 0.75$ s

(g) $t = 0.9$ s (h) $t = 1.0$ s

Figure 5.11: Predicted free surface in wave impact on deck (Case H2)

in Fig. 5.1. The domain sizes of the numerical wave tank were $W = 10m$, $D = 1$ m and $S = 0.6$ m. The wave maker was at $x = -4.8$ m and the damping zone was defined as $X_w = 2.5$ m, $X_e = 5.0$ m, $Z_b = -1.0$ m and $Z_t = 0.1$ m. The wave was propagating along the x-axis. In this study, several parameters, including the wave conditions (the wave length, the wave height and the encounter angle), the entry location and the entry velocity were varied. The effects of these parameters on the predicted slamming force and the pressure distribution on the wedge were examined. The numerical solutions were also compared with those obtained without waves. The test conditions are summarized in Table 5.3.

Table 5.3: Test conditions for water entry in waves

Case ID	λ_w	H_w	Wave heading	ϵ_0	Entry location	V_w
I0	-	-	-	-	Calm water	5 m/s
I1	2.44 m	0.10 m	Beam sea	0°	$x = -1.29$ m, $z = 0.053$ m (crest)	5 m/s
I2	2.44 m	0.12 m	Beam sea	0°	$x = -1.23$ m, $z = 0.065$m (crest)	5 m/s
I3	2.44 m	0.12 m	Head sea	0°	$x = -1.23$ m, $z = 0.065$ m (crest)	5 m/s
I4	2.44 m	0.12 m	Beam sea	90°	$x = -3.11$ m, $z = 0.00$ m	5 m/s
I5	2.44 m	0.12 m	Beam sea	180°	$x = -2.55$ m, $z = -0.054$ m (trough)	5 m/s
I6	2.44 m	0.12 m	Beam sea	270°	$x = -1.85$ m, $z = 0.00$ m	5 m/s
I7	2.44 m	0.12 m	Beam sea	0°	$x = -1.23$ m, $z = 0.065$ m (crest)	3 m/s
I8	2.44 m	0.12 m	Beam sea	0°	$x = -1.23$ m, $z = 0.065$ m (crest)	7 m/s
I9	0.61 m	0.03 m	Beam sea	0°	$x = -0.80$ m, $z = 0.018$ m (crest)	5m/s

To make better comparisons between these cases, in later analysis, the time, the

slamming force, the pressure and the position are non-dimensionalized as follows:

$$t' = V_w t / B_w \tag{5.1}$$

where t' is the non-dimensionalized time, V_w is the entry velocity of the wedge and B_w is the width of the wedge section,

$$x' = x/(V_w t) \tag{5.2}$$

where x' is the non-dimensionalized position and V_w is the entry velocity of the wedge,

$$C_w = \frac{F_s}{\frac{1}{2}\rho V_w^2 B_w L_w} \tag{5.3}$$

where C_w is the slamming coefficient, F_s is the slamming force, ρ is the density of water and L_w is the span-wise length of the wedge section, and

$$C_p = \frac{p}{\frac{1}{2}\rho V_w^2} \tag{5.4}$$

where C_p is the pressure coefficient and p is the pressure.

5.3.1 Wave Length

Two wave lengths, $\lambda_w = 0.61$ m and 2.44 m were applied in the study. The wedge was under the beam sea condition and the wedge entered a wave crest with $V_w = 5$ m/s after the wave was fully generated. The wave steepness was kept the same, $H_w/\lambda_w = 1/20.33$. As a result, different wave heights, $H_w = 0.12$ m and 0.03 m, were applied, respectively. The locations of the apex edge of the wedge section at the moment of touching the water are summarized in Table 5.3. The vertical and horizontal slamming forces and the pressure distribution on the wedge bottom at

four time instants, $t' = 0.167$, 0.333, 0.5 and 0.667, were predicted. The numerical solutions of cases I1 and I9 are compared with those from the water entry into calm water (case I0) in Figs. 5.12 and 5.13. Note that $t = 0.0$ s is the moment that the wedge touches the water surface.

It can be seen from Fig. 5.12 that waves lead to obvious horizontal slamming force during the water entry process. The magnitude of the horizontal slamming forces are roughly 5% of the vertical slamming forces. The predicted vertical slamming forces in case of waves are similar to those of calm water but with slightly lower magnitudes. It is also obvious that the wave length has a significant effect on the predicted slamming force. In Fig. 5.12(a), the horizontal slamming force in case of short waves ($\lambda_w = 0.61$ m) increases from zero and starts to decrease around $t' = 0.15$. It becomes negative after around $t' = 0.25$. When it comes to longer waves ($\lambda_w = 2.44$ m), the horizontal slamming force starts to decrease around $t' = 0.3$ and is above zero all the time. Discrepancies can also be found in the vertical slamming force. The magnitude of the vertical slamming force in case of shorter waves is higher in the later phase (after the peaks). The vertical slamming force in longer waves is close to the calm water, but with slightly smaller magnitude.

Asymmetrical pressure distributions can be observed in the case of water entry in waves in Fig. 5.13. The pressure on one side of the wedge section bottom that encounters the incoming waves is slightly higher than the other side during the water entry process. The asymmetrical distribution of the pressure leads to the horizontal slamming forces. The shorter wave length results in higher pressure in the later phase.

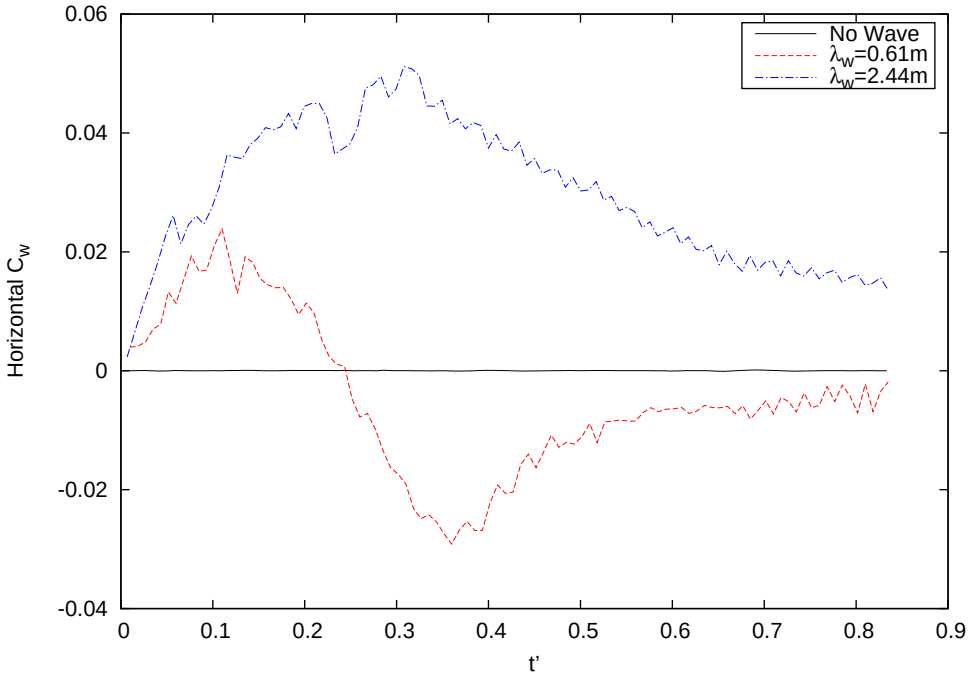

(a) Horizontal force

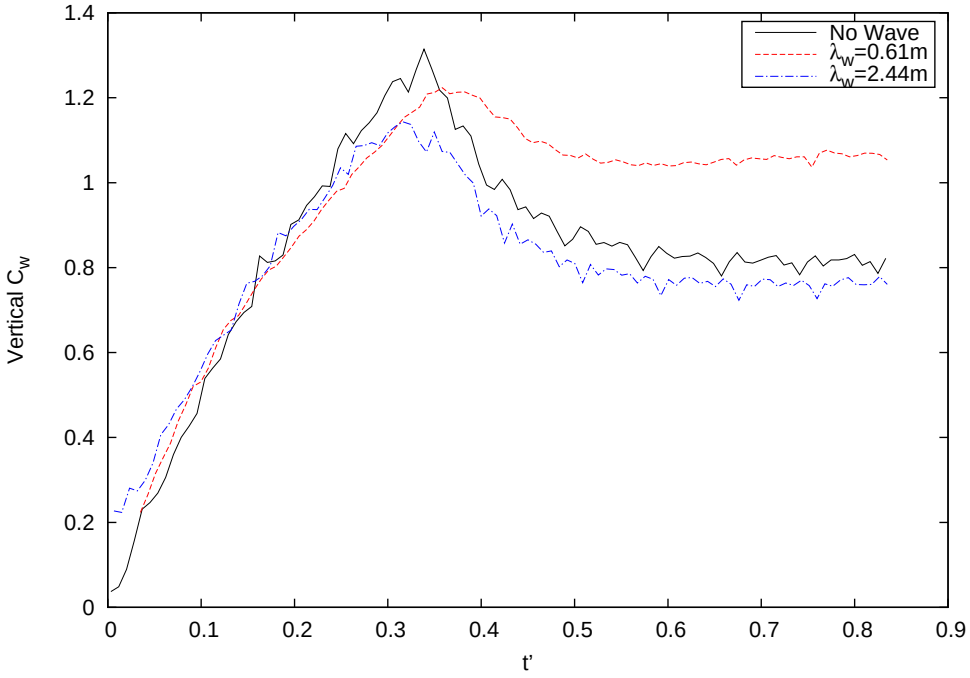

(b) Vertical force

Figure 5.12: Slamming forces on wedge in sensitivity study on wave length

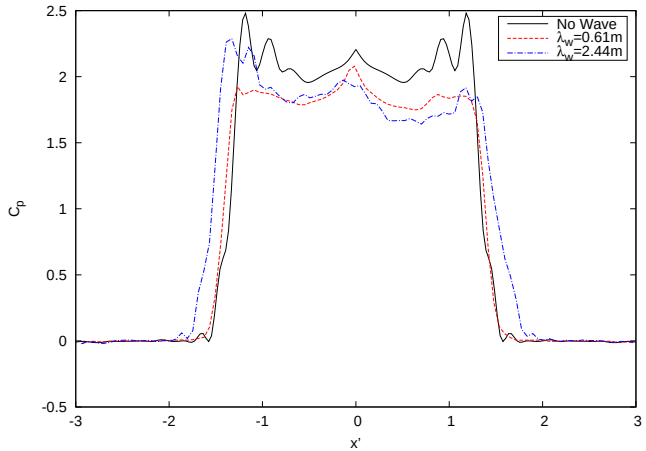

(a) $t' = 0.167$

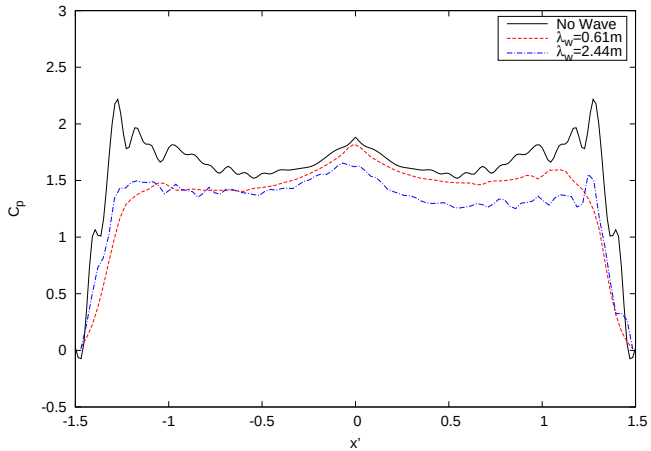

(b) $t' = 0.333$

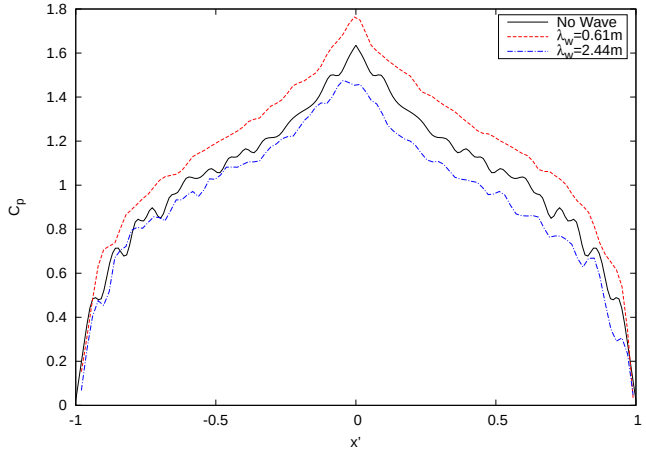

(c) $t' = 0.500$

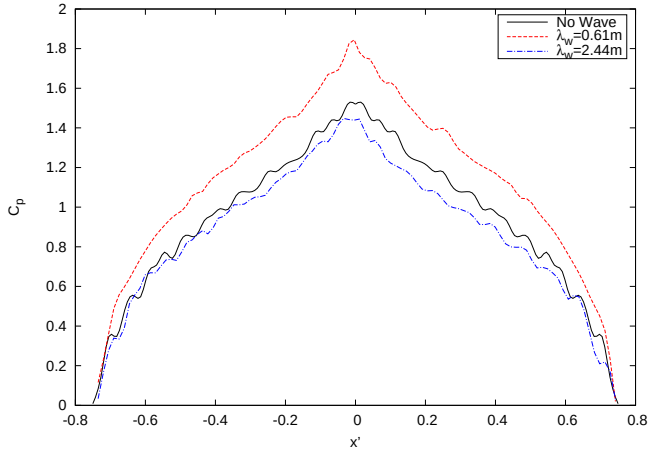

(d) $t' = 0.667$

Figure 5.13: Pressure distributions in sensitivity study on wave length

5.3.2 Wave Height

The wave length, $\lambda_w = 2.44$ m, was used in the study. The wedge was under the beam sea condition and the wedge entered a wave crest with $V_w = 5$ m/s after the wave was fully generated. Two different wave heights, $H_w = 0.10$ m and 0.12 m were studied. The locations of the apex edge of the wedge section at the moment of touching the water are summarized in Table 5.3. The vertical and horizontal slamming forces and the pressure distribution on the wedge bottom at four time instants, $t' = 0.167$, 0.333, 0.5 and 0.667, were predicted. The numerical solutions of cases I1 and I2 are compared with those from the water entry into calm water (case I0) in Figs. 5.14 and 5.15.

Obvious horizontal slamming force can also be observed in Fig. 5.14. The magnitude of the horizontal slamming forces are roughly 5% of the vertical slamming forces. The maximum horizontal slamming force occurs at the same time with the vertical slamming force. As for the vertical slamming forces, predicted values in case of waves are similar to those of calm water but with slightly lower magnitudes. The predicted slamming forces from the two wave height conditions are very similar. The wave height has minimal effect on the slamming force.

Asymmetrical pressure distributions can be observed in the cases with waves in Fig. 5.15. The pressure on the side of the wedge that encounters the incoming waves is slightly higher than the other side during the water entry process. The asymmetrical distribution of the pressure leads to the horizontal slamming forces. It can also be seen that the predicted pressures in case of waves are slightly lower than those of calm water. The wave height has minimal effect on the predicted pressure as well.

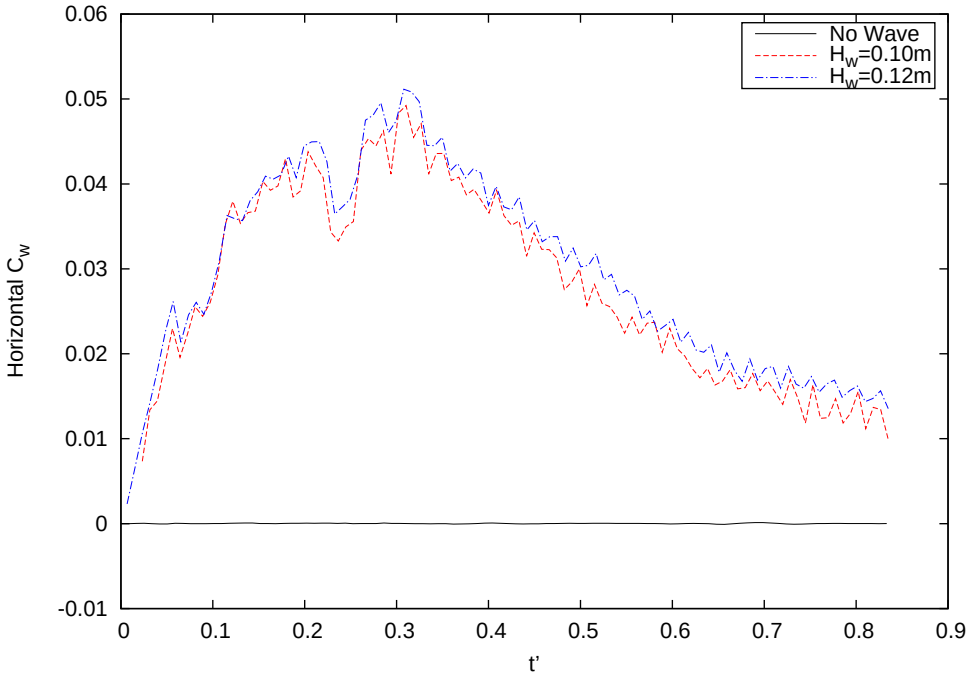

(a) Horizontal force

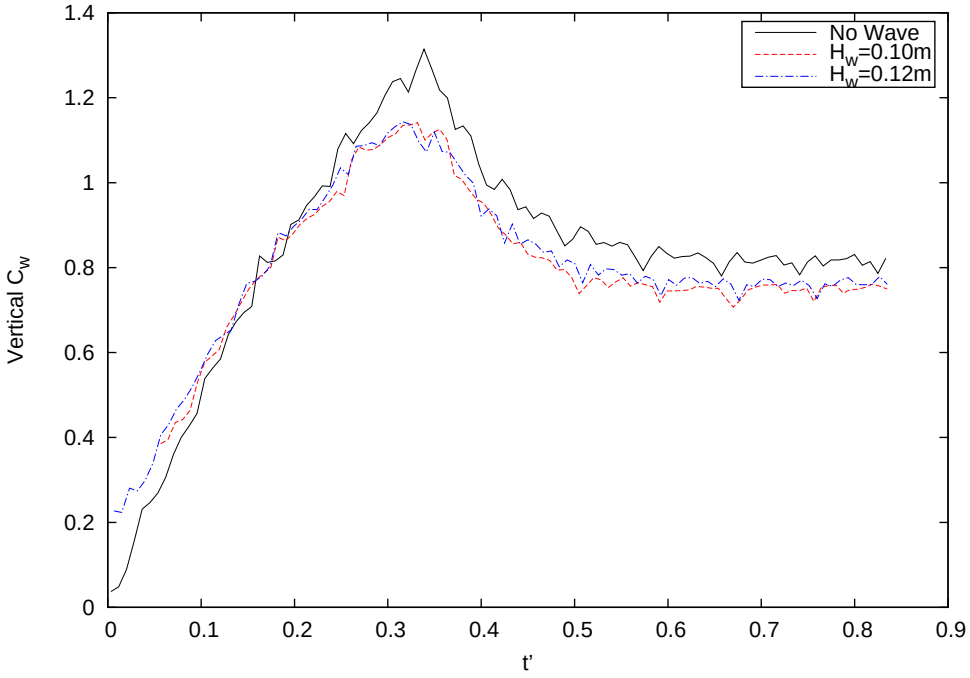

(b) Vertical force

Figure 5.14: Slamming forces on wedge in sensitivity study on wave height

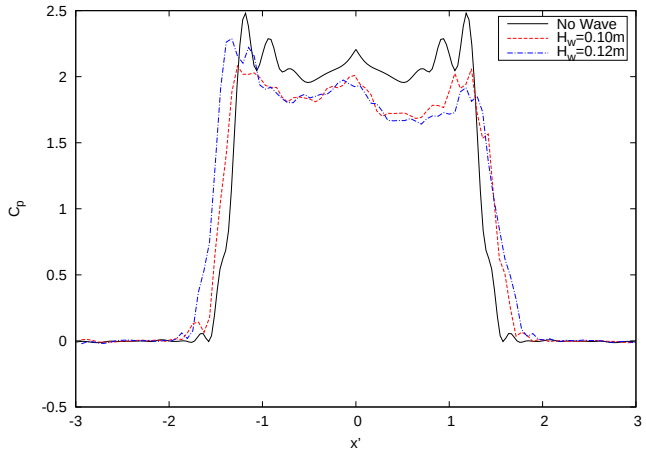

(a) $t' = 0.167$

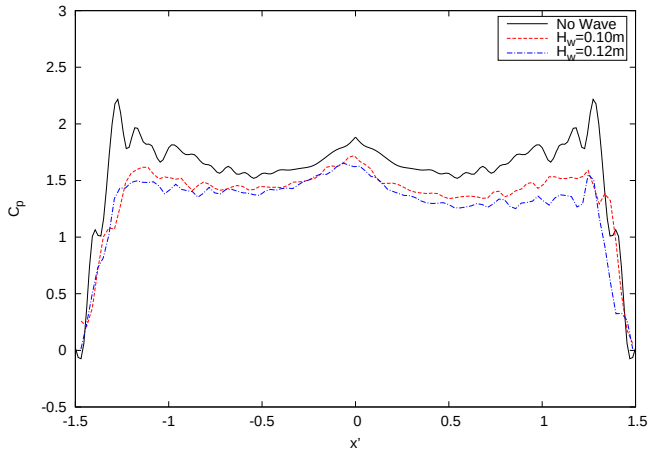

(b) $t' = 0.333$

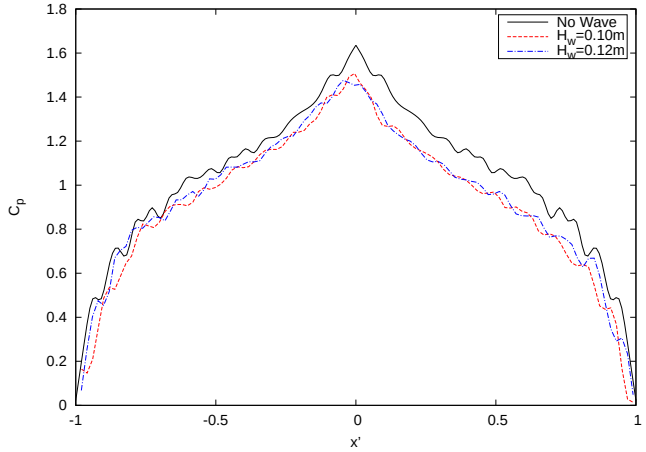

(c) $t' = 0.500$

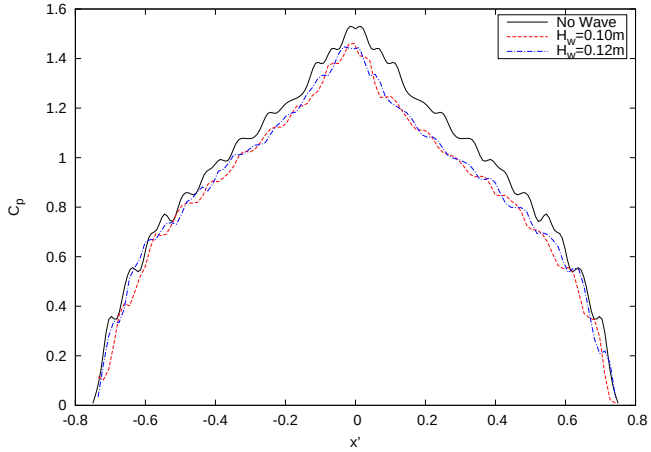

(d) $t' = 0.667$

Figure 5.15: Pressure distributions in sensitivity study on wave height

5.3.3 Encounter Angle

The effect of the orientation of the wedge section relative to the incoming waves was studied. The wave length, $\lambda_w = 2.44$ m, and the wave height, $H_w = 0.12$ m, were used in the study. The wedges entered the wave crest with two different orientations, the head sea condition and the beam sea conditions, as demonstrated in Fig. 5.16. The entry velocity of the wedge was $V_w = 5$ m/s. The locations of the apex edge of the wedge section at the moment of touching the water are summarized in Table 5.3. The vertical and horizontal slamming forces and the pressure distribution on the wedge bottom at four time instants, $t' = 0.167$, 0.333, 0.5 and 0.667, were predicted. The numerical solutions of cases I2 and I3 are compared with those obtained from calm water (case I0) in Figs. 5.17 and 5.18. Note that the horizontal slamming force is the impact force in the x-axis.

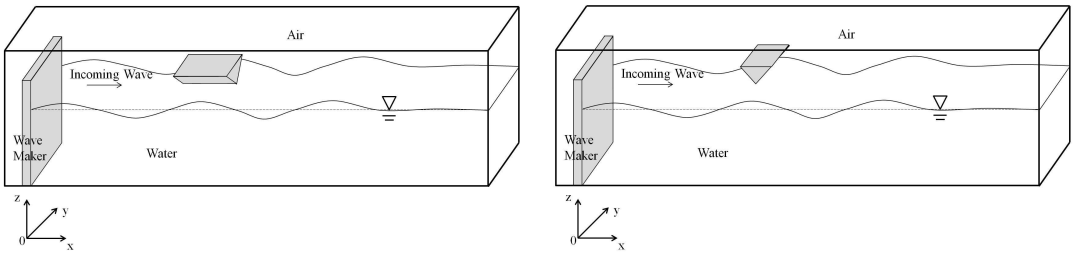

(a) Head sea condition (b) Beam sea condition

Figure 5.16: Demonstration of orientation of wedge

It can be seen from Fig. 5.17 that the orientation of the wedge has a significant effect on the horizontal slamming force. When it comes to the head sea condition, the horizontal slamming force is close to zero. It is also clear that the vertical slamming forces in the head sea condition are slightly higher than those in the beam sea

condition. They are both close to those of calm water. The existence of waves has minimal effect on the vertical slamming force and the pressure distribution on the wedge bottom. It can be observed in Fig. 5.18 that the predicted pressure distributions on the wedge bottom are close to each other based on different wave headings. Asymmetrical pressure distribution can be observed in the beam sea condition while it is symmetrical in the head sea condition as well as in the calm water.

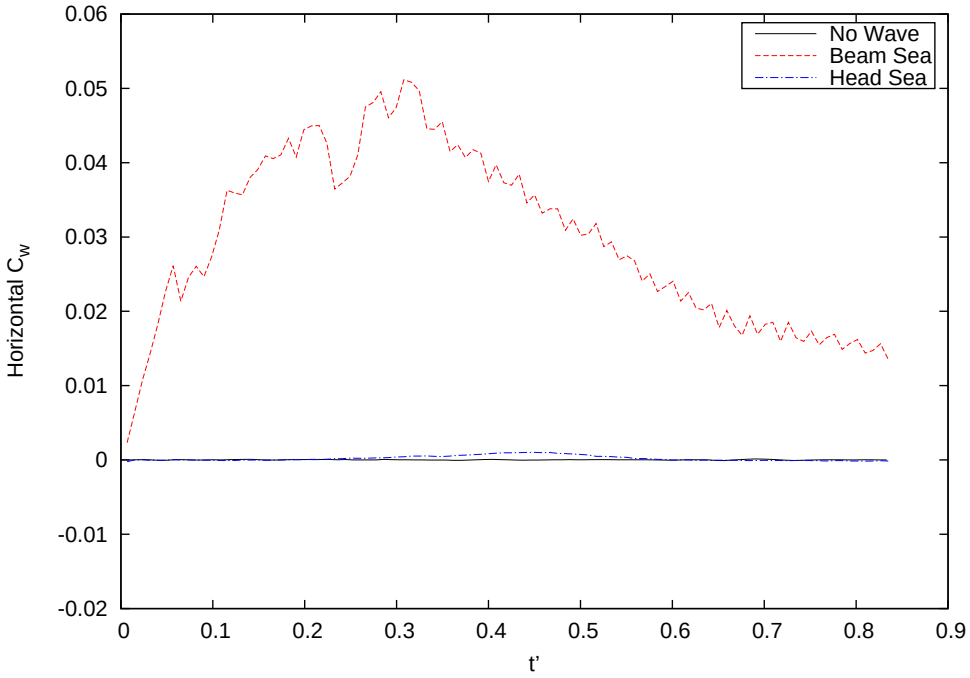

(a) Horizontal force

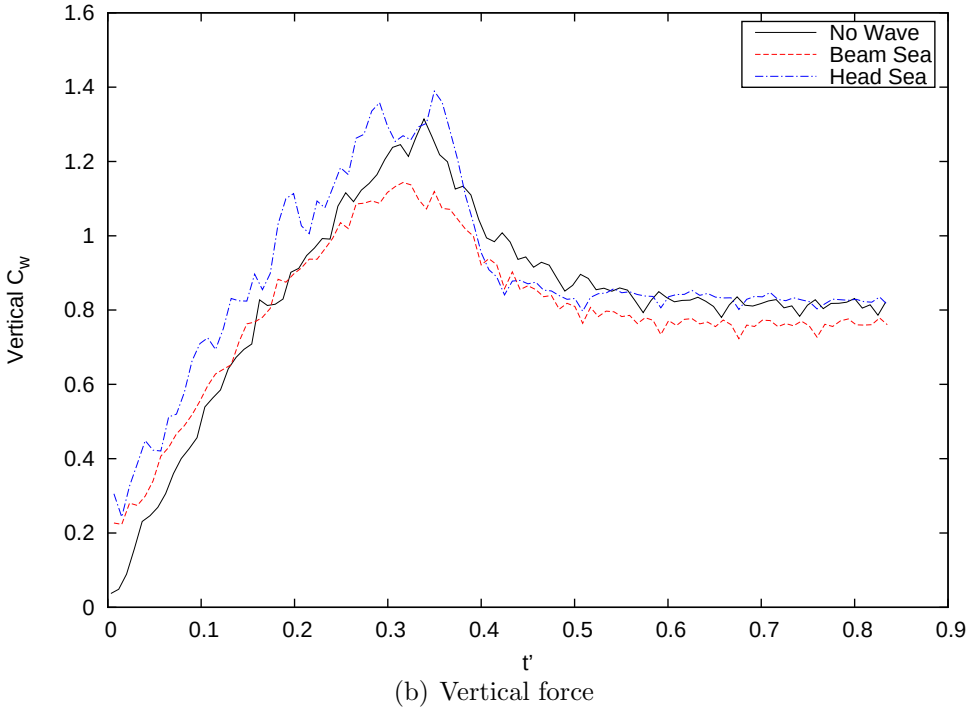

(b) Vertical force

Figure 5.17: Slamming forces on wedge in sensitivity study on wave heading

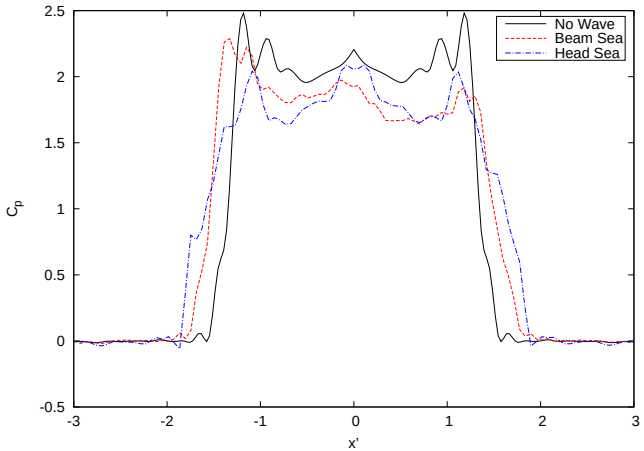

(a) $t' = 0.167$

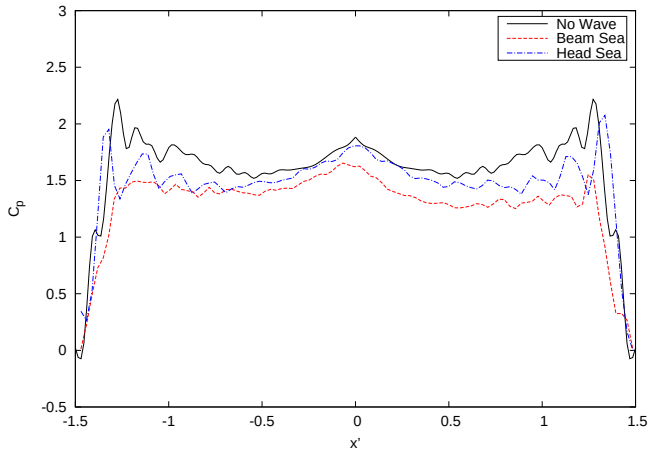

(b) $t' = 0.333$

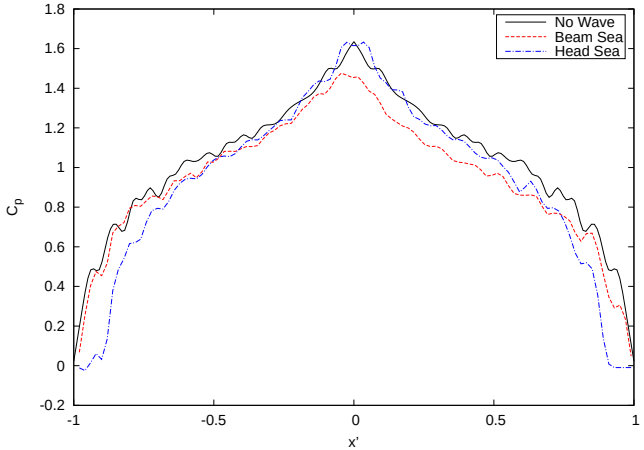

(c) $t' = 0.500$

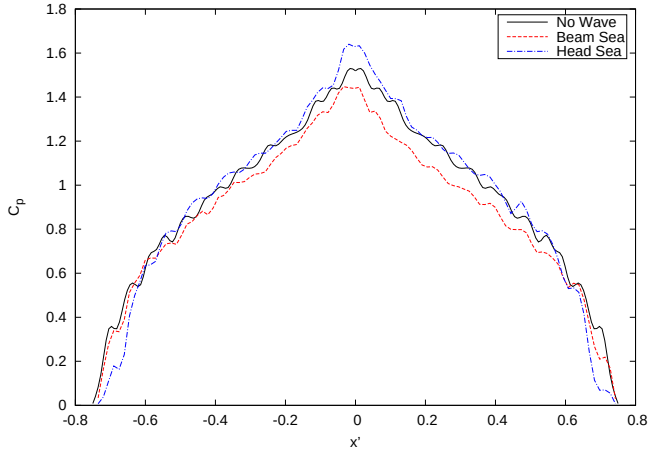

(d) $t' = 0.667$

Figure 5.18: Pressure distributions in sensitivity study on wave heading

5.3.4 Entry Location

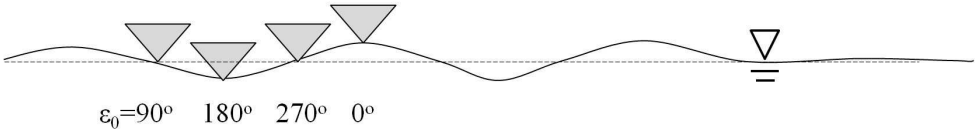

Figure 5.19: Demonstration of entry locations

The effect of the entry location in waves was studied. The wave length, $\lambda_w = 2.44$ m, and the wave height, $H_w = 0.12$ m, were used in this study. The wedge was under the beam sea condition and the wedge entered water with $V_w = 5$ m/s. Four different entry locations (Fig. 5.19), $\epsilon_0 = 0°$ (wave crest), 90°, 180° (wave trough) and 270°, were studied. The locations of the apex edge of the wedge section at the moment of touching the water are summarized in Table 5.3. The vertical and horizontal slamming forces and the pressure distribution on the wedge bottom at four time instants, $t' = 0.167$, 0.333, 0.5 and 0.667, were predicted. The numerical solutions of cases I2, I4, I5 and I6 are compared with those obtained based on calm water (case I0) in Figs. 5.20 and 5.21. Again, $t = 0.0$ s is the moment that the wedge touches the water surface.

It can be seen in Fig. 5.20 that the location of entry in waves has a significant effect on the horizontal and the vertical slamming force. The horizontal slamming force is negative in the case of wave trough ($\epsilon_0 = 180°$) while it is positive in the case of wave crest ($\epsilon_0 = 0°$). The horizontal slamming force is negative first, then turns to positive in the case of $\epsilon_0 = 270°$. The trend is opposite in the case with $\epsilon_0 = 90°$. This is thought to be caused by the different wave slopes and particle velocity at

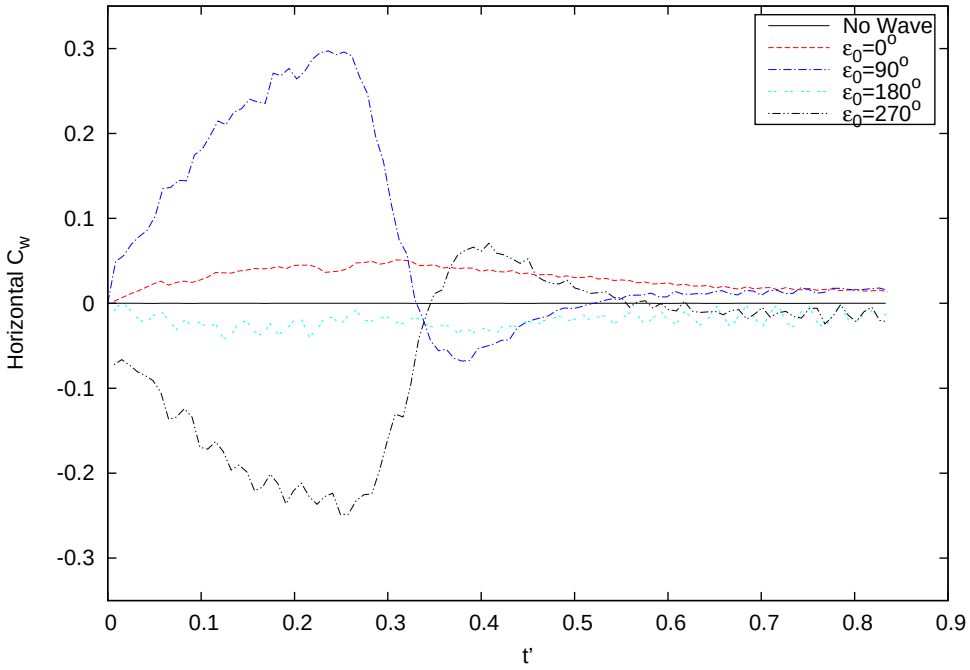

(a) Horizontal force

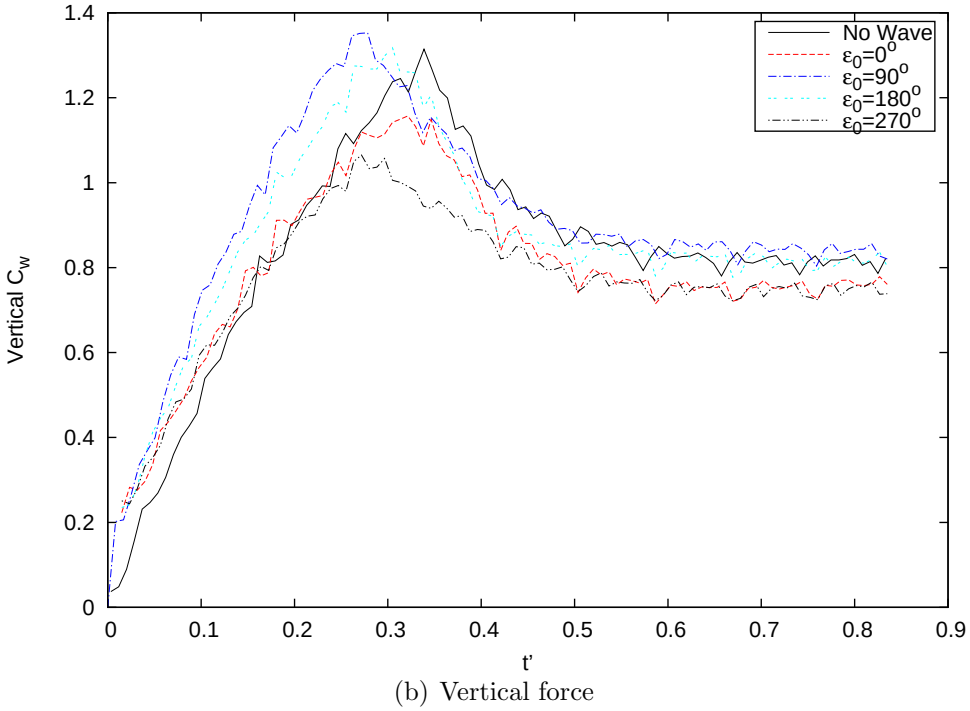

(b) Vertical force

Figure 5.20: Slamming forces on wedge in sensitivity study on entry location

different locations of a wave surface. The local fluid velocity is pointing to positive x-axis, positive z-axis, negative x-axis and negative z-axis directions in the case of $\epsilon_0 = 0°$, $90°$, $180°$ and $270°$, respectively. It thus changes the relative velocity of the wedge with regards to the local fluid. In terms of the vertical slamming force, the highest vertical slamming force happens in the case of $\epsilon_0 = 90°$ where the local fluid velocity is pointing upwards. The lowest vertical slamming force happens in the case of $\epsilon_0 = 270°$ where the local fluid velocity is pointing downwards. It is also clear in Fig. 5.21 that increased local pressure can occur, comparing with that of calm water case.

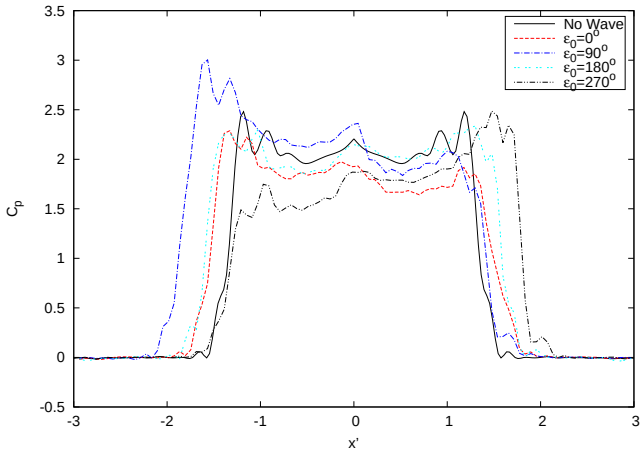

(a) $t' = 0.167$

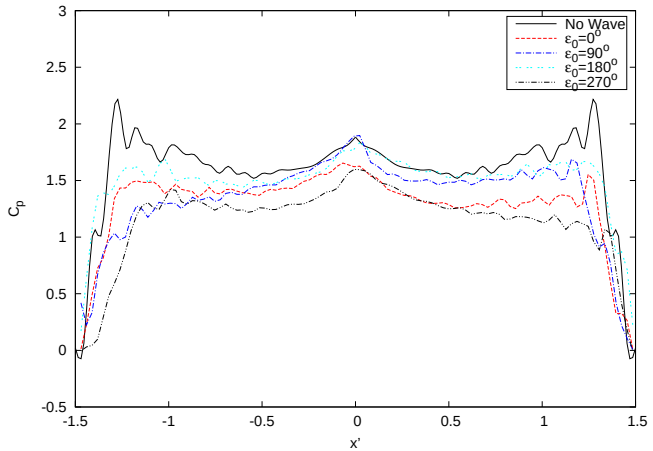

(b) $t' = 0.333$

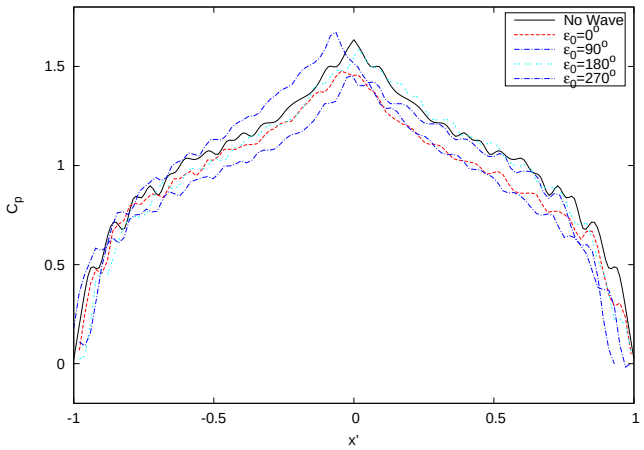

(c) $t' = 0.500$

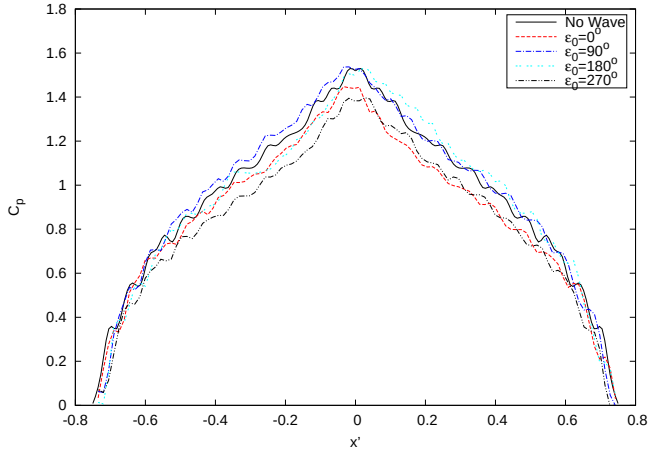

(d) $t' = 0.667$

Figure 5.21: Pressure distributions in sensitivity study on entry location

5.3.5 Entry Velocity

The effect of the entry velocity was studied. The wave length, $\lambda_w = 2.44$ m, and the wave height, $H_w = 0.12$ m, were used in the study. The wedge was under the beam sea condition and the wedge entered the wave crest ($\epsilon_0 = 0°$). Three different entry velocities, $V_w = 3$ m/s, 5 m/s and 7 m/s, were studied. The vertical and horizontal slamming forces and the pressure distribution on the wedge bottom at four time instants, $t' = 0.167$, 0.333, 0.5 and 0.667, were predicted. The numerical solutions of cases I2, I7 and I8 are compared with those from the calm water (case I0) in Figs. 5.22 and 5.23.

It can be seen in Fig. 5.22 that the horizontal slamming force coefficient is sensitive to the entry velocity while the vertical slamming force is not. Higher entry velocity leads to lower horizontal slamming force coefficient. It is also clear that higher entry velocity leads to higher slamming force in both horizontal and vertical directions. Similar observation can be found in Fig. 5.23. Lower entry velocity leads to higher pressure coefficient but lower pressure on the wedge bottom.

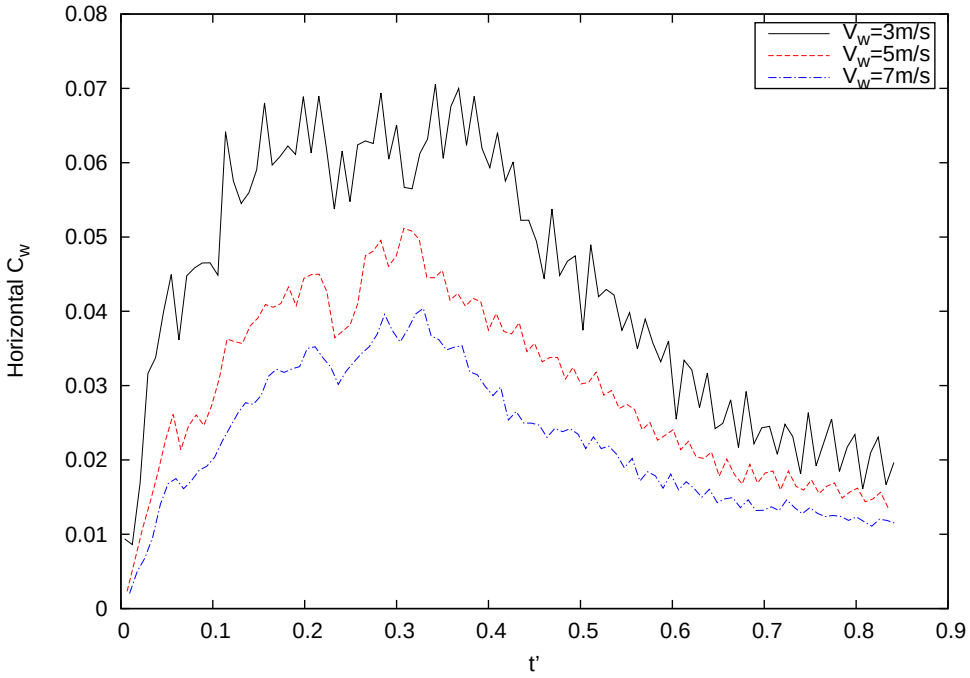

(a) Horizontal force

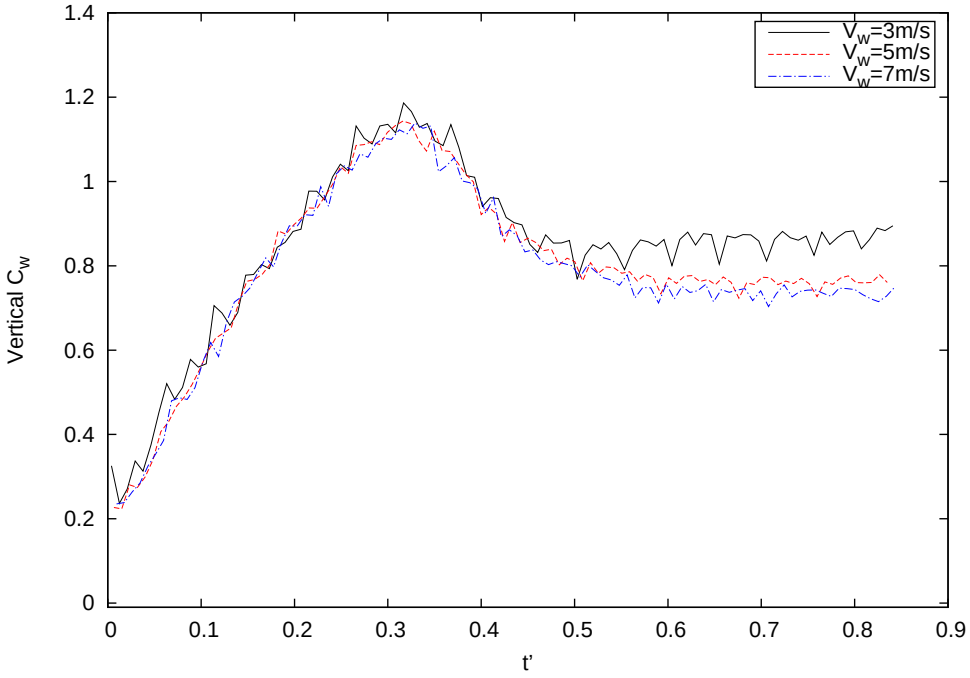

(b) Vertical force

Figure 5.22: Slamming forces on wedge in sensitivity study on entry velocity

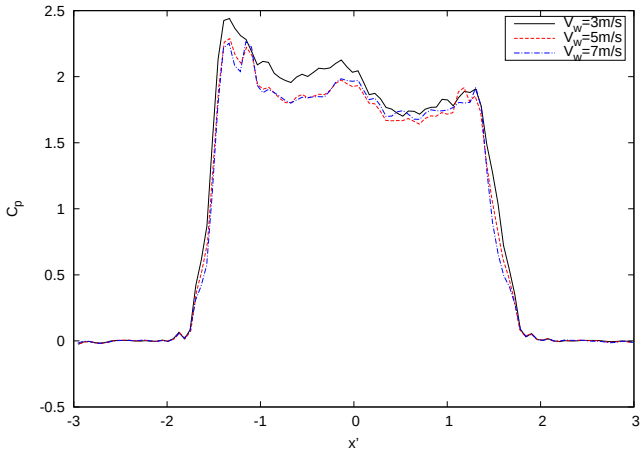

(a) $t' = 0.167$

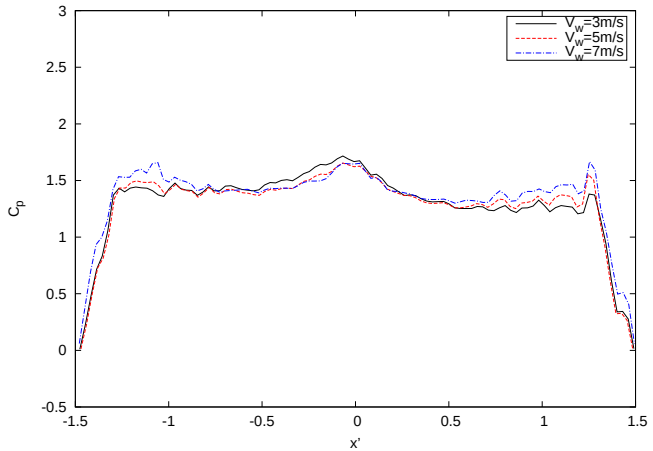

(b) $t' = 0.333$

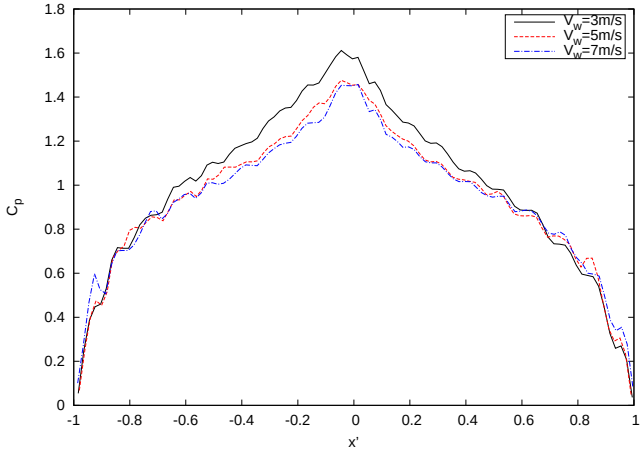

(c) $t' = 0.500$

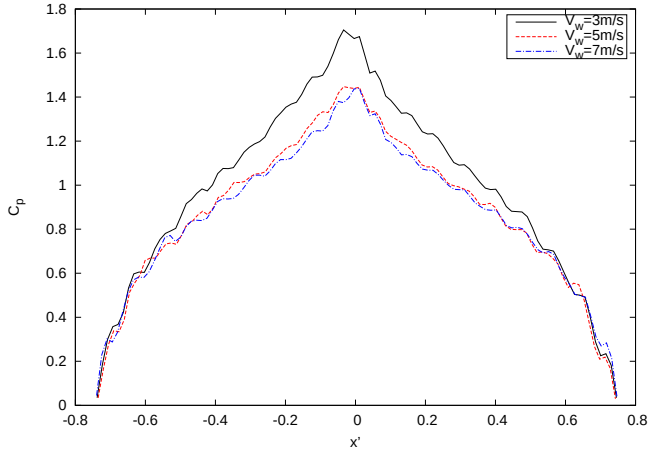

(d) $t' = 0.667$

Figure 5.23: Pressure distributions in sensitivity study on entry velocity

Chapter 6

Conclusions and Future Work

6.1 Conclusions

This thesis presents an improved CIP-based flow solver and studies water entry problems of 2-D and 3-D objects numerically. The present method shows better predictions of the impact forces and pressures during the water entry process than the VOF method and the BEM. By implementing the THINC/WLIC scheme, it is also capable of capturing the violent free surface, jets and bubbles with better accuracy and sharpness. By applying a parallel computing algorithm based on MPI, the present method allows the use of much finer grids and smaller time steps. Close to linear speed-up performance was achieved when using up to 50 CPUs. Computations with free fall motions showed solutions as good as with prescribed motions. In this research, the water entry of 2-D and 3-D objects in calm water was studied first. Then the water entry in regular waves was examined. Validation studies of the present method were carried out for water entry of several 2-D and 3-D objects and wave

impact underneath a fixed deck.

The water entry of 2-D symmetric and asymmetric wedges and ship sections with different drop heights was first studied by the present method. It was found that the water entry problem in general requires fine grids and small time steps. The solutions are not sensitive to the domain sizes. The prediction of the rise time and the delay time in the time histories of pressures and impact forces is very sensitive to the grid size. The convergence studies showed acceptable GCI values. The interface capturing schemes have significant effects on the solutions. The THINC/WLIC scheme and the THINC scheme, used for interface capturing of the free surface and as a part of the CIP based method, lead to much better prediction of slamming forces and pressures than the original CIP scheme. The compressibility only influences the force/pressure prediction with the existence of air pockets in the later phase of the initial impact. The peak pressure/force and the rise time, however, are not affected by the compressibility. The compressible solver is needed only in the case with trapped air pockets and high entry velocity. The computations considering free fall motions showed good results as with prescribed motions. The rise time, delay time, peak pressure/force and time difference were compared with experimental data. Generally good agreement was found. The delay time was over-predicted in the ship section cases.

The present method was further validated by simulating the water entry of a three-dimensional wedge, a modified Wigley hull and an inclined cylinder. The incompressible solver and the THINC/WLIC interface capturing scheme were used in this study and the study was focused on the prediction of slamming force, free surface and the motion trajectories of the objects. Relatively fine grids and time step size were required for the 3-D slamming cases. The solutions were more sensitive to the

grid size than the time step. The numerical solutions were in good agreement with the experimental results. The 3-D effect resulted in lower slamming forces in the wedge case. When comparing with other numerical methods (original CIP, VOF and BEM), the present method led to much better agreement with the experimental results. The results for the Wigley hull case showed less than 10% difference from experimental data. The results for the inclined cylinder case were also in good agreement with experimental results, even though it was more difficult to simulate due to the cavities and the exit phase. It was found that the present method considering free motions is able to solve the slamming problems involving breaking free surfaces and air bubbles with good performance in terms of speed-up and accuracy. On the other hand, the present method needs improvement in simulating the later phase of free fall problems coupled with complex cavity dynamics and rotational body motions.

A numerical wave tank (NWT) was then simulated using the present method. A piston type wave maker and a damping zone were implemented. The NWT was validated by generating regular waves with various wave lengths and wave heights. The NWT was further validated by simulating the wave impact underneath a fixed deck. The predicted impact forces on the deck were in good agreement with experimental data. In the study of water entry into waves, it was found that waves result in obvious horizontal slamming forces in phase with the vertical slamming forces and with the magnitude of approximately 5% of vertical slamming forces. The vertical slamming forces due to waves tend to be slightly lower than those in calm water. Although the slamming forces were not significantly affected, asymmetrical pressure distribution on the bottom of the wedge was observed. Higher local pressure concentration than in the calm water can occur during the water entry in waves.

The effect of the waves on slamming problems were further examined by studying following five factors, the wave length, the wave height, the wave heading, the entry location and the entry velocity. The study was focused on how these parameters affect the slamming forces and the pressure distribution on a wedge section. As a result, the wave length has significant effects on the slamming forces and pressures. The horizontal slamming force can change directions in the short wave length case. The slamming forces are insensitive to the wave height, but very sensitive to the entry location. Due to the variation of the local fluid velocities on the wave surface, the pressure distribution on the falling object is significantly affected. Greater local pressure can occur due to different wave phase angles. The horizontal slamming force is also sensitive to the entry velocity. Higher entry velocity leads to lower horizontal slamming coefficient however higher horizontal slamming force. The vertical slamming force coefficient is insensitive to the entry velocity. The results show that the presence of waves can result in greater local pressure concentrations and an additional horizontal force.

The novel contributions of this research are summarized as below:

1. Three different interface capturing schemes coupled with the CIP-based flow solver were examined for slamming problems. The THINC schemes were found more stable and accurate for the prediction of pressure/force and the capture of free surfaces.

2. The free fall of various 3-D rigid bodies into calm water was studied. The 6-DOF motion solver was developed and validated.

3. Water impact in waves was investigated by applying the improved CIP-based

method. Studies show that waves can lead to asymmetrical and increased slamming pressure in comparison with slamming in calm water. Studies also suggest that model tests should be carried out to validate the numerical method.

6.2 Future Work

The following aspects need to be addressed in future work.

1. The computing efficiency needs to be improved for slamming in waves. In the present studies, a constant time step was used to simulate waves and the slamming, with a focus on the slamming phenomenon. However, this led to a very long computing time to generate waves, since the number of grids is large and the time step is small. In order to improve the efficiency, a hybrid method may be developed. Since slamming usually occurs in a short period of time, the flows in the far field are not disturbed. The CIP-based method can be coupled with a potential flow based method to solve the slamming problem in waves. The highly nonlinear free surface flow in the near field can be tackled by the CIP-based method and the incoming waves and the far field flow can be solved based on the potential flow theory. Other methods, such as the use of fine grid in slamming zone and coarse grid in far field, longer time step for wave generation and smaller time step for slamming, should be investigated.

2. Model tests should be carried out for slamming in waves to validate the improved numerical method.

3. Slamming in irregular waves should be further studied. Since ships operating

in irregular waves encounter slamming continuously, the characteristics of the slamming phenomenon need to be understood.

4. Cavities should be further investigated. As shown in the simulations of ship sections, cavities occur during slamming. The effect of cavities on slamming needs to be understood for real ships.

Bibliography

[1] S. Abrate. Hull slamming. *Applied Mechanics Reviews*, 64(6), 2013.

[2] A. E. M. Alaoui and A. Nême. Slamming load during vertical water entry at constant velocity. In *ISOPE2012*, Rhodes, Greece, 2012.

[3] R. Baarholm and O. M. Faltinsen. Wave impact underneath horizontal decks. *Journal of Marine Science and Technology*, 9(1):1–13, 2004.

[4] C. M. Bao, G. X. Wu, and G. Xu. Simulation of freefall water entry of a finite wedge with flow detachment. *Applied Ocean Research*, 65:262–278, 2017.

[5] M. Barjasteh, H. Zeraatgar, and M. J. Javaherian. An experimental study on water entry of asymmetric wedges. *Applied Ocean Research*, 58:292–304, 2016.

[6] A. Carcaterra and E. Ciappi. Hydrodynamic shock of elastic structures impacting on the water: theory and experiments. *Journal of Sound and Vibration*, 271(1-2):411–439, 2004.

[7] I. Celik, U. Ghia, P. Roache, C. Freitas, H. Coleman, and P. Raad. Procedure for estimation and reporting of uncertainty due to discretization in CFD applications. *Journal of Fluids Engineering*, 130(7):078001, 2008.

[8] H.-J. Chae and B.-S. Yoon. Lagrangian approach to the wedge entry problem using SPH numerical methods. In *ISOPE2016*, Rhodes, Greece, 2016.

[9] J. Chuang, W. Zhu, and W. Qiu. Numerical solutions of 2-D water entry problem. In *ISOPE2006*, San Francisco, California, USA, 2006.

[10] S.-L. Chuang. Slamming of rigid wedge-shaped bodies with various deadrise angles. Technical report, David Taylor Model Basin, 1966.

[11] S.-L. Chuang and D. T. Milne. Drop tests of cones to investigate the three-dimensional effects of slamming. Technical report, Naval Ship Research and Development Center, 1971.

[12] R. Cointe and J. L. Armand. Hydrodynamic impact analysis of a cylinder. *Journal of Offshore Mechanics and Arctic Engineering*, 109(3):237, 1987.

[13] M. R. Davis and J. R. Whelan. Computation of wet deck bow slam loads for catamaran arched cross sections. *Ocean Engineering*, 34(17-18):2265–2276, 2007.

[14] R. G. Dean and R. A. Dalrymple. *Water Wave Mechanics for Engineers and Scientists*. Prentice-Hall, Inc., Englewood Cliffs, New Jersey, 1984.

[15] A. Engle and R. Lewis. A comparison of hydrodynamic impacts prediction methods with two dimensional drop test data. *Marine Structures*, 16(2):175–182, 2003.

[16] O. M. Faltinsen. The effect of hydroelasticity on ship slamming. *Philos. Trans. R. Soc.Lond. A*, 355:575–591, 1997.

[17] O. M. Faltinsen and M. Chezhian. A generalized Wagner method for three-dimensional slamming. *Journal of Ship Research*, 49(4):279–287, 2005.

[18] R. A. Gingold and J. J. Monaghan. Smoothed particle hydrodynamics: theory and application to non-spherical stars. *Monthly Notices of the Royal Astronomical Society*, 181(3):375–389, 1977.

[19] K. Gong, H. Liu, and B. L. Wang. Water entry of a wedge based on SPH model with an improved boundary treatment. *Journal of Hydrodynamics*, 21(6):750–757, 2009.

[20] M. Greenhow. Wedge entry into initially calm water. *Applied Ocean Research*, 9(4):214–223, 1987.

[21] M. Greenhow. Water-entry and -exit of a horizontal circular cylinder. *Applied Ocean Research*, 10(4):191–198, 1988.

[22] M. Greenhow and W.-M. Lin. Nonlinear free surface effects: Experiments and theory. Technical report, Dept. Ocean Engineering, MIT, 1983. Wedge, circular cylinder, freesurface, no entry V.

[23] H. B. Gu, L. Qian, D. M. Causon, C. G. Mingham, and P. Lin. Numerical simulation of water impact of solid bodies with vertical and oblique entries. *Ocean Engineering*, 75:128–137, 2014.

[24] O. A. Hermundstad and T. Moan. Numerical and experimental analysis of bow flare slamming on a RoRo vessel in regular oblique waves. *Journal of Marine Science and Technology*, 10(3):105–122, 2005.

[25] C. W. Hirt and B. D. Nichols. Volume of fluid (vof) method for the dynamics of free boundaries. *Journal of Computational Physics*, 39(1):201–225, 1981.

[26] S. Y. Hong, K.-H. Kim, and S. C. Hwang. Comparative study of water-impact problem for ship section and wedge drops. *International Journal of Offshore and Polar Engineering*, 27(2):123–134, 2017.

[27] S. Y. Hong, K.-H. Kim, B. W. Kim, and Y.-S. Kim. Experimental study on the bow-flare slamming of a 10,000 teu containership. In *ISOPE2014*, Busan, Korea, 2014.

[28] S.-Y. Hong, Y.-S. Kim, J.-H. Kyoung, S.-W. Hong, and Y.-H. Kim. Experimental study on impact loads acting on free-falling modified Wigley. *International Journal of Ocean System Engineering*, 2(3):151–159, 2012.

[29] S. D. Howison, J. R. Ockendon, and S. K. Wilson. Incompressible water-entry problems at small deadrise angles. *Journal of Fluid Mechanics*, 222:215–230, 1991.

[30] C. Hu and M. Kashiwagi. A CIP-based method for numerical simulations of violent free-surface flows. *Journal of Marine Science and Technology*, 9(4):143–157, 2004.

[31] C. Hu and M. Kashiwagi. Two-dimensional numerical simulation and experiment on strongly nonlinear wavebody interactions. *Journal of Marine Science and Technology*, 14(2):200–213, 2008.

[32] X.-z. Hu and S.-j. Liu. Numerical investigation of water-entry of flatted-bottom seafloor mining tool in ocean waves. *Journal of Central South University*, 21(8):3071–3078, 2014.

[33] Z. Hu, X. Zhao, C. Du, and D. Zhang. Numerical simulation of water entry of twin wedges using a CIP-based method. In *ISOPE2017*, San Francisco, USA, 2017.

[34] F. J. Huera-Huarte, D. Jeon, and M. Gharib. Experimental investigation of water slamming loads on panels. *Ocean Engineering*, 38(11-12):1347–1355, 2011.

[35] A. Iranmanesh and M. Passandideh-Fard. A three-dimensional numerical approach on water entry of a horizontal circular cylinder using the volume of fluid technique. *Ocean Engineering*, 130:557–566, 2017.

[36] A. Kamath, H. Bihs, and Ø. A. Arntsen. Study of water impact and entry of a free falling wedge using computational fluid dynamics simulations. 139, 2017.

[37] K.-H. Kim, B. W. Kim, S. Y. Hong, and Y.-S. Kim. Characteristics of stern slamming loads on an ultra-large containership in regular and irregular waves. In *ISOPE2015*, Hawaii, USA, 2015.

[38] K.-H. Kim, D. Y. Lee, S. Y. Hong, B. W. Kim, Y.-S. Kim, and B. W. Nam. Experimental study on the water impact load on symmetric and asymmetric wedges. In *ISOPE2014*, Busan, Korea, 2014.

[39] Y. Kim, Y. Kim, Y. Liu, and D. Yue. On the water entry impact problem of asymmetric bodies. In *9th International Conference on Numerical Ship Hydrodynamics*, 2007.

[40] Y. Kim, K.-K. Yang, J.-H. Kim, and Z. Zhu. Study of water-entry impact of wedge and ship-like section using potential theories and CFD. *International Journal of Offshore and Polar Engineering*, 27(2):168–176, 2017.

[41] K. M. T. Kleefsman, G. Fekken, A. E. P. Veldman, B. Iwanowski, and B. Buchner. A Volume-of-Fluid based simulation method for wave impact problems. *Journal of Computational Physics*, 206(1):363–393, 2005.

[42] A. A. Korobkin and V. V. Pukhnachov. Initial stage of water impact. *Annual Review of Fluid Mechanics*, 20:159–185, 1988.

[43] X. Li, C. Hu, and D. L. Touze. Water entry simulation by a lattice Boltzmann method. In *IWWWFB*, 2017.

[44] M.-C. Lin and L.-D. Shieh. Simultaneous measurements of water impact on a two-dimensional body. *Fluid Dynamics Research*, 19:125–148, 1997.

[45] L. Ma and H. Liu. Numerical study on wedge water entry problems using two-phase SPH method. In *ISOPE2016*, Rhodes, Greece, 2016.

[46] L. Ma and H. Liu. Numerical study of 2-D vertical water-entry problems using two-phase SPH method. *International Journal of Offshore and Polar Engineering*, 27(2):160–167, 2017.

[47] Z. Ma, L. Qian, P. M. Ferrer, D. Causon, and C. Mingham. Numerical simulation of water entry of 2D wedges. In *ISOPE2016*, Rhodes, Greece, 2016.

[48] X. M. Mei, Y. M. Liu, and D. K. P. Yue. On the water impact of general two-dimensional sections. *Applied Ocean Research*, 21(1):1–15, 1999.

[49] C. Monroy, S. Seng, L. Diebold, A. Benhamou, and . Malenica. A comparative study of the generalized wagner model and a free-surface RANS solver for water entry problems. *International Journal of Offshore and Polar Engineering*, 27(2):135–143, 2017.

[50] K. Ochi. Model experiments on ship strength and slamming in regular waves. *Transactions of the Society of Naval Architects and Marine Engineers*, 66:345–383, 1958.

[51] G. Oger, M. Doring, B. Alessandrini, and P. Ferrant. Two-dimensional SPH simulations of wedge water entries. *Journal of Computational Physics*, 213(2):803–822, 2006.

[52] J. M. Oliver. Second-order wagner theory for two-dimensional water-entry problems at small deadrise angles. *Journal of Fluid Mechanics*, 572:59–85, 2007.

[53] S. Osher and J. A. Sethian. Fronts propagating with curvature dependent speed: Algorithms based on hamilton-jacobi formulations. *Journal of Computational Physics*, 79:12–49, 1988.

[54] R. Panciroli, S. Abrate, and G. Minak. Dynamic response of flexible wedges entering the water. *Composite Structures*, 99:163–171, 2013.

[55] R. Panciroli, S. Abrate, G. Minak, and A. Zucchelli. Hydroelasticity in water-entry problems: Comparison between experimental and SPH results. *Composite Structures*, 94(2):532–539, 2012.

[56] R. Panciroli and M. Porfiri. Analysis of hydroelastic slamming through particle image velocimetry. *Journal of Sound and Vibration*, 347:63–78, 2015.

[57] R. Panciroli, A. Shams, and M. Porfiri. Experiments on the water entry of curved wedges: High speed imaging and particle image velocimetry. *Ocean Engineering*, 94:213–222, 2015.

[58] S. Peng, W. Wu, H. Sun, J. Pan, and Z. Xia. Experimental study and numerical simulation on slamming of trimaran. In *ISOPE2011*, Maui, Hawaii, USA, 2011.

[59] B. Peseux, L. Gornet, and B. Donguy. Hydrodynamic impact: Numerical and experimental investigations. *Journal of Fluids and Structures*, 21(3):277–303, 2005.

[60] D. Ren, J.-C. Park, S.-M. Yun, and H.-S. Shin. Particle simulation on a free fall slamming problem for 2-D wedge and ship section. In *ISOPE2016*, Rhodes, Greece, 2016.

[61] A. Shams, M. Jalalisendi, and M. Porfiri. Experiments on the water entry of asymmetric wedges using particle image velocimetry. *Physics of Fluids*, 27(2):027103, 2015.

[62] A. Shams, S. Zhao, and M. Porfiri. Hydroelastic slamming of flexible wedges: Modeling and experiments from water entry to exit. *Physics of Fluids*, 29(3):037107, 2017.

[63] M. Shiffman and D. C. Spencer. The force of impact on a cone striking a water surface (vertical entry). *Communications on Pure and Applied Mathematics*, 4:379–417, 1951.

[64] I. Stenius, A. Rosn, M. Battley, and T. Allen. Experimental hydroelastic characterization of slamming loaded marine panels. *Ocean Engineering*, 74:1–15, 2013.

[65] H. Sun and O. M. Faltinsen. Water impact of horizontal circular cylinders and cylindrical shells. *Applied Ocean Research*, 28(5):299–311, 2006.

[66] S. L. Sun and G. X. Wu. Oblique water entry of a cone by a fully three-dimensional nonlinear method. *Journal of Fluids and Structures*, 42:313–332, 2013.

[67] S. Y. Sun, S. L. Sun, and G. X. Wu. Oblique water entry of a wedge into waves with gravity effect. *Journal of Fluids and Structures*, 52:49–64, 2015.

[68] A. Swidan, W. Amin, D. Ranmuthugala, G. Thomas, and I. Penesis. Numerical prediction of symmetric water impact loads on wedge shaped hull form using CFD. *World Journal of Mechanics*, 03(08):311–318, 2013.

[69] H. Takewaki, A. Nishiguchi, and T. Yabe. Cubic interpolated pseudo-particle method (cip) for solving hyperbolic-type equations. *Journal of Computational Physics*, 61(2):261–268, 1985.

[70] X.-m. Tian, Z.-j. Zou, F.-h. Wang, and H.-l. Ren. Experimental investigations on slamming impacts by drop tests. In *ISOPE2014*, Busan, Korea, 2014.

[71] A. Troesch and C.-G. Kang. Hydrodynamic impact loads on three-dimensional bodies. In *Symposium on Naval Hydrodynamics, 16th*, 1986.

[72] T. Tveitnes, A. C. Fairlie-Clarke, and K. Varyani. An experimental investigation into the constant velocity water entry of wedge-shaped sections. *Ocean Engineering*, 35(14-15):1463–1478, 2008.

[73] T. Utsumi, T. Kunugi, and T. Aoki. Stability and accuracy of the Cubic Interpolated Propagation scheme. *Computer Physics Communications*, 101:9–20, 1997.

[74] D. Van Nuffel, K. S. Vepa, I. De Baere, P. Lava, M. Kersemans, J. Degrieck, J. De Rouck, and W. Van Paepegem. A comparison between the experimental and theoretical impact pressures acting on a horizontal quasi-rigid cylinder during vertical water entry. *Ocean Engineering*, 77:42–54, 2014.

[75] D. Van Nuffel, S. Vepa, I. De Baere, J. Degrieck, J. De Rouck, and W. Van Paepegem. Experimental study on the impact loads acting on a horizontal rigid cylinder during vertical water entry. In *OMAE2012*, Rio de Janeiro, Brazil, 2012.

[76] J. H. G. Verhagen. The impact of a flat plate on a water surface. *Journal of Ship Research*, 1967.

[77] T. Vinje and P. Brevig. Nonlinear ship motions. In *3rd International Conference on Numeircal Ship Hydrodynamics*, pages 257–266, 1981.

[78] T. von Karman. The impact on seaplane floats during landing. Technical report, NACA, 1929.

[79] H. Wagner. Über stoss und gleitvorgänge an der oberfläche von flüssigkeiten. *Z. Angew. Math. Mech.*, 12(4):193–215, 1932.

[80] J. Wang and O. M. Faltinsen. Improved numerical solution of Dobrovol'skaya's boundary integral equations on similarity flow for uniform symmetrical entry of wedges. *Applied Ocean Research*, 66:23–31, 2017.

[81] J. Wang, C. Lugni, and O. M. Faltinsen. Experimental and numerical investigation of a freefall wedge vertically entering the water surface. *Applied Ocean Research*, 51:181–203, 2015.

[82] S. Wang and C. Guedes Soares. Numerical study on the water impact of 3D bodies by an explicit finite element method. *Ocean Engineering*, 78:73–88, 2014.

[83] S. Wang and C. Guedes Soares. Experimental and numerical study of the slamming load on the bow of a chemical tanker in irregular waves. *Ocean Engineering*, 111:369–383, 2016.

[84] S. Wang and C. Guedes Soares. Stern slamming of a chemical tanker in irregular head waves. *Ocean Engineering*, 122:322–332, 2016.

[85] W.-h. Wang and Y.-y. Wang. An essential solution of water entry problems and its engineering applications. *Journal of Marine Science and Application*, 9(3):268–273, 2010.

[86] Z. Wei and C. Hu. An experimental study on water entry of horizontal cylinders. *Journal of Marine Science and Technology*, 19(3):338–350, 2014.

[87] Z. Wei and C. Hu. Experimental study on water entry of circular cylinders with inclined angles. *Journal of Marine Science and Technology*, 20(4):722–738, 2015.

[88] Z.-Y. Wei, H.-y. Xiao, Z.-d. Wang, and X.-H. Shi. Numerical simulation of water entry of wedges based on the CIP method. *Journal of Marine Science and Technology*, 23:142–150, 2015.

[89] P. Wen and W. Qiu. CIP and parallel computing based numerical solutions of 3-D slamming problems. In *ASME 2015 34th International Conference on Ocean, Offshore and Arctic Engineering*, volume 11, St. John's, Newfoundland, Canada, 2015.

[90] P. Wen and W. Qiu. Numerical solution of 2-D water entry problems based on a CIP method and a parallel computing algorithm. In *OMAE2015*, St. John's, Canada, 2015.

[91] P. Wen and W. Qiu. Numerical prediction of forces and pressures on wedge and ship sections based on a CIP method. In *Twenty-sixth (2016) International Ocean and Polar Engineering Conference*, Rhodes, Greece, 2016.

[92] P. Wen and W. Qiu. Solving 2-D water entry problems with a CIP method and a parallel computing algorithm. *Marine Systems and Ocean Technology*, 11:1–9, 2016.

[93] G. X. Wu. Numerical simulation of water entry of twin wedges. *Journal of Fluids and Structures*, 22(1):99–108, 2006.

[94] G. X. Wu, H. Sun, and Y. S. He. Numerical simulation and experimental study of water entry of a wedge in free fall motion. *Journal of Fluids and Structures*, 19(3):277–289, 2004.

[95] F. Xiao, Y. Honma, and T. Kono. A simple algebraic interface capturing scheme using hyperbolic tangent function. *International J. Numer. Meth. Fluids*, 48:1023–1040, 2005.

[96] G. Xu and G. Wu. Oblique water entry of a wedge with vortex shedding. In *IWWWFB*, 2015.

[97] G. D. Xu, W. Y. Duan, and G. X. Wu. Numerical simulation of oblique water entry of an asymmetrical wedge. *Ocean Engineering*, 35(16):1597–1603, 2008.

[98] T. Yabe. A universal cubic interpolation solver for compressible and incompressible fluids. *Stock Waves*, 1:187–195, 1991.

[99] T. Yabe. A universal solver for hyperbolic equations by cubic-polynomial interpolation I. one-dimensional solver. *Computer Physics Communications*, 66(2-3):219–232, 1991.

[100] T. Yabe, T. Ishikawa, and P. Wang. A universal solver for hyperbolic equations by cubic-polynomial interpolation II. two- and three-dimensional solvers. *Computer Physics Communications*, 66(2-3):233–242, 1991.

[101] T. Yabe, F. Xiao, and T. Utsumi. The constrained interpolation profile method for multiphase analysis. *Journal of Computational Physics*, 169(2):556–593, 2001.

[102] L. Yang, H. Yang, S. Yan, and Q. Ma. Numerical investigation of water-entry problems using IBM method. *International Journal of Offshore and Polar Engineering*, 27(2):152–159, 2017.

[103] L. Yang, H. Yang, S. Yan, Q. Ma, and M. Bihnam. Comparative study on water impact problem. In *ISOPE2016*, Rhodes, Greece, 2016.

[104] Q. Yang and W. Qiu. Numerical simulation of water impact for 2-D and 3-D bodies. *Ocean Engineering*, 43:82–89, 2012.

[105] Q. Yang and W. Qiu. Numerical solution of 3-D water entry problems with a constrained interpolation profile method. *J. Offshore Mech. Arct. Eng*, 134(4), 2012.

[106] E. M. Yettou, A. Desrochers, and Y. Champoux. Experimental study on the water impact of a symmetrical wedge. *Fluid Dynamics Research*, 38(1):47–66, 2006.

[107] K. Yokoi. Efficient implementation of THINC scheme: A simple and practical smoothed VOF algorithm. *Journal of Computational Physics*, 226(2):1985–2002, 2007.

[108] R. Zha, H. Peng, and W. Qiu. Solving 2D coupled water entry problem by an improved MPS method. In *IWWWFB*, 2017.

[109] Y. Zhang, A. Mohtat, and S. C. Yim. Effect of compressibility on peak impact pressure and pressure distribution during water entry of a wedge. In *OMAE2015*, St. John's, Newfoundland, Canada, 2015.

[110] R. Zhao and O. Faltinsen. Water entry of two-dimensional bodies. *Journal of Fluid Mechanics*, 246:593–612, 1993.

[111] R. Zhao, O. Faltinsen, and J. Aarsnes. Water entry of arbitrary two dimensional sections with and without flow separation. In *Symp. on Naval Hydrodynamics*, 1996.

[112] X. Zhu, O. M. Faltinsen, and C. Hu. Water entry and exit of a horizontal circular cylinder. *Journal of Offshore Mechanics and Arctic Engineering*, 129(4):253–264.

Appendix A

CIP Method

A.1 Principle of CIP Method

The classic upwind difference method for the advection term of the Navier-Stokes equations usually introduces numerical diffusion and associated inaccuracies. In the present work, the advection equations, Eqs. (2.4) to (2.6), are solved by the CIP method to reduce the numerical diffusion.

The CIP method, originally developed by Takewaki et al. [69], Yabe [98] [99] and Yabe et al. [100] [101], is a high order upwind scheme for solving the advection equation. It uses both the advection function of the profile and its spatial derivatives to construct an interpolation function of the profile within each grid cell. It can achieve sub-cell resolution while retaining the sharpness of the profile. The one-dimensional advection of a variable χ is governed by the following equation:

$$\frac{\partial \chi(x,t)}{\partial t} + u\frac{\partial \chi(x,t)}{\partial x} = 0 \tag{A.1}$$

where u is the advection velocity.

The CIP method not only considers the transportation of the profile of the variable χ, but also its spatial gradients $\varphi = \partial\chi/\partial x$. By differentiating Eq. (A.1), the advection equation of φ can be obtained with a similar form.

$$\frac{\partial\varphi}{\partial t} + u\frac{\partial\varphi}{\partial x} = -\varphi\frac{\partial u}{\partial x} \tag{A.2}$$

The computation of Eq. (A.2) is split into two steps, an advection phase and a nonadvection phase. The nonadvection phase is computed using finite difference method. The advection calculations of Eqs. (A.1) and (A.2) are achieved by a semi-Lagrangian procedure:

$$\chi^*(x) = \hat{\chi}^n(x - u\Delta t) \tag{A.3}$$

$$\varphi^*(x) = \hat{\varphi}^n(x - u\Delta t) \tag{A.4}$$

where $\hat{\chi}^n$ is an interpolation approximation to χ^n from the previous time step at the upwind cell, and $\hat{\varphi}^n = \partial\hat{\chi}^n/\partial x$. Fig. A.1 demonstrates the procedure of the CIP method.

The interpolation function $\hat{\chi}^n$ is constructed for each computational cells based on a cubic polynomial. For $u > 0$, the approximation for $\chi(x)$ in the upwind cell of grid x_i can be expressed using cubic interpolation as:

$$\hat{\chi}(x) = a_i(x - x_i)^3 + b_i(x - x_i)^2 + c_i(x - x_i) + d_i \quad (x_{i-1} < x < x_i) \tag{A.5}$$

The coefficients of the polynomial are determined from the known quantities χ_i^n, χ_{i-1}^n,

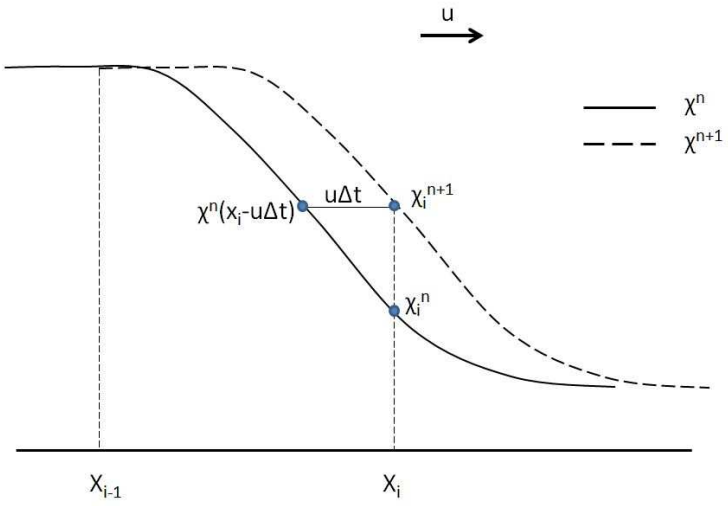

Figure A.1: Illustration of CIP method

φ_i^n and φ_{i-1}^n.

$$a_i = \frac{\varphi_i^n + \varphi_{i-1}^n}{\Delta x^2} - \frac{2(\chi_i^n - \chi_{i-1}^n)}{\Delta x^3} \tag{A.6}$$

$$b_i = \frac{(2\varphi_i^n + \varphi_{i-1}^n)}{\Delta x} - \frac{3(\chi_i^n - \chi_{i-1}^n)}{\Delta x^2} \tag{A.7}$$

$$c_i = \varphi_i^n \tag{A.8}$$

$$d_i = \chi_i^n \tag{A.9}$$

If $u < 0$, the coefficients are determined by using values on the upwind grids, χ_i^n, χ_{i+1}^n, φ_i^n and φ_{i+1}^n.

In summary, the CIP method has the following advantages:

1. Compact high order scheme. The cubic polynomial interpolation can be constructed by using the profile and its spatial derivatives.

2. Sub-cell resolution. The profile inside each cell is determined. It can achieve certain computational accuracy.

The formulation of the multi-dimensional CIP method is introduced in the next section.

A.2 Multi-dimensional CIP Formulation

A.2.1 Two-dimensional CIP Method

Following the same procedures in the one-dimensional formulation, the two-dimensional advection equations for a variable, $\chi(x,z,t)$, and its spatial derivatives, $\varphi_x(x,z,t)$ and $\varphi_z(x,z,t)$, can be written as:

$$\frac{\partial \chi(x,z,t)}{\partial t} + u\frac{\partial \chi(x,z,t)}{\partial x} + w\frac{\partial \chi(x,z,t)}{\partial z} = 0 \tag{A.10}$$

$$\frac{\partial \varphi_x(x,z,t)}{\partial t} + u\frac{\partial \varphi_x(x,z,t)}{\partial x} + w\frac{\partial \varphi_x(x,z,t)}{\partial z} = 0 \tag{A.11}$$

$$\frac{\partial \varphi_z(x,z,t)}{\partial t} + u\frac{\partial \varphi_z(x,z,t)}{\partial x} + w\frac{\partial \varphi_z(x,z,t)}{\partial z} = 0 \tag{A.12}$$

The following cubic polynomials are used for constructing the interpolation function in the upwind cell of grid point (x_i, z_k).

$$\begin{aligned}\hat{\chi}(x,z) = &\left\{\left[A_1 \times (x-x_i) + A_2 \times (z-z_k) + A_3\right](x-x_i) + A_4 \times (z-z_k) + \varphi^n_{x,i,k}\right\} \\ &(x-x_i) + \left\{\left[A_5 \times (z-z_k) + A_6 \times (x-x_i) + A_7\right](x-x_i) + \varphi^n_{z,i,k}\right\}(z-z_k) \\ &+ \chi^n_{i,k}\end{aligned} \tag{A.13}$$

The coefficients can be calculated by:

$$A_1 = \left[\left(\varphi^n_{x,is,k} + \varphi^n_{x,i,k}\right) \times X1 - 2(\chi^n_{i,k} - \chi^n_{is,k})\right] / X1^3 \tag{A.14}$$

$$A_2 = \left[-A_8 - (\varphi^n_{x,i,ks} - \varphi^n_{x,i,k}) \times X1\right] / (X1^2 \times Z1) \tag{A.15}$$

$$A_3 = \left[3\left(\chi^n_{is,k} - \chi^n_{i,k}\right) + \left(\varphi^n_{x,is,k} + 2\varphi^n_{x,i,k}\right) \times X1\right] / X1^2 \tag{A.16}$$

$$A_4 = \left[A_2 \times X1^2 - \left(\varphi^n_{z,is,k} - \varphi^n_{z,i,k}\right)\right] / X1 \tag{A.17}$$

$$A_5 = \left[\left(\varphi^n_{z,i,ks} + \varphi^n_{z,i,k}\right) \times Z1 - 2(\chi^n_{i,k} - \chi^n_{i,ks})\right] / Z1^3 \tag{A.18}$$

$$A_6 = \left[-A_8 - (\varphi^n_{z,is,k} - \varphi^n_{z,i,k}) \times Z1\right] / (X1 \times Z1^2) \tag{A.19}$$

$$A_7 = \left[3\left(\chi^n_{i,ks} - \chi^n_{i,k}\right) + \left(\varphi^n_{z,i,ks} + 2\varphi^n_{z,i,k}\right) \times Z1\right] / Z1^2 \tag{A.20}$$

where $X1 = sign(u) \times \Delta x$, $Z1 = sign(w) \times \Delta z$, $is = i - sign(u)$, $ks = k - sign(w)$ and $A_8 = \chi^n_{i,k} - \chi^n_{is,k} - \chi^n_{i,ks} + \chi^n_{is,ks}$.

A.2.2 Three-dimensional CIP Method

The general form of the three-dimensional advection equations can be written as:

$$\frac{\partial \chi(x,y,z,t)}{\partial t} + u\frac{\partial \chi(x,y,z,t)}{\partial x} + v\frac{\partial \chi(x,y,z,t)}{\partial y} + w\frac{\partial \chi(x,y,z,t)}{\partial z} = 0 \tag{A.21}$$

$$\frac{\partial \varphi_x(x,y,z,t)}{\partial t} + u\frac{\partial \varphi_x(x,y,z,t)}{\partial x} + v\frac{\partial \varphi_x(x,y,z,t)}{\partial y} + w\frac{\partial \varphi_x(x,y,z,t)}{\partial z} = 0 \tag{A.22}$$

$$\frac{\partial \varphi_y(x,y,z,t)}{\partial t} + u\frac{\partial \varphi_y(x,y,z,t)}{\partial x} + v\frac{\partial \varphi_y(x,y,z,t)}{\partial y} + w\frac{\partial \varphi_y(x,y,z,t)}{\partial z} = 0 \tag{A.23}$$

$$\frac{\partial \varphi_z(x,y,z,t)}{\partial t} + u\frac{\partial \varphi_z(x,y,z,t)}{\partial x} + v\frac{\partial \varphi_z(x,y,z,t)}{\partial y} + w\frac{\partial \varphi_z(x,y,z,t)}{\partial z} = 0 \tag{A.24}$$

The interpolation function in the upwind cell of grid point (x_i, y_j, z_k) is:

$$\begin{aligned}
\hat{\chi}(x,y,z) =& \{[A_1 \times (x-x_i) + A_4 \times (y-y_j) + A_7 \times (z-z_k) + A_{11}](x-x_i) \\
&+ A_{14} \times (y-y_j) + \varphi^n_{x,i,j,k}\}(x-x_i) \\
&\{[A_5 \times (x-x_i) + A_2 \times (y-y_j) + A_8 \times (z-z_k) + A_{12}](y-y_j) \\
&+ A_{15} \times (z-z_k) + \varphi^n_{y,i,j,k}\}(y-y_j) \\
&\{[A_6 \times (x-x_i) + A_9 \times (y-y_j) + A_3 \times (z-z_k) + A_{13}](z-z_k) \\
&+ A_{16} \times (x-x_i) + \varphi^n_{z,i,j,k}\}(z-z_k) \\
&+ A_{10} \times (x-x_i) \times (y-y_j) \times (z-z_k) + \chi^n_{i,j,k}
\end{aligned} \tag{A.25}$$

The coefficients can be calculated by:

$$A_1 = \left[\left(\varphi^n_{x,is,j,k} + \varphi^n_{x,i,j,k}\right) \times X1 + 2(\chi^n_{i,j,k} - \chi^n_{is,j,k})\right] / X1^3 \quad \text{(A.26)}$$

$$A_2 = \left[\left(\varphi^n_{y,i,js,k} + \varphi^n_{y,i,j,k}\right) \times Y1 + 2(\chi^n_{i,j,k} - \chi^n_{i,js,k})\right] / Y1^3 \quad \text{(A.27)}$$

$$A_3 = \left[\left(\varphi^n_{z,i,j,ks} + \varphi^n_{z,i,j,k}\right) \times Z1 + 2(\chi^n_{i,j,k} - \chi^n_{i,j,ks})\right] / Z1^3 \quad \text{(A.28)}$$

$$B_1 = \chi^n_{i,j,k} - \chi^n_{is,j,k} - \chi^n_{i,js,k} + \chi^n_{is,js,k} \quad \text{(A.29)}$$

$$B_2 = \chi^n_{i,j,k} - \chi^n_{i,j,ks} - \chi^n_{i,js,k} + \chi^n_{i,js,ks} \quad \text{(A.30)}$$

$$B_3 = \chi^n_{i,j,k} - \chi^n_{is,j,k} - \chi^n_{i,j,ks} + \chi^n_{is,j,ks} \quad \text{(A.31)}$$

$$A_4 = \left[B_1 - (\varphi^n_{x,i,js,k} - \varphi^n_{x,i,j,k}) \times X1\right] / (X1^2 \times Y1) \quad \text{(A.32)}$$

$$A_5 = \left[B_1 - (\varphi^n_{y,is,j,k} - \varphi^n_{y,i,j,k}) \times Y1\right] / (X1 \times Y1^2) \quad \text{(A.33)}$$

$$A_6 = \left[B_3 - (\varphi^n_{z,is,j,k} - \varphi^n_{z,i,j,k}) \times Z1\right] / (X1 \times Z1^2) \quad \text{(A.34)}$$

$$A_7 = \left[B_3 - (\varphi^n_{x,i,j,ks} - \varphi^n_{x,i,j,k}) \times X1\right] / (X1^2 \times Z1) \quad \text{(A.35)}$$

$$A_8 = \left[B_2 - (\varphi^n_{y,i,j,ks} - \varphi^n_{y,i,j,k}) \times Y1\right] / (Z1 \times Y1^2) \quad \text{(A.36)}$$

$$A_9 = \left[B_2 - (\varphi^n_{z,i,js,k} - \varphi^n_{z,i,j,k}) \times Z1\right] / (Y1 \times Z1^2) \quad \text{(A.37)}$$

$$A_{10} = [-\chi^n_{i,j,k} + (\chi^n_{is,j,k} + \chi^n_{i,js,k} + \chi^n_{i,j,ks}) - (\chi^n_{is,js,k} + \chi^n_{i,js,ks} + \chi^n_{is,j,ks}) \quad \text{(A.38)}$$

$$+\chi^n_{is,js,ks}]/(X1 \times Y1 \times Z1) \quad \text{(A.39)}$$

$$A_{11} = \left[3\left(\chi^n_{is,j,k} - \chi^n_{i,j,k}\right) - \left(\varphi^n_{x,is,j,k} + 2\varphi^n_{x,i,j,k}\right) \times X1\right] / X1^2 \quad \text{(A.40)}$$

$$A_{12} = \left[3\left(\chi^n_{i,js,k} - \chi^n_{i,j,k}\right) - \left(\varphi^n_{y,i,js,k} + 2\varphi^n_{y,i,j,k}\right) \times Y1\right] / Y1^2 \quad \text{(A.41)}$$

$$A_{13} = \left[3\left(\chi^n_{i,j,ks} - \chi^n_{i,j,k}\right) - \left(\varphi^n_{z,i,j,ks} + 2\varphi^n_{z,i,j,k}\right) \times Z1\right] / Z1^2 \quad \text{(A.42)}$$

where $X1 = sign(u) \times \Delta x$, $Y1 = sign(v) \times \Delta y$, $Z1 = sign(w) \times \Delta z$, $is = i - sign(u)$, $js = j - sign(v)$ and $ks = k - sign(w)$.

Appendix B

Biconjugate Gradient Stabilized Method

The biconjugate gradient stabilized method, or abbreviated as BiCGSTAB, is an iterative method for the numerical solution of non-symmetric linear systems. To solve a linear system $[A]\,\mathbf{x} = \mathbf{b}$, the BiCGSTAB starts with an initial guess $\mathbf{x}_0$ and proceeds with the following algorithmic steps:

1. $\mathbf{r}_0 = \mathbf{b} - [A]\,\mathbf{x}_0$
2. Choose an arbitrary vector $\hat{\mathbf{r}}_0$ which satisfies $\hat{\mathbf{r}}_0 \cdot \mathbf{r}_0 \neq 0$. In this work, $\hat{\mathbf{r}}_0 = \mathbf{r}_0$.
3. $\rho_0 = \alpha = \omega_0 = 1$
4. $\mathbf{v}_0 = \mathbf{p}_0 = \mathbf{0}$
5. Do the following iterations ($i = 1, 2, 3, \ldots$) till a solution is found.
   (a) $\rho_i = \hat{\mathbf{r}}_0 \cdot \mathbf{r}_{i-1}$

(b) $\beta = \dfrac{\rho_i \alpha}{\rho_{i-1}\omega_{i-1}}$

(c) $\mathbf{p}_i = \mathbf{r}_{i-1} + \beta(\mathbf{p}_{i-1} - \omega_{i-1}\mathbf{v}_{i-1})$

(d) $\mathbf{v}_i = [A]\,\mathbf{p}_i$

(e) $\alpha = \dfrac{\rho_i}{\hat{\mathbf{r}}_0 \cdot \mathbf{v}_i}$

(f) $\mathbf{h} = \mathbf{x}_{i-1} + \alpha \mathbf{p}_i$

(g) If $\mathbf{h}$ is accurate enough, then $\mathbf{x} = \mathbf{h}$ and quit

(h) $\mathbf{s} = \mathbf{r}_{i-1} - \alpha \mathbf{v}_i$

(i) $\mathbf{t} = [A]\,\mathbf{s}$

(j) $\omega_i = \dfrac{\mathbf{t} \cdot \mathbf{s}}{\mathbf{t} \cdot \mathbf{t}}$

(k) $\mathbf{x}_i = \mathbf{h} + \omega_i \mathbf{s}$

(l) If $\mathbf{x}_i$ is accurate enough, then $\mathbf{x} = \mathbf{x}_i$ and quit

(m) $\mathbf{r}_i = \mathbf{s} - \omega_i \mathbf{t}$ and go to step (a)

The convergence rate depends on the condition number of the matrix $[A]$. Preconditioning of the system can reduce the condition number and improve the convergence rate. The system is changed to solve $[M]^{-1}[A]\,\mathbf{x} = [M]^{-1}\,\mathbf{b}$, where the eigenvalues of $[M]^{-1}[A]$ are better clustered than those of $[A]$. In this work, the simple Jacobi preconditioning is applied and $[M] = diag([A])$.

Appendix C

Spatial Derivatives

The spatial derivatives in the formulations of the present method are summarized below. Note that $(\partial u/\partial x)_{P\{i,j,k\}}$ denotes the derivative $\partial u/\partial x$ at the P node in the grid $\{i, j, k\}$.

$$(\partial u/\partial x)_{P\{i,j,k\}} = \frac{u_{U\{i,j,k\}} - u_{U\{i-1,j,k\}}}{x_{U\{i,j,k\}} - x_{U\{i-1,j,k\}}} \tag{C.1}$$

$$(\partial u/\partial x)_{U\{i,j,k\}} = \frac{u_{U\{i+1,j,k\}} - u_{U\{i-1,j,k\}}}{x_{U\{i+1,j,k\}} - x_{U\{i-1,j,k\}}} \tag{C.2}$$

$$(\partial u/\partial x)_{V\{i,j,k\}} = \frac{u_{U\{i,j,k\}} + u_{U\{i,j+1,k\}} - u_{U\{i-1,j,k\}} - u_{U\{i-1,j+1,k\}}}{2(x_{U\{i,j,k\}} - x_{U\{i-1,j,k\}})} \tag{C.3}$$

$$(\partial u/\partial x)_{W\{i,j,k\}} = \frac{u_{U\{i,j,k\}} + u_{U\{i,j,k+1\}} - u_{U\{i-1,j,k\}} - u_{U\{i-1,j,k+1\}}}{2(x_{U\{i,j,k\}} - x_{U\{i-1,j,k\}})} \tag{C.4}$$

$$(\partial u/\partial y)_{P\{i,j,k\}} = \frac{u_{U\{i,j+1,k\}} + u_{U\{i-1,j+1,k\}} - u_{U\{i,j-1,k\}} - u_{U\{i-1,j-1,k\}}}{2(y_{U\{i,j+1,k\}} - y_{U\{i,j-1,k\}})} \tag{C.5}$$

$$(\partial u/\partial y)_{U\{i,j,k\}} = \frac{u_{U\{i,j+1,k\}} - u_{U\{i,j-1,k\}}}{y_{U\{i,j+1,k\}} - y_{U\{i,j-1,k\}}} \tag{C.6}$$

$$(\partial u/\partial y)_{V\{i,j,k\}} = \frac{u_{U\{i,j+1,k\}} + u_{U\{i-1,j+1,k\}} - u_{U\{i,j,k\}} - u_{U\{i-1,j,k\}}}{2(y_{U\{i,j+1,k\}} - y_{U\{i,j,k\}})} \tag{C.7}$$

$$\begin{aligned}(\partial u/\partial y)_{W\{i,j,k\}} =&[(u_{U\{i,j+1,k\}} + u_{U\{i-1,j+1,k\}} + u_{U\{i,j+1,k+1\}} + u_{U\{i-1,j+1,k+1\}}) \\ &- (u_{U\{i,j-1,k\}} + u_{U\{i-1,j-1,k\}} + u_{U\{i,j-1,k+1\}} + u_{U\{i-1,j-1,k+1\}})] \\ &/[4(y_{U\{i,j+1,k\}} - y_{U\{i,j-1,k\}})]\end{aligned} \tag{C.8}$$

$$(\partial u/\partial z)_{P\{i,j,k\}} = \frac{u_{U\{i,j,k+1\}} + u_{U\{i-1,j,k+1\}} - u_{U\{i,j,k-1\}} - u_{U\{i-1,j,k-1\}}}{2(z_{U\{i,j,k+1\}} - z_{U\{i,j,k-1\}})} \tag{C.9}$$

$$(\partial u/\partial z)_{U\{i,j,k\}} = \frac{u_{U\{i,j,k+1\}} - u_{U\{i,j,k-1\}}}{z_{U\{i,j,k+1\}} - z_{U\{i,j,k-1\}}} \tag{C.10}$$

$$\begin{aligned}(\partial u/\partial z)_{V\{i,j,k\}} =&[(u_{U\{i,j,k+1\}} + u_{U\{i-1,j,k+1\}} + u_{U\{i,j+1,k+1\}} + u_{U\{i-1,j+1,k+1\}}) \\ &- (u_{U\{i,j,k-1\}} + u_{U\{i-1,j,k-1\}} + u_{U\{i,j+1,k-1\}} + u_{U\{i-1,j+1,k-1\}})] \\ &/[4(z_{U\{i,j,k+1\}} - z_{U\{i,j,k-1\}})]\end{aligned} \tag{C.11}$$

$$(\partial u/\partial z)_{W\{i,j,k\}} = \frac{u_{U\{i,j,k+1\}} + u_{U\{i-1,j,k+1\}} - u_{U\{i,j,k\}} - u_{U\{i-1,j,k\}}}{2(z_{U\{i,j,k+1\}} - z_{U\{i,j,k\}})} \tag{C.12}$$

$$(\partial v/\partial x)_{P\{i,j,k\}} = \frac{v_{V\{i+1,j,k\}} + v_{V\{i+1,j-1,k\}} - v_{V\{i-1,j,k\}} - v_{V\{i-1,j-1,k\}}}{2(x_{V\{i+1,j,k\}} - x_{V\{i-1,j,k\}})} \tag{C.13}$$

$$(\partial v/\partial x)_{U\{i,j,k\}} = \frac{v_{V\{i+1,j,k\}} + v_{V\{i+1,j-1,k\}} - v_{V\{i,j,k\}} - v_{V\{i,j-1,k\}}}{2(x_{V\{i+1,j,k\}} - x_{V\{i,j,k\}})} \tag{C.14}$$

$$(\partial v/\partial x)_{V\{i,j,k\}} = \frac{v_{V\{i+1,j,k\}} - v_{V\{i-1,j,k\}}}{x_{V\{i+1,j,k\}} - x_{V\{i-1,j,k\}}} \tag{C.15}$$

$$\begin{aligned}(\partial v/\partial x)_{W\{i,j,k\}} =&[(v_{V\{i+1,j,k\}} + v_{V\{i+1,j-1,k\}} + v_{V\{i+1,j,k+1\}} + v_{V\{i+1,j-1,k+1\}}) \\ &- (v_{V\{i-1,j,k\}} + v_{V\{i-1,j-1,k\}} + v_{V\{i-1,j,k+1\}} + v_{V\{i-1,j-1,k+1\}})] \\ &/[4(x_{V\{i+1,j,k\}} - x_{V\{i-1,j,k\}})]\end{aligned} \tag{C.16}$$

$$(\partial v/\partial y)_{P\{i,j,k\}} = \frac{v_{V\{i,j,k\}} - v_{V\{i,j-1,k\}}}{y_{V\{i,j,k\}} - y_{V\{i-1,j,k\}}} \tag{C.17}$$

$$(\partial v/\partial y)_{U\{i,j,k\}} = \frac{v_{V\{i,j,k\}} + v_{V\{i+1,j,k\}} - v_{V\{i,j-1,k\}} - v_{V\{i+1,j-1,k\}}}{2(y_{V\{i,j,k\}} - y_{V\{i,j-1,k\}})} \tag{C.18}$$

$$(\partial v/\partial y)_{V\{i,j,k\}} = \frac{v_{V\{i,j+1,k\}} - v_{V\{i,j-1,k\}}}{y_{V\{i,j+1,k\}} - y_{V\{i,j-1,k\}}} \tag{C.19}$$

$$(\partial v/\partial y)_{W\{i,j,k\}} = \frac{v_{V\{i,j,k\}} + v_{V\{i,j,k+1\}} - v_{V\{i,j-1,k\}} - v_{V\{i,j-1,k+1\}}}{2(y_{V\{i,j,k\}} - y_{V\{i,j-1,k\}})} \tag{C.20}$$

$$(\partial v/\partial z)_{P\{i,j,k\}} = \frac{v_{V\{i,j,k+1\}} + v_{V\{i,j-1,k+1\}} - v_{V\{i,j,k-1\}} - v_{V\{i,j-1,k-1\}}}{2(z_{V\{i,j,k+1\}} - z_{V\{i,j,k-1\}})} \tag{C.21}$$

$$\begin{aligned}(\partial v/\partial z)_{U\{i,j,k\}} =&[(v_{V\{i,j,k+1\}} + v_{V\{i,j-1,k+1\}} + v_{V\{i+1,j,k+1\}} + v_{V\{i+1,j-1,k+1\}}) \\ &- (v_{V\{i,j,k-1\}} + v_{V\{i,j-1,k-1\}} + v_{V\{i+1,j,k-1\}} + v_{V\{i+1,j-1,k-1\}})] \\ &/[4(z_{V\{i,j,k+1\}} - z_{V\{i,j,k-1\}})]\end{aligned} \tag{C.22}$$

$$(\partial v/\partial z)_{V\{i,j,k\}} = \frac{v_{V\{i,j,k+1\}} - v_{V\{i,j,k-1\}}}{z_{V\{i,j,k+1\}} - z_{V\{i,j,k-1\}}} \tag{C.23}$$

$$(\partial v/\partial z)_{W\{i,j,k\}} = \frac{v_{V\{i,j,k+1\}} + v_{V\{i,j-1,k+1\}} - v_{V\{i,j,k\}} - v_{V\{i,j-1,k\}}}{2(z_{V\{i,j,k+1\}} - z_{V\{i,j,k\}})} \tag{C.24}$$

$$(\partial w/\partial x)_{P\{i,j,k\}} = \frac{w_{W\{i+1,j,k\}} + w_{W\{i+1,j,k-1\}} - w_{W\{i-1,j,k\}} - w_{W\{i-1,j,k-1\}}}{2(x_{W\{i+1,j,k\}} - x_{W\{i-1,j,k\}})} \tag{C.25}$$

$$(\partial w/\partial x)_{U\{i,j,k\}} = \frac{w_{W\{i+1,j,k\}} + w_{W\{i+1,j,k-1\}} - w_{W\{i,j,k\}} - w_{W\{i,j,k-1\}}}{2(x_{W\{i+1,j,k\}} - x_{W\{i,j,k\}})} \tag{C.26}$$

$$\begin{aligned}(\partial w/\partial x)_{V\{i,j,k\}} =&[(w_{W\{i+1,j,k\}} + w_{W\{i+1,j,k-1\}} + w_{W\{i+1,j+1,k\}} + w_{W\{i+1,j+1,k-1\}}) \\ &- (w_{W\{i-1,j,k\}} + w_{W\{i-1,j,k-1\}} + w_{W\{i-1,j+1,k\}} + w_{W\{i-1,j+1,k-1\}})] \\ &/[4(x_{W\{i+1,j,k\}} - x_{W\{i-1,j,k\}})]\end{aligned} \tag{C.27}$$

$$(\partial w/\partial x)_{W\{i,j,k\}} = \frac{w_{W\{i+1,j,k\}} - w_{W\{i-1,j,k\}}}{x_{W\{i+1,j,k\}} - x_{W\{i-1,j,k\}}} \tag{C.28}$$

$$(\partial w/\partial y)_{P\{i,j,k\}} = \frac{w_{W\{i,j+1,k\}} + w_{W\{i,j+1,k-1\}} - w_{W\{i,j-1,k\}} - w_{W\{i,j-1,k-1\}}}{2(y_{W\{i,j+1,k\}} - y_{W\{i,j-1,k\}})} \tag{C.29}$$

$$\begin{aligned}(\partial w/\partial y)_{U\{i,j,k\}} =&[(w_{W\{i,j+1,k\}} + w_{W\{i,j+1,k-1\}} + w_{W\{i+1,j+1,k\}} + w_{W\{i+1,j+1,k-1\}}) \\ &- (w_{W\{i,j-1,k\}} + w_{W\{i,j-1,k-1\}} + w_{W\{i+1,j-1,k\}} + w_{W\{i+1,j-1,k-1\}})] \\ &/[4(y_{W\{i,j+1,k\}} - y_{W\{i,j-1,k\}})]\end{aligned} \tag{C.30}$$

$$(\partial w/\partial y)_{V\{i,j,k\}} = \frac{w_{W\{i,j+1,k\}} + w_{W\{i,j+1,k-1\}} - w_{W\{i,j,k\}} - w_{W\{i,j,k-1\}}}{2(y_{W\{i,j+1,k\}} - y_{W\{i,j,k\}})} \tag{C.31}$$

$$(\partial w/\partial y)_{W\{i,j,k\}} = \frac{w_{W\{i,j+1,k\}} - w_{W\{i,j-1,k\}}}{y_{W\{i,j+1,k\}} - y_{W\{i,j-1,k\}}} \tag{C.32}$$

$$(\partial w/\partial z)_{P\{i,j,k\}} = \frac{w_{W\{i,j,k\}} - w_{W\{i,j,k-1\}}}{z_{W\{i,j,k\}} - z_{W\{i,j,k-1\}}} \tag{C.33}$$

$$(\partial w/\partial z)_{U\{i,j,k\}} = \frac{w_{W\{i,j,k\}} + w_{W\{i+1,j,k\}} - w_{W\{i,j,k-1\}} - w_{W\{i+1,j,k-1\}}}{2(z_{W\{i,j,k\}} - z_{W\{i,j,k-1\}})} \tag{C.34}$$

$$(\partial w/\partial z)_{V\{i,j,k\}} = \frac{w_{W\{i,j,k\}} + w_{W\{i,j+1,k\}} - w_{W\{i,j,k-1\}} - w_{W\{i,j+1,k-1\}}}{2(z_{W\{i,j,k\}} - z_{W\{i,j,k-1\}})} \tag{C.35}$$

$$(\partial w/\partial z)_{W\{i,j,k\}} = \frac{w_{W\{i,j,k+1\}} - w_{W\{i,j,k-1\}}}{z_{W\{i,j,k+1\}} - z_{W\{i,j,k-1\}}} \tag{C.36}$$

$$(\partial p/\partial x)_{U\{i,j,k\}} = \frac{p_{P\{i+1,j,k\}} - p_{P\{i,j,k\}}}{(x_{P\{i+1,j,k\}} - x_{P\{i,j,k\}})} \tag{C.37}$$

$$(\partial p/\partial y)_{V\{i,j,k\}} = \frac{p_{P\{i,j+1,k\}} - p_{P\{i,j,k\}}}{(y_{P\{i,j+1,k\}} - y_{P\{i,j,k\}})} \tag{C.38}$$

$$(\partial p/\partial z)_{W\{i,j,k\}} = \frac{p_{P\{i,j,k+1\}} - p_{P\{i,j,k\}}}{(z_{P\{i,j,k+1\}} - z_{P\{i,j,k\}})} \tag{C.39}$$

$$\begin{aligned}(\partial^2 u/\partial x^2)_{U\{i,j,k\}} =& \frac{2u_{U\{i+1,j,k\}}}{(x_{U\{i+1,j,k\}} - x_{U\{i,j,k\}})(x_{U\{i+1,j,k\}} - x_{U\{i-1,j,k\}})} \\ &- \frac{2u_{U\{i,j,k\}}}{(x_{U\{i+1,j,k\}} - x_{U\{i,j,k\}})(x_{U\{i+1,j,k\}} - x_{U\{i-1,j,k\}})} \\ &- \frac{2u_{U\{i,j,k\}}}{(x_{U\{i,j,k\}} - x_{U\{i-1,j,k\}})(x_{U\{i+1,j,k\}} - x_{U\{i-1,j,k\}})} \\ &+ \frac{2u_{U\{i-1,j,k\}}}{(x_{U\{i,j,k\}} - x_{U\{i-1,j,k\}})(x_{U\{i+1,j,k\}} - x_{U\{i-1,j,k\}})}\end{aligned} \tag{C.40}$$

$$\begin{aligned}(\partial^2 u/\partial y^2)_{U\{i,j,k\}} =& \frac{2u_{U\{i,j+1,k\}}}{(y_{U\{i,j+1,k\}} - y_{U\{i,j,k\}})(y_{U\{i,j+1,k\}} - y_{U\{i,j-1,k\}})} \\ &- \frac{2u_{U\{i,j,k\}}}{(y_{U\{i,j+1,k\}} - y_{U\{i,j,k\}})(y_{U\{i,j+1,k\}} - y_{U\{i,j-1,k\}})} \\ &- \frac{2u_{U\{i,j,k\}}}{(y_{U\{i,j,k\}} - y_{U\{i,j-1,k\}})(y_{U\{i,j+1,k\}} - y_{U\{i,j-1,k\}})} \\ &+ \frac{2u_{U\{i,j-1,k\}}}{(y_{U\{i,j,k\}} - y_{U\{i,j-1,k\}})(y_{U\{i,j+1,k\}} - y_{U\{i,j-1,k\}})}\end{aligned} \tag{C.41}$$

$$
\begin{aligned}
(\partial^2 u/\partial z^2)_{U\{i,j,k\}} =& \frac{2u_{U\{i,j,k+1\}}}{(z_{U\{i,j,k+1\}} - z_{U\{i,j,k\}})(z_{U\{i,j,k+1\}} - z_{U\{i,j,k-1\}})} \\
&- \frac{2u_{U\{i,j,k\}}}{(x_{U\{i,j,k+1\}} - z_{U\{i,j,k\}})(z_{U\{i,j,k+1\}} - z_{U\{i,j,k-1\}})} \\
&- \frac{2u_{U\{i,j,k\}}}{(z_{U\{i,j,k\}} - z_{U\{i,j,k-1\}})(z_{U\{i,j,k+1\}} - z_{U\{i,j,k-1\}})} \\
&+ \frac{2u_{U\{i,j,k-1\}}}{(z_{U\{i,j,k\}} - z_{U\{i,j,k-1\}})(z_{U\{i,j,k+1\}} - z_{U\{i,j,k-1\}})}
\end{aligned} \tag{C.42}
$$

$$
\begin{aligned}
(\partial^2 v/\partial x^2)_{V\{i,j,k\}} =& \frac{2v_{V\{i+1,j,k\}}}{(x_{V\{i+1,j,k\}} - x_{V\{i,j,k\}})(x_{V\{i+1,j,k\}} - x_{V\{i-1,j,k\}})} \\
&- \frac{2v_{V\{i,j,k\}}}{(x_{V\{i+1,j,k\}} - x_{V\{i,j,k\}})(x_{V\{i+1,j,k\}} - x_{V\{i-1,j,k\}})} \\
&- \frac{2v_{V\{i,j,k\}}}{(x_{V\{i,j,k\}} - x_{V\{i-1,j,k\}})(x_{V\{i+1,j,k\}} - x_{V\{i-1,j,k\}})} \\
&+ \frac{2v_{V\{i-1,j,k\}}}{(x_{V\{i,j,k\}} - x_{V\{i-1,j,k\}})(x_{V\{i+1,j,k\}} - x_{V\{i-1,j,k\}})}
\end{aligned} \tag{C.43}
$$

$$
\begin{aligned}
(\partial^2 v/\partial y^2)_{V\{i,j,k\}} =& \frac{2v_{V\{i,j+1,k\}}}{(y_{V\{i,j+1,k\}} - y_{V\{i,j,k\}})(y_{V\{i,j+1,k\}} - y_{V\{i,j-1,k\}})} \\
&- \frac{2v_{V\{i,j,k\}}}{(y_{V\{i,j+1,k\}} - y_{V\{i,j,k\}})(y_{V\{i,j+1,k\}} - y_{V\{i,j-1,k\}})} \\
&- \frac{2v_{V\{i,j,k\}}}{(y_{V\{i,j,k\}} - y_{V\{i,j-1,k\}})(y_{V\{i,j+1,k\}} - y_{V\{i,j-1,k\}})} \\
&+ \frac{2v_{V\{i,j-1,k\}}}{(y_{V\{i,j,k\}} - y_{V\{i,j-1,k\}})(y_{V\{i,j+1,k\}} - y_{V\{i,j-1,k\}})}
\end{aligned} \tag{C.44}
$$

$$
\begin{aligned}
(\partial^2 v/\partial z^2)_{V\{i,j,k\}} =& \frac{2v_{V\{i,j,k+1\}}}{(z_{V\{i,j,k+1\}} - z_{V\{i,j,k\}})(z_{V\{i,j,k+1\}} - z_{V\{i,j,k-1\}})} \\
&- \frac{2v_{V\{i,j,k\}}}{(z_{V\{i,j,k+1\}} - z_{V\{i,j,k\}})(z_{V\{i,j,k+1\}} - z_{V\{i,j,k-1\}})} \\
&- \frac{2v_{V\{i,j,k\}}}{(z_{V\{i,j,k\}} - z_{V\{i,j,k-1\}})(z_{V\{i,j,k+1\}} - z_{V\{i,j,k-1\}})} \\
&+ \frac{2v_{V\{i,j,k-1\}}}{(z_{V\{i,j,k\}} - z_{V\{i,j,k-1\}})(z_{V\{i,j,k+1\}} - z_{V\{i,j,k-1\}})}
\end{aligned} \tag{C.45}
$$

$$
\begin{aligned}
(\partial^2 w/\partial x^2)_{W\{i,j,k\}} =& \frac{2w_{W\{i+1,j,k\}}}{(x_{W\{i+1,j,k\}} - x_{W\{i,j,k\}})(x_{W\{i+1,j,k\}} - x_{W\{i-1,j,k\}})} \\
&- \frac{2w_{W\{i,j,k\}}}{(x_{W\{i+1,j,k\}} - x_{W\{i,j,k\}})(x_{W\{i+1,j,k\}} - x_{W\{i-1,j,k\}})} \\
&- \frac{2w_{W\{i,j,k\}}}{(x_{W\{i,j,k\}} - x_{W\{i-1,j,k\}})(x_{W\{i+1,j,k\}} - x_{W\{i-1,j,k\}})} \\
&+ \frac{2w_{W\{i-1,j,k\}}}{(x_{W\{i,j,k\}} - x_{W\{i-1,j,k\}})(x_{W\{i+1,j,k\}} - x_{W\{i-1,j,k\}})}
\end{aligned} \tag{C.46}
$$

$$
\begin{aligned}
(\partial^2 w/\partial y^2)_{W\{i,j,k\}} =& \frac{2w_{W\{i,j+1,k\}}}{(y_{W\{i,j+1,k\}} - y_{W\{i,j,k\}})(y_{W\{i,j+1,k\}} - y_{W\{i,j-1,k\}})} \\
&- \frac{2w_{W\{i,j,k\}}}{(y_{W\{i,j+1,k\}} - y_{W\{i,j,k\}})(y_{W\{i,j+1,k\}} - y_{W\{i,j-1,k\}})} \\
&- \frac{2w_{W\{i,j,k\}}}{(y_{W\{i,j,k\}} - y_{W\{i,j-1,k\}})(y_{W\{i,j+1,k\}} - y_{W\{i,j-1,k\}})} \\
&+ \frac{2w_{W\{i,j-1,k\}}}{(y_{W\{i,j,k\}} - y_{W\{i,j-1,k\}})(y_{W\{i,j+1,k\}} - y_{W\{i,j-1,k\}})}
\end{aligned} \tag{C.47}
$$

$$
\begin{aligned}
(\partial^2 w/\partial z^2)_{W\{i,j,k\}} =& \frac{2w_{W\{i,j,k+1\}}}{(z_{W\{i,j,k+1\}} - z_{W\{i,j,k\}})(z_{W\{i,j,k+1\}} - z_{W\{i,j,k-1\}})} \\
&- \frac{2w_{W\{i,j,k\}}}{(z_{W\{i,j,k+1\}} - z_{W\{i,j,k\}})(z_{W\{i,j,k+1\}} - z_{W\{i,j,k-1\}})} \\
&- \frac{2w_{W\{i,j,k\}}}{(z_{W\{i,j,k\}} - z_{W\{i,j,k-1\}})(z_{W\{i,j,k+1\}} - z_{W\{i,j,k-1\}})} \\
&+ \frac{2w_{W\{i,j,k-1\}}}{(z_{W\{i,j,k\}} - z_{W\{i,j,k-1\}})(z_{W\{i,j,k+1\}} - z_{W\{i,j,k-1\}})}
\end{aligned} \tag{C.48}
$$

$$
(\frac{\partial^2 v}{\partial x \partial y})_{U\{i,j,k\}} = \frac{v_{V\{i+1,j,k\}} + v_{V\{i,j-1,k\}} - v_{V\{i+1,j-1,k\}} - v_{V\{i,j,k\}}}{(x_{V\{i+1,j,k\}} - x_{V\{i,j,k\}})(y_{V\{i,j,k\}} - y_{V\{i,j-1,k\}})} \tag{C.49}
$$

$$
(\frac{\partial^2 w}{\partial x \partial z})_{U\{i,j,k\}} = \frac{w_{W\{i+1,j,k\}} + w_{W\{i,j,k-1\}} - w_{W\{i+1,j,k-1\}} - w_{W\{i,j,k\}}}{(x_{W\{i+1,j,k\}} - x_{W\{i,j,k\}})(z_{W\{i,j,k\}} - z_{W\{i,j,k-1\}})} \tag{C.50}
$$

$$(\frac{\partial^2 u}{\partial x \partial y})_{V\{i,j,k\}} = \frac{u_{U\{i-1,j,k\}} + u_{U\{i,j+1,k\}} - u_{U\{i-1,j+1,k\}} - u_{U\{i,j,k\}}}{(x_{U\{i,j,k\}} - x_{U\{i-1,j,k\}})(y_{U\{i,j+1,k\}} - y_{U\{i,j,k\}})} \tag{C.51}$$

$$(\frac{\partial^2 w}{\partial y \partial z})_{V\{i,j,k\}} = \frac{w_{W\{i,j,k-1\}} + w_{W\{i,j+1,k\}} - w_{W\{i,j+1,k-1\}} - w_{W\{i,j,k\}}}{(y_{W\{i,j+1,k\}} - y_{W\{i,j,k\}})(z_{W\{i,j,k\}} - z_{W\{i,j,k-1\}})} \tag{C.52}$$

$$(\frac{\partial^2 u}{\partial x \partial z})_{W\{i,j,k\}} = \frac{u_{U\{i-1,j,k\}} + u_{U\{i,j,k+1\}} - u_{U\{i-1,j,k+1\}} - u_{U\{i,j,k\}}}{(x_{U\{i,j,k\}} - x_{U\{i-1,j,k\}})(z_{U\{i,j,k+1\}} - z_{U\{i,j,k\}})} \tag{C.53}$$

$$(\frac{\partial^2 v}{\partial y \partial z})_{W\{i,j,k\}} = \frac{v_{V\{i,j,k+1\}} + v_{V\{i,j-1,k\}} - v_{V\{i,j-1,k+1\}} - v_{V\{i,j,k\}}}{(y_{V\{i,j,k\}} - y_{V\{i,j-1,k\}})(z_{V\{i,j,k+1\}} - z_{V\{i,j,k\}})} \tag{C.54}$$